CHARACTERIZING HYPERPOLARIZED ^{129}Xe DEPOLARIZATION MECHANISMS DURING CONTINUOUS-FLOW SPIN EXCHANGE OPTICAL PUMPING AND AS A SOURCE OF IMAGE CONTRAST

Alex Burant

A dissertation submitted to the faculty at the University of North Carolina at Chapel Hill in partial fulfillment of the requirements for the degree of Doctor of Philosophy in the Department of Physics and Astronomy.

Chapel Hill
2018

Approved by:

Rosa Tamara Branca

Thomas Clegg

Reyco Henning

Laurie E. McNeil

Y. Jack Ng

ABSTRACT

Alex Burant: CHARACTERIZING HYPERPOLARIZED ^{129}Xe DEPOLARIZATION MECHANISMS DURING CONTINUOUS-FLOW SPIN EXCHANGE OPTICAL PUMPING AND AS A SOURCE OF IMAGE CONTRAST.
(Under the direction of Rosa Tamara Branca.)

Xenon-129 has become the isotope of choice for applications of hyperpolarized (HP) noble gases in magnetic resonance imaging (MRI) and spectroscopy due to its lower cost and higher availability compared to ^{3}He, relatively high tissue solubility, and wide range of chemical shifts. As the signal achieved in HP gas MRI is directly related to the nuclear spin polarization, the production of large volumes of highly polarized ^{129}Xe is paramount.

While near unity levels of xenon polarization have been achieved in optical cells using stopped-flow spin exchange optical pumping (SEOP), continuous-flow SEOP is the most widely used method for clinical applications as it enables the production of large volumes of hyperpolarized gas, which are necessary for imaging applications in humans. However, polarization levels achieved via continuous-flow SEOP are well below the theoretically predicted values. In this dissertation, ^{129}Xe relaxation mechanisms that are often ignored during continuous-flow SEOP are investigated, through both simulations and experiments, to quantify their effects.

First, computational fluid dynamics simulations are used to better characterize the SEOP process inside the optical cells. This work reveals turbulence inside the optical cell occurs at much lower flow rates than previously predicted. Turbulence leads to a wide distribution of xenon residency times in the cell, previously assumed to be constant for a given flow rate. This could be a cause for the discrepancy between the theoretical model for the final xenon polarization and the levels achieved experimentally.

Then, the effect of diffusion-mediated depolarization of ^{129}Xe gas in magnetic field inhomogeneities during continuous-flow SEOP is determined. The results indicate that xenon diffusion in regions in which the magnetic field abruptly changes strength and direction can be a major source of depolarization during continuous-flow SEOP. As such, care should be taken in the design of the SEOP setup to avoid these gradients in the flow path of the HP gas. In the absence of such large magnetic field gradients, wall collisions remain the major contributing factor to gas-phase spin relaxation.

Depolarization in magnetic field gradients can also be a source of image contrast for magnetic resonance imaging. To this end, the effects of longitudinal and transverse spin relaxation are separated and characterized for hyperpolarized ^{129}Xe diffusing near SPIONs using finite element analysis and Monte Carlo simulations. Simulations demonstrate that signal loss near SPIONs is dominated by transverse relaxation, with little contribution from longitudinal relaxation. In addition, experimental and computational work clearly show that the high diffusion coefficient of xenon does not provide appreciable sensitivity enhancement to SPIONs at the length scales typically probed by MRI.

This work provides a better understanding of often-ignored relaxation mechanisms during continuous-flow hyperpolarization and will aid in the effort to bridge the gap between theoretical and experimental xenon polarization levels.

ACKNOWLEDGMENTS

Getting here, six years later, was possible thanks to an unknowable number of people.

First and foremost, I am thankful for the guidance and support of my advisor, Tamara Branca. I appreciate you taking a chance on me after my first year and allowing me to find my feet as a scientist. You are the definition of hard work (I still don't know how you do it) and a model mentor, researcher, and educator.

I am thankful to the entire Branca group including Le Zhang, Drew McCallister, and Michael Antonacci. You have provided support, assistance, and helpful conversations to not only complete but understand all the work presented here. I would not want to run scans at 6 AM or on the weekend with anyone else.

I am thankful to my other committee members, Tom Clegg, Reyco Henning, Laurie McNeil, and Jack Ng, for their patience, flexibility, willingness to serve, and fortitude to read this dissertation.

Thank you to Duane Deardorff, Alice Churukian, Jennifer Weinberg-Wolf, and Stefan Jeglinski for the opportunity to learn from and teach with you. I appreciate all that you have done to make me a better instructor and prepare me to be a physics educator.

This journey would not have been possible without the support and encouragement of my family and friends. My friends have been there the entire way to celebrate and commiserate all that goes into being a graduate student. My family has been a constant source of support, not just during my time at UNC, but throughout my life. I would especially like to thank my parents. I cannot say or do enough to thank you for all that you have done for me.

Finally, thank you, Hannah. I am not sure how we made it but we did. And I cannot wait to see where we go from here.

TABLE OF CONTENTS

LIST OF FIGURES

LIST OF TABLES

LIST OF ABBREVIATIONS AND SYMBOLS

BC	Binary Collisions
HP	Hyperpolarized
HPXe	Hyperpolarized Xenon
MRI	Magnetic Resonance Imaging
NMR	Nuclear Magnetic Resonance
SEOP	Spin Exchange Optical Pumping
SNR	Signal-to-Noise Ratio
SPIONs	SuperParamagnetic Iron Oxide Nanoparticles
vdW	van der Waals molecules
^{1}H	Hydrogen
^{3}He	Helium-3
^{129}Xe	Xenon-129

CHAPTER 1: INTRODUCTION

The first demonstration of hyperpolarized (HP) gas magnetic resonance imaging (MRI) in a biological system occurred in 1994 when Albert et al. (1994) produced mouse lung images using hyperpolarized ^{129}Xe. Shortly thereafter, the first *in vivo* images using hyperpolarized ^{3}He were produced and work in hyperpolarized noble gas MRI took off. Hyperpolarized noble gas MRI offered a new frontier of imaging in the lungs that had previously been limited because of the low spin density of ^{1}H in the void space of the lungs along with a variety of other confounding factors that make proton MRI in the lungs difficult (Wild et al., 2012).

There were many hurdles to overcome in the pursuit of using hyperpolarized noble gases to perform ventilation studies in the lungs. First, ^{1}H, the most often used nucleus in magnetic resonance, has the highest gyromagnetic ratio of all stable nuclei, which means using any other nucleus will immediately impart a penalty on the achievable signal. Second, noble gas density is three orders of magnitude lower than the density of ^{1}H in the lungs even in the best case scenario of inhaling an entire inspiratory capacity ($\sim$3.5 L) of noble gas. Even if inhaling that much noble gas were feasible, it is not allowed under current imaging protocols.

To see how it is possible to overcome these obstacles, it is important to understand how signal is generated in MRI. The nuclear magnetic resonance (NMR) signal is proportional to:

$$\text{Signal} \propto N \times \mu \times \Omega_0 \times P, \tag{1.0.1}$$

where N is the nuclear spin density of the detected atom, μ is the nuclear magnetic moment of the atom, Ω_0 is the Larmor frequency, and P is the nuclear spin polarization of the detected atom. The Larmor frequency is related to the gyromagnetic ratio of the atom,

γ, and the applied magnetic field strength, B_0 ($\Omega_0 = \gamma B_0$). The magnetic moment is an intrinsic property of the atoms. Therefore, these are properties which cannot be changed. In the case of noble gases the spin density may also not be increased as there is a finite amount of gas that a subject can inhale. This leaves increasing the spin polarization as the only option to increase the signal generated by the noble gases. Hyperpolarization techniques are able to increase the nuclear spin polarization of noble gas nuclei by up to five orders of magnitude compared to their thermal equilibrium levels and provides the signal-to-noise ratio (SNR) necessary to produce void space images in the lungs.

Early work in hyperpolarized noble gas MRI centered around the use of hyperpolarized ^{3}He. Hyperpolarized ^{3}He MRI produced high SNR images in the lung to help better understand lung function and structure and was able to provide anatomical information on ventilation defects caused by asthma, cystic fibrosis, and Chronic Obstructive Pulmonary Disease (COPD) (de Lange et al., 2006; Woodhouse et al., 2009; Evans et al., 2007). The decision to use ^{3}He was an easy one as hyperpolarized ^{3}He had been used for many years as a target in fundamental nuclear physics experiments including neutron detection and parity violation in the weak interaction between the proton and neutron (Johnson et al., 1995; Anthony et al., 1993; Coulter et al., 1988). This meant that the methods to polarize helium were understood and the polarization technology was well developed. The achievable polarization levels of helium were already greater than 50%, much higher than the polarizations achieved by ^{129}Xe (Chen et al., 2014).

Unfortunately, a ^{3}He supply crisis began in the early 2000's arising from increasing demand for ^{3}He in applications outside of MRI (Cho, 2009). Specifically, the United States is interested in using hyperpolarized ^{3}He in neutron detectors for matters of national security. Additionally, there is simply an extremely limited supply source for ^{3}He as the only way to produce ^{3}He on Earth is as byproduct of tritium decay and the only sources of tritium are nuclear fusion warheads and commercial nuclear reactors. While the government still offers ^{3}He to select groups at a subsidized price, these two factors have caused the price of ^{3}He

for everyone else to rise above $2000 per liter. Fortunately, ^{129}Xe provides a cheap (∼$20 per liter for natural abundance) and effective alternative to ^{3}He and can now reach similar polarization levels for comparable volumes of gas (Nikolaou et al., 2013).

For comparison, Figure 1.1 shows typical ventilation images that are possible today using both ^{3}He and ^{129}Xe along with the first ^{129}Xe human lung image produced by Mugler et al. (1997). As can be seen, the ventilation images achieved using hyperpolarized ^{129}Xe rival the SNR and resolution of those using hyperpolarized ^{3}He. Along with providing high quality ventilation images of the lungs, ^{129}Xe has other characteristics which make it appealing for use in *in vivo* MRI including its relatively high tissue solubility and wide range of chemical shifts. These properties, along with the higher nuclear spin polarization achieved in recent years, have enabled application of hyperpolarized ^{129}Xe outside the lungs. HP ^{129}Xe is now used as a probe for gas exchange in the lungs (Wang et al., 2017), for brain perfusion studies (Venkatesh et al., 2001; Rao et al., 2016), for the detection of highly perfused fatty tissues like brown adipose tissue (Branca et al., 2014), as well as a non-invasive temperature probe (Zhang et al., 2017).

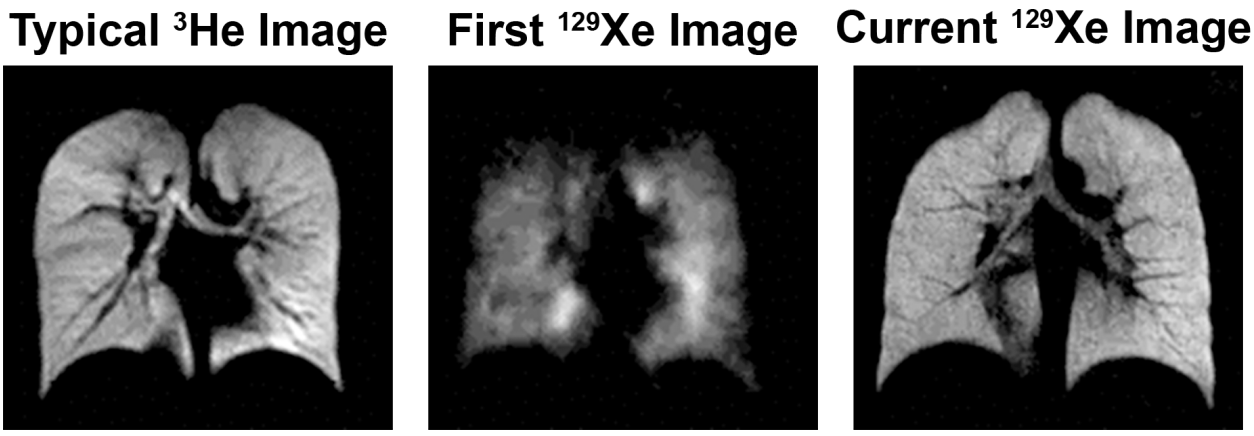

Figure 1.1: Left: Image of healthy lungs using 350 ml of HP ^{3}He at a polarization of ∼35% in a 1.5 T MRI scanner. Middle: The very first HP ^{129}Xe image of the lungs produced in 1996 using 700 ml of gas at a polarization of 1% in a 1.5 T MRI scanner. The difference in image quality caused by the much lower xenon polarization even with twice the volume of gas is easily noticeable. Right: Image of healthy lungs from 2009 using 700 ml of HP ^{129}Xe at a polarization of ∼35% in a 3 T MRI scanner. The image quality rivals that of the HP ^{3}He image. All images reproduced from Mugler & Altes (2013).

In order to perform these experiments, liter volumes of highly polarized xenon gas are necessary. Since the signal-to-noise ratio is directly related to the polarization level of the gas (Equation 1.0.1), attaining the highest possible polarization is crucial. While there are multiple methods to hyperpolarize ^{129}Xe, the most commonly used is spin exchange optical pumping (SEOP) performed in either batch-mode or continuous-flow (Barskiy et al., 2017). Though batch-mode hyperpolarization has seen polarization levels approaching unity *in situ*, the maximum achievable polarizations for xenon occur at low xenon partial pressures (Nikolaou et al., 2013, 2014; Fink et al., 2005). This suggests that continuous-flow SEOP, which operates at much lower xenon partial pressures compared to batch-mode, should provide the means for obtaining the highest final xenon polarizations. However, continuous-flow hyperpolarizers have historically performed below predicted theoretical levels (Driehuys et al., 1996; Zook et al., 2002; Hersman et al., 2008).

Identifying the cause for the discrepancy between theoretical and experimental ^{129}Xe polarization levels during continuous-flow SEOP remains one of the last obstacles faced by the field of HP gas MRI. This work focuses on possible mechanisms for polarization loss during continuous-flow SEOP which are either ignored or have been neglected to characterize their effects on the relaxation of HP ^{129}Xe. In additions, the longitudinal and transverse relaxations of xenon near superparamagnetic iron oxide nanoparticles (SPIONs) are characterized.

In the next sections, a theoretical primer on the hyperpolarization techniques of the noble gas ^{129}Xe is provided. First, the physics behind spin exchange optical pumping is described, and then the production of HP gas is detailed. Next, the theoretical framework for determining the final xenon polarization is explained using the most up-to-date models. The mechanisms which cause the depolarization of ^{129}Xe gas are reviewed, and those which are often ignored during continuous-flow SEOP are identified. Finally, an overview of the chapters contained in this dissertation is provided.

1.1 Spin Exchange Optical Pumping of Noble Gas Nuclei

The idea of optically pumping alkali metal atoms to polarize electron spins was first shown in the Nobel Prize winning experiments performed by Kastler (1967). Kastler (1967) also theorized the possibility of transferring spin polarization from the electrons of alkali atoms to nuclei of noble gas atoms. The first experimental demonstrations of this technique were reported by Bouchiat et al. (1960) in ^{3}He and by Grover (1978) in ^{129}Xe who showed it could be accomplished in ^{129}Xe at a much higher rate.

There are two possible methods for polarizing noble gas nuclei via exchange processes after optical pumping. The first, which is possible exclusively for ^{3}He, is known as metastability exchange optical pumping (MEOP) (Batz et al., 2011). This method takes advantage of a metastable state in ^{3}He, which acts as a ground state during the optical pumping process, that can be populated by electron collisions within a plasma. Coupling between the nucleus and electrons in these atoms causes the optically-pumped orientation of the electrons to affect the nuclear spin orientation simultaneously. Finally, through metastability exchange collisions these atoms transfer their angular momentum to the ^{3}He atoms which have remained in the true ground state to polarize the spins.

The second method is Spin Exchange Optical Pumping (SEOP), which is possible in a variety of nuclear spins including ^{3}He and ^{129}Xe. As the work presented here is achieved exclusively using ^{129}Xe which is hyperpolarized via SEOP, this section will center on an explanation of this process and the hardware used in our lab to polarize the gas.

However, before the process of spin exchange optical pumping is described, a clear definition of what it means for a noble gas to be "hyperpolarized" must be provided. As discussed previously, ^{129}Xe is a spin-$\frac{1}{2}$ nucleus. Therefore, in the presence of an applied magnetic field, its nuclear spin can be aligned either parallel, N_+, of antiparallel, N_-, to the magnetic field. The nuclear spin polarization may then be defined as the ratio of the difference of spins in

the ground state and excited state to the total number of spins:

$$P = \frac{N_+ - N_-}{N_+ + N_-}. \tag{1.1.1}$$

It is important to note that while this semiclassical definition is true for spin-$\frac{1}{2}$ systems, it breaks down for spins with spin quantum numbers greater than $I = \frac{1}{2}$, such as ^{131}Xe ($I = \frac{3}{2}$). As this work will not be dealing with spins that exhibit spin quantum numbers greater than $I = \frac{1}{2}$, our semiclassical definition will suffice.

Spin Exchange Optical Pumping is a two-step process whereby angular momentum is transferred from the electronic spin of an alkali metal atom to the nuclear spin of a noble gas atom. In order for this exchange to occur, first the alkali metal vapor must be polarized through depopulation optical pumping and then angular momentum transfer can occur through spin exchange binary collisions or the formation of van der Waals molecules (Happer, 1972; Becker et al., 1994; Ruset et al., 2006; Schrank et al., 2009).

In practice this is achieved through the use of an optical pumping system whose schematic is shown in Figure 1.2. Optical components are employed to ensure the proper polarization for the light illuminating the optical cell. First, the laser beam, whose polarization has been scrambled by the optical fiber, is expanded and collimated and then separated by a polarizing beam splitter into its s and p components. The s and p components are then sent through two separate quarter-wave plates, where the linear polarization is transformed into circular polarization. The optical pumping cell contains an alkali metal vapor and a gas mixture typically composed of the noble gas (^{3}He or ^{129}Xe), helium, and nitrogen. Helium is added to the gas mixture to pressure-broaden the D1 absorption line of the alkali metal to increase the amount of absorbed light (Romalis et al., 1997). Nitrogen is added to quench the fluorescence of the excited alkali metal through the vibrational modes in nitrogen thus preventing alkali metal depolarization through the absorption of emitted unpolarized photons (Wagshul & Chupp, 1994). As seen in Figure 1.2, the optical cell is housed inside a temperature controlled oven and placed at the center of a Helmholtz coil. The oven is heated

to between 100-200°C to produce an optically thick rubidium vapor while the Helmholtz coil produces a low, uniform magnetic field which causes Zeeman splitting of the alkali metals energy levels.

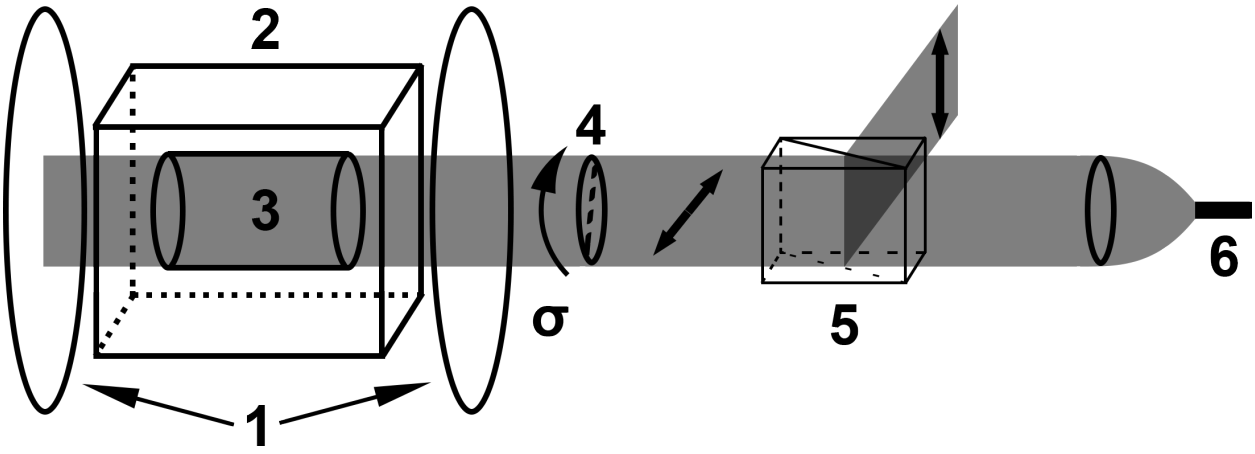

Figure 1.2: Example SEOP system schematic. 1. Helmholtz coil pair generating the polarizing magnetic field. 2. Temperature controlled oven 3. Optical pumping cell containing an alkali metal vapor and the noble gas. 4. Quarter-wave plate to circularly polarize light. 5. Polarizing beamsplitter to separate horizontally and vertically polarized light. 6. Laser tuned to D1 transition of alkali metal.

The alkali metal vapor is continuously irradiated by the laser which is tuned to the D1 transition of the alkali metal. This causes the electrons in the ground state ($5S_{\frac{1}{2}}$ for rubidium) to transition into the excited state ($5P_{\frac{1}{2}}$ for rubidium), but in order for optical pumping to occur, the alkali metal must be selectively excited from only one of the ground state spin sublevels. Optical pumping takes advantage of conservation of energy and angular momentum, in the form of quantum selection rules, to achieve this goal. In the ground state, the alkali metal has a total angular momentum of $\frac{1}{2}$ which is a combination of spin and orbital angular momentum. The same is true of the excited state. Therefore, both the ground and excited states may be in either the spin up or spin down sublevel. Because of the circularly-polarized nature of the laser light, the alkali metal is selectively excited to only one of the excited sublevels as the transition must conserve energy and angular momentum. Figure 1.3 illustrates the optical pumping of rubidium for right-circularly-polarized light. Once in the excited state, the spins undergo collisional mixing and are then evenly distributed among the

excited sublevels which means they relax to either of the ground state sublevels. Fortunately, since only one of the two ground states can absorb the angular momentum from the circularly polarized photons, the spins in other ground state become transparent to light. As a result, the "transparent" ground state becomes overpopulated and the electronic spins of the alkali atoms are said to be polarized. The depopulation of a single, alkali metal ground state sublevel is why this process is known as depopulation optical pumping.

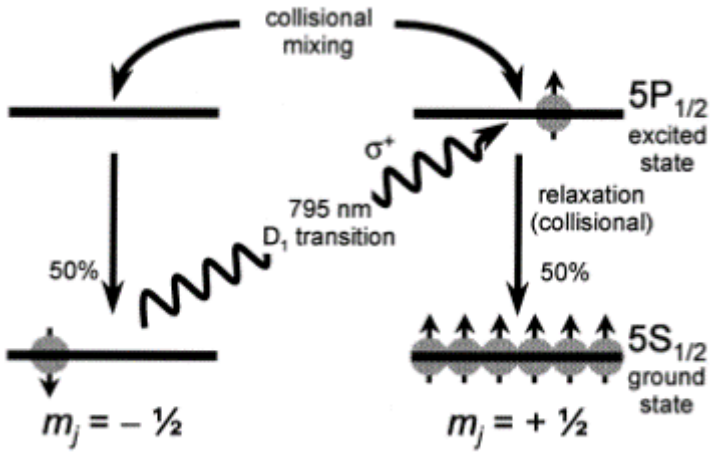

Figure 1.3: Diagram showing the depopulation optical pumping of rubidium by laser light tuned to the 795 nm D1 transition. Spins are initially in either of the 5S ground state sublevels. Due to selection rules only one of the ground state sublevels may absorb the circularly polarized photons and transition to a single 5P excited state. Collisional mixing in the excited state gives an equal probability of relaxing to each ground state sublevel but eventually all of the electrons find themselves in the non-absorbing sublevel thus polarizing the rubidium to nearly 100%. Reproduced from Möller et al. (2002).

The polarized alkali metal atoms may now transfer their angular momentum to polarize the nuclear spins of the noble gas atoms via spin exchange collisions. The polarization can be transferred through the Fermi contact interaction during binary collisions, which is the only way spins become polarized in the case of ^{3}He. However, for ^{129}Xe, there is an additional method by which the spins may become polarized. Nitrogen in the gas mixture may mediate the formation and breakup of Rb-^{129}Xe van der Waals molecules which lead to angular momentum transfer and polarize the xenon gas. These two methods of polarization transfer are illustrated in figure Figure 1.4. After collision or breakup of the van der Waals

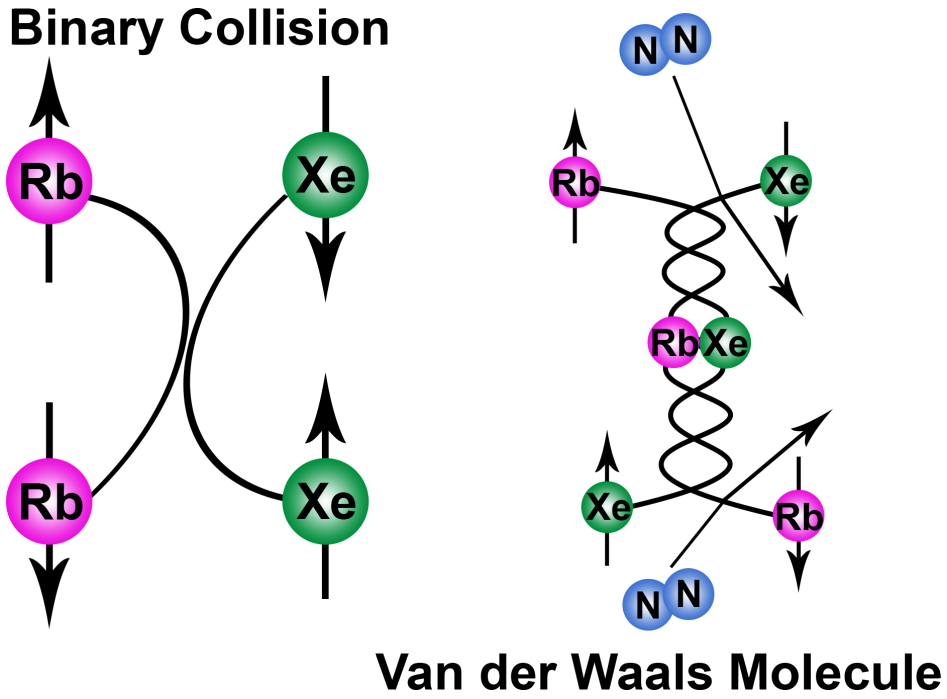

Figure 1.4: Spin exchange diagram showing the two possible means for polarization transfer between rubidium and xenon. Left: The polarized rubidium electron collides with the unpolarized xenon nuclear and through a Fermi contact interaction the polarization is transferred to the xenon nucleus. The rubidium atom may again become polarized through optical pumping. Right: Formation and breakup of Rb-^{129}Xe van der Waals molecules through three body collisions involving nitrogen. The interaction leaves the ^{129}Xe polarized and the Rb depolarized.

molecule, the rubidium atom is left depolarized and will again absorb photons from the laser irradiation until it becomes repolarized.

Originally, noble gas was polarized via SEOP using a batch method. In this case, the unpolarized noble gas is flowed into the optical cell containing the alkali metal and sealed. The alkali metal is heated to create the optically thick vapor and then illuminated by laser light to induce the optical pumping. Spin exchange follows through collisions between the alkali metal and noble gas atoms as described previously. Once the gas reaches the desired, achievable polarization, the cell is cooled to allow the alkali metal to condense and the polarized gas is transferred to a storage container. The batch method is the only method used to polarize ^{3}He using SEOP due in part to the low spin exchange rates between helium and alkali metals, which cause pump up times on the order of hours. The batch method is

also used for polarizing xenon, but the maximum achievable polarizations for xenon occur at low xenon partial pressures, meaning clinically relevant volumes ($\sim$1 L) of highly polarized (>25%) xenon can be difficult to achieve using the batch method (Ben-Amar Baranga et al., 1998; Fink et al., 2005).

Fortunately, the spin exchange rates between xenon and rubidium are three orders of magnitude higher than between helium and rubidium, decreasing the pump-up time from hours to seconds and allowing xenon to be polarized via continuous-flow SEOP (Grover, 1978; Jau et al., 2003). In this method, a gas mixture including xenon, nitrogen, and helium are continuously flowed through the optical cell illuminated by laser light. Typically, a lean mixture of xenon (between 1% and 5%) is used to limit the spin destruction mechanism due to spin-non-conserving, binary, Rb-Xe collisions (Driehuys et al., 1996). The xenon gas atoms become polarized by SEOP with an optically thick alkali metal vapor, in the same way as the batch method, but continue to flow out of the cell where they are separated from the mixture and collected using a liquid nitrogen cold trap. Once the desired volume of xenon is frozen in the cold trap, the flow of gas is stopped, the optical cell is closed, and the polarized xenon is thawed and transferred to a storage container. Continuous-flow SEOP is the most widely used method for clinical applications as it offers the potential to produce large volumes of gas in a shorter amount of time than the batch method. The work presented here is completed exclusively using hyperpolarized xenon produced via continuous-flow SEOP.

The polarizer used for all work presented in this dissertation is a Polarean 9800 ^{129}Xe Hyperpolarizer. Figure 1.5 shows an image of the polarizer as it appears in our lab along with an illustration of continuous-flow SEOP as it occurs within the optical cell of the polarizer. The polarizer uses most of the parts that were originally shipped with the polarizer with notable exceptions. First, a custom-designed, spiral cold finger is used instead of the original, cylindrical cold finger. The custom cold finger has lead to an increase in the polarization levels likely for two reasons. The spirals improve the thermal contact of the glass with its surroundings, which leads to more efficient freeze-out of xenon and faster sublimation when

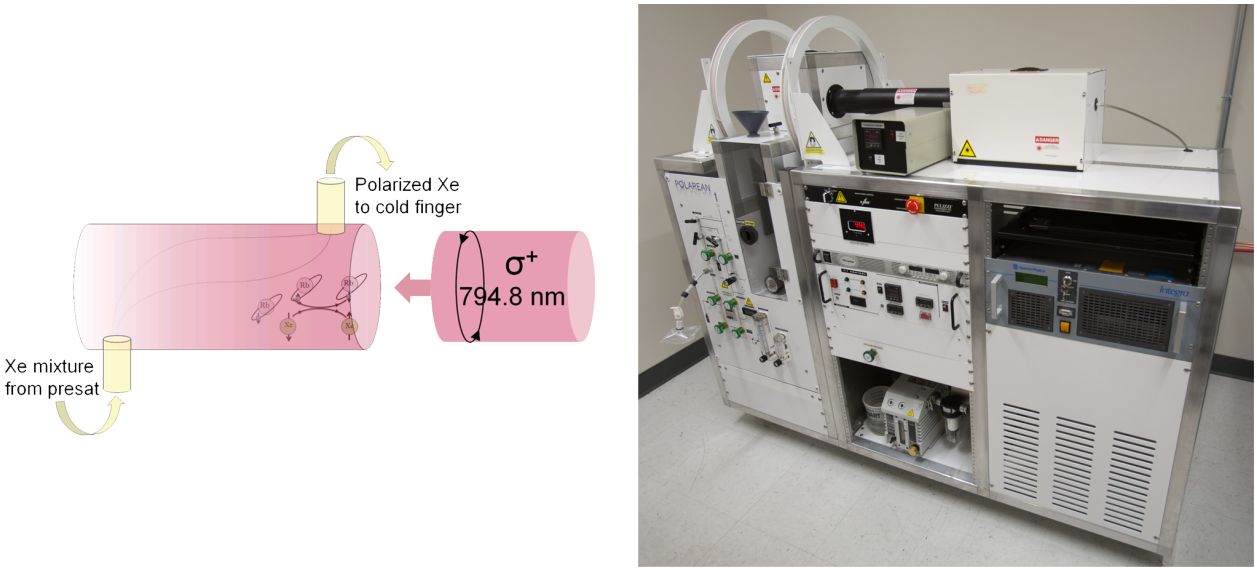

Figure 1.5: Continuous-flow hyperpolarizer used for all work presented in this dissertation. Left: Schematic of the spin exchange optical pumping process in continuous-flow mode. Right: Our lab's Polarean 9800 ^{129}Xe Hyperpolarizer which operates in a continuous-flow mode.

thawing for collection, and the larger volume of the spiral cold finger allows the xenon to freeze in a thin layer rather than a large chunk of ice. This leads to a decrease in solid state relaxation and prevents blockages in the flow during collection. The second variable part is the permanent magnet in which the cold finger is placed to increase the longitudinal relaxation of xenon while in the solid state. This magnet is interchangeable and our lab has two permanent magnet designs which may be used: the original magnet shipped with the polarizer and the magnet which is available in the Polarean 3777 ^{129}Xe Hyperpolarizer Upgrade Module. The original magnet has an open front for easy access to the liquid nitrogen dewar and a closed top which was used as a flux return. The new magnet design has a closed front and open top which generates a stronger and more homogeneous magnetic field which help produce larger final xenon polarizations.

In the next section, the equations which dictate rubidium optical pumping and polarization are discussed along with the spin exchange and spin destruction equations which ultimately determine the xenon polarization.

1.2 Theoretical Model of Noble Gas Polarization

As polarization is transferred from the electrons of the alkali metal atoms to the nuclei of the noble gas, the noble gas polarization is directly related to the alkali metal polarization. In the previous section, the process of spin exchange optical pumping was described qualitatively, but in this section, the polarization of ^{129}Xe by spin exchange with optically pumped rubidium will be described quantitatively.

The theory behind spin exchange optical pumping of noble gas nuclei has been extensively studied and is fairly well understood (Happer, 1972; Walker & Happer, 1997). Following the work of Appelt et al. (1999b), Norquay et al. (2013), and Freeman et al. (2014), a theoretical model to determine the final ^{129}Xe polarization during SEOP will be presented. The time dependence of the rubidium polarization throughout the length of the optical cell during optical pumping may be described by (Happer & Van Wijngaarden, 1987):

$$P_{Rb}(z,t) = \frac{\gamma_{OP}(z)}{\gamma_{OP}(z) + \Gamma_{SD}} \left[1 - e^{-(\gamma_{OP}(z)+\Gamma_{SD})t}\right] \tag{1.2.1}$$

where $\gamma_{OP}(z)$ is the position-dependent Rb optical pumping rate with z representing the distance from the illuminated window of the optical cell, along its main axis and Γ_{SD} is the rubidium spin destruction rate. This equation shows the exponential buildup of rubidium polarization. However, as the time needed to reach saturation of the Rb polarization is on the order of milliseconds while the time required for spin exchange is on the order of seconds or longer, the steady-state polarization of the rubidium can be used:

$$P_{Rb}(z,t) = \frac{\gamma_{OP}(z)}{\gamma_{OP}(z) + \Gamma_{SD}}. \tag{1.2.2}$$

As can be seen from this equation, achieving the maximum rubidium polarization requires minimizing the spin destruction rate of rubidium. The rubidium spin destruction rate, or the rate at which rubidium is depolarized, is a combination of depolarization through binary

Table 1.1: Spin destruction cross sections for Rb binary collisions

i	$\kappa_{SD}^{Rb-i}(\mathrm{cm^3 s^{-1}})$
Rb	4.2×10^{-13} (Ben-Amar Baranga et al., 1998)
He	$1.0\times10^{-29}\mathrm{T}^{4.26}$ (Ben-Amar Baranga et al., 1998)
N_2	$1.3\times10^{-25}\mathrm{T}^{3}$ (Chen et al., 2007)
Xe	$6.02\times10^{-15}\left(\frac{T}{298\mathrm{K}}\right)^{1.17}$ (Freeman et al., 2014)

collisions (BC) with the various constituents of the gas mixture and the formation and breakup of van der Waals molecules (vdW). The contribution from binary collisions is given by:

$$\Gamma_{SD}^{BC} = \sum_i [G_i]\, \kappa_{SD}^{Rb-i}, \tag{1.2.3}$$

where κ_{SD}^{Rb-i} is the spin destruction cross section for rubidium binary collisions with each gas in the optical cell with an atomic density $[G_i]$. Table 1.1 lists the temperature dependent values for the spin destruction cross section of rubidium with the various gases present during continuous-flow SEOP.

The contribution of van der Waals molecules to rubidium spin destruction is dependent on temperature and the atomic gas densities of He, N_2, and Xe (Ruset, 2005):

$$\Gamma_{SD}^{vdW} = \left(\frac{66183}{1 + 0.92\frac{[\mathrm{N_2}]}{[\mathrm{Xe}]} + 0.31\frac{[\mathrm{He}]}{[\mathrm{Xe}]}}\right)\left(\frac{T}{423\mathrm{K}}\right)^{-2.5} \tag{1.2.4}$$

As seen from this equation, to minimize the effects of the formation and breakup of van der Waals molecules on the rubidium spin destruction, it is advantageous to keep the xenon atomic densities low within the optical cell while maintaining high concentrations of nitrogen and helium. According to Equation 1.2.3, maintaining low xenon atomic densities also helps lower the spin destruction due to binary collisions while having high concentrations of nitrogen and helium have a negligible effect on binary collisions.

Now that we know how to minimize the spin destruction of rubidium, the next step is to maximize the optical pumping rates of rubidium within the optical cell. For this, the pump laser will be modeled as a Gaussian function with a center wavelength of λ_l and linewidth

of $\Delta\lambda_l$. The pressure-broadened D1 absorption cross section of rubidium will be modeled as a Lorentzian function. With these assumptions, the optical pumping rate, γ_{OP}, may be written (Appelt et al., 1999b; Antonacci et al., 2017):

$$\gamma_{OP}(z) = \frac{\beta}{[\mathrm{Rb}]}F, \tag{1.2.5}$$

where F is the photon flux defined by $F = \frac{I \cdot n_p}{A}$ with I being the intensity of the pumping laser, n_p being the photons per Joule produced by the pumping laser, and A being the cross-sectional area of the pump laser as incident on the optical cell. [Rb] is the rubidium number density. It is important to note that when determining the rubidium number density within the optical cell most often vapor curves, such as those from Killian (1926), Nesmeyanov (1964), or Alcock et al. (1984), are employed along with the temperature reading from a resistance temperature detector (RTD) placed on the outside of the cell. This assumes that the rubidium vapor is in thermal equilibrium with a number density determined by an RTD on the outside of the optical cell and a uniform distribution along the entire length of the optical cell. The term β is defined by:

$$\beta = \frac{2\sqrt{\pi \ln 2} r_e f_{D1} \lambda_l^3 w'(r,s)}{hc\Delta\lambda_l n_p}\,[\mathrm{Rb}]\,. \tag{1.2.6}$$

In this equation, r_e is the classical radius of the electron, f_{D1} is the rubidium D1 oscillator strength, h is Planck's constant, and c is the speed of light. The function $w'(r,s)$ is the real part of the complex overlap function dependent on r, the ratio of the atomic D1 linewidth to the pumping laser linewidth, and s, the relative detuning between the pumping laser and the D1 cross section (Appelt et al., 1999a).

Using the above equation, the attenuation of the optical pumping rate along the length of the optical cell may be described by:

$$\frac{\mathrm{d}\gamma_{OP}(z)}{\mathrm{d}z} = -\beta\left(1 - s_z\frac{\gamma_{OP}(z)}{\gamma_{OP}(z) + \Gamma_{SD}}\right)\gamma_{OP}(z), \tag{1.2.7}$$

where s_z is the fraction of laser photons that are circularly polarized. Equation 1.2.7 can be solved via separation of variables and provides a solution for the optical pumping rate such that (Appelt et al., 1999b):

$$[1 + (1 - s_z)(\beta z + K)]\,\gamma_{OP}(z) + \gamma_{SD}\ln(\gamma_{OP}(z)) + \gamma_{SD}(\beta z + K) = 0. \tag{1.2.8}$$

K is a constant determined by the boundary condition at $z = 0$. $\gamma_{OP}(0)$ is the initial optical pumping rate at $z = 0$ and forces the constant K to be:

$$K = \frac{-\gamma_{OP}(0) + \gamma_{SD}\ln(\gamma_{OP}(0))}{\gamma_{SD} + (1 - s_z)\gamma_{OP}(0)}. \tag{1.2.9}$$

This solution for the optical pumping rate as a function of the z may be used to determine the optical pumping rate at discrete positions along the axis of the optical cell. Once the optical pumping rate is known for a specific position in the cell, it may be used to calculate the expected rubidium polarization at that point through Equation 1.2.2. This provides the ability to determine a mean rubidium polarization, $\langle P_{Rb}\rangle$, throughout the cell which may be used to calculate the final xenon polarization. The xenon polarization is dependent on the residency time, t_{res}, within the optical cell and exhibits an exponential buildup in polarization, similar to rubidium, described by (Driehuys et al., 1996):

$$P_{Xe}(t_{res}) = \frac{\gamma_{SE}}{\gamma_{SE} + \Gamma}\langle P_{Rb}\rangle \left[1 - e^{-t_{res}(\gamma_{SE}+\Gamma)}\right]. \tag{1.2.10}$$

Here, Γ is the relaxation rate of ^{129}Xe, which is described in more detail in section 1.3, while γ_{SE} denotes the Rb-Xe spin exchange rate. As discussed in section 1.1, the spin exchange between xenon and rubidium is mediated by a combination of binary collisions and the formation of short-lived van der Waals molecules. Combining the formulas for the spin exchange rates due to binary Rb-Xe collision and van der Waals molecules allows for a

total theoretical spin exchange rate to be calculated by (Cates et al., 1992):

$$\gamma_{SE} = \gamma_{SE}^{BC} + \gamma_{SE}^{vdW} = \left(\kappa_{SE}^{Rb-Xe} + \sum i \frac{1}{\frac{[G_i]}{\xi_i}} \right) [\mathrm{Rb}] \,. \tag{1.2.11}$$

The spin exchange cross section due to binary collisions has been reported to be 2.2×10^{-16} $\mathrm{cm^3 s^{-1}}$ (Jau et al., 2003). The variable ξ_i is a van der Waals specific rate that has been measured for each gas atom in the mixture. The values have been calculated as ξ_{Xe} =5230 Hz, ξ_{N_2} =5700 Hz, and ξ_{He} =17000 Hz (Cates et al., 1992; Zeng et al., 1985; Driehuys et al., 1996).

The theory presented here is often used to make comparisons to experimental data for various polarizer designs and may be used for both batch method and continuous-flow SEOP. However, in all cases, the theory overestimates the polarization achieved experimentally by up to a factor of two. In the next section, the relaxation mechanisms of ^{129}Xe which may lead to this discrepancy are reviewed.

1.3 Depolarization Mechanisms of Hyperpolarized Gases

Once ^{129}Xe has been hyperpolarized, it is important to maintain the polarization up to the point it is put to use. This requires a thorough understanding of the longitudinal relaxation of xenon in the solid, liquid, and gas phases. Longitudinal relaxation, also known as T_1 relaxation, involves the interaction of nuclear spins with the surrounding environment and, through energy exchange, causes the relaxation of a nuclear spin system back to thermal equilibrium. Here, the mechanisms which cause longitudinal relaxation of ^{129}Xe in the gas and liquid phases are presented. The longitudinal relaxation rate may be described by the combined effects of multiple depolarization mechanisms using the following equation:

$$\frac{1}{T_1} = \left(\frac{1}{T_1}\right)_{CR} + \left(\frac{1}{T_1}\right)_{MFI} + \left(\frac{1}{T_1}\right)_{O_2} . \tag{1.3.1}$$

In this equation, The relaxation has been categorized as collisional relaxation, CR, relaxation due to magnetic field inhomogeneities, MFI, and relaxation with molecular oxygen, O_2. Collisional relaxation includes the intrinsic relaxation due to binary collisions and van der Waals molecules as well as the extrinsic relaxation caused by collisions with the container walls.

In the early stages of the development of SEOP, many of the intrinsic relaxation mechanisms were studied. Hunt & Carr (1963) developed the theory on relaxation due to binary collisions through the identification of the spin-rotation Hamiltonian for the ^{129}Xe nuclear spin. Relaxation resulted as magnetic fields were generated by the moving electrons in the xenon atoms during binary collisions. The highly polarizable xenon atoms are thus affected by these magnetic fields and may become depolarized. These magnetic fields are modulated by the lifetime of the collisions and thus have a small effect during the short lifetime of a binary collision. The formula for the relaxation rate of xenon caused by intrinsic binary collisions was determined to be (Streever & Carr, 1961; Hunt & Carr, 1963):

$$\frac{1}{T_1} = \frac{[\text{Xe (amagat)}]}{56\text{h} \cdot \text{amagat}} \tag{1.3.2}$$

While this equation was determined for xenon densities, [Xe], greater that 50 amagat, it was extrapolated down to $\sim$1 amagat, a regime much more relevant to SEOP, and predicts a T_1 for xenon on the order of tens of hours. Therefore, in most SEOP polarizers these mechanism is ignored because, as will soon be shown, other relaxation mechanisms provide a much shorter longitudinal relaxation time on the order of tens of minutes.

Chann et al. (2002) showed that at the number densities typically achieved during spin exchange optical pumping the formation and break up of van der Waals molecules dominates the intrinsic relaxation of ^{129}Xe. While only a very small percentage ($<$1%) of xenon atoms at room temperature and standard pressure are bound in van der Waals molecules, the lifetime of these molecules is on the order of nanoseconds, which is nearly three orders of magnitude greater than the lifetime of binary collisions(Bernardes & Primakoff, 1959). Work by Anger

Table 1.2: Room temperature coefficients, K_B ($\times 10^{-10}$ cm^3/s), for the breakup of van der Waals molecules for xenon and nitrogen as measure by [a]Chann et al. (2002) and [b]Anger et al. (2008).

Gas	K_B
Xe	1.2^a
	3.7^b
N_2	1.3^a
	1.9^b

et al. (2008) provided an empirical formula for the relaxation rate caused by the formation of van der Waals molecules. When combined with Equation 1.3.2, the formula for the total intrinsic relaxation of ^{129}Xe takes the form:

$$\frac{1}{T_1} = \frac{[\text{Xe (amagat)}]}{56\text{h} \cdot \text{amagat}} + \frac{1}{4.59\text{h}} \left[1 + \left(3.65 \times 10^{-3}\right) B_0^2\right] \left(1 + r_{N_2} \frac{[N_2]}{[\text{Xe}]}\right)^{-1}, \tag{1.3.3}$$

where B_0 is the applied magnetic field and r_{N_2} is relative efficiency of nitrogen to breakup the van der Waals molecules. The coefficients, K_B, for the breakup of van der Waals molecules by xenon and nitrogen as measured by Chann et al. (2002) and Anger et al. (2008) are listed in Table 1.2. The relative efficiency of breakup, r_{N_2}, is given by $r_{N_2} = K_B/K_{\text{Xe}}$.

Extrinsic collisional relaxation takes the form of collisions with container walls. Wall relaxation is arguably the least understood relaxation mechanism for hyperpolarized noble gases. Wall relaxation of hyperpolarized xenon depends on a wide range of factors including the surface-to-volume ratio of the container, the coating of the container, temperature, and magnetic field strength. However, highly variable relaxation times may be obtained in seemingly identical containers. To make matters worse, use of the container can change the longitudinal relaxation time due to wall collisions. Zeng et al. (1983) studied the wall relaxation of hyperpolarized ^{129}Xe and found for uncoated Pyrex, the most common material used for optical cells in continuous-flow SEOP, at temperatures of ∼80°C that wall relaxation times ranged from 200 s to as high as 1300 s in exceptional cases. Interestingly, Repetto et al. (2016) found that a specific type of glass, GE180, increased the longitudinal

relaxation time of xenon up to 9 hours with no wall coating and very long lifetimes. This increase is helpful but in most cases a relaxation time due to wall collisions is expected to be on the order of tens of minutes to an hour. While optical cells used in batch method SEOP always make use of surface coatings, those used in continuous-flow SEOP forgo this costly procedure as the contribution from wall collisions to the longitudinal relaxation time is negligible because of the decreased residency time of the xenon atoms.

The contribution of relaxation due to magnetic field inhomogeneities is the subject of chapter 3 and as such will not be covered in detail here. However, it is worth noting that relaxation in magnetic field gradients is often ignored in continuous-flow SEOP even though it is possible to obtain relaxation times on the order of minutes in regions where the magnetic field approaches zero. However, with careful design of the continuous-flow SEOP setup, relaxation arising from diffusion in magnetic field gradients can be increased to tens of minutes or hours.

Finally, relaxation through interactions with oxygen is one of the strongest longitudinal relaxation mechanisms of hyperpolarized xenon owing to the permanent magnetic dipole moment of oxygen. During SEOP and transport, depolarization of xenon because of interactions with molecular oxygen can be minimized by flushing the leak-proof storage container several times with ultra-high purity nitrogen gas before use. Unfortunately, interactions with oxygen become unavoidable during *in vivo* experiments with ^{129}Xe. Experiments performed to measure the relaxation arising from collisional coupling of oxygen produced a formula for the relaxation rate described by (Jameson et al., 1988):

$$\frac{1}{T_1} = \left(0.478\mathrm{s}^{-1}\mathrm{amagat}^{-1}\right) n_{O_2}. \tag{1.3.4}$$

In this equation n_{O_2} is the oxygen density. This equation reveals that at atmospheric concentrations, oxygen causes a longitudinal relaxation time of approximately 10 s, which becomes an inescapable consequence when performing pre-clinical or clinical scans.

1.4 Overview of Contents

In this dissertation, work fundamental to the understanding of continuous-flow spin exchange optical pumping inefficiencies is presented.

In chapter 2, the fluid flow within optical cells used for continuous-flow SEOP is studied. Previous work has been done to simulate flow within the optical cell but multiple assumptions and symmetries are used to simplify the simulations. These assumptions ignore important aspects which can considerably affect the fluid flow. Work simulating the entire 3D geometry of two different optical cell designs is presented. This work suggests that the path the gas takes before entering the optical cell influences gas flow within the optical cell and that turbulence is introduced at much lower flow rates than expected, close to those flow rates used for production of clinically relevant doses of hyperpolarized gas. Additionally, this turbulence leads to a distribution of residency times, antithetical to the way that the residency times are treated when modeling xenon polarization. These results could explain the discrepancy found between theoretical and experimental polarization levels achieved during continuous-flow SEOP.

In chapter 3, the contribution of gas diffusion in magnetic field inhomogeneities to the depolarization of xenon during continuous-flow SEOP is discussed. Through the combined use of finite element analysis and random walk simulations, large gradients were discovered in the flow path of the gas that can lead to a significant increase in the longitudinal relaxation rates of hyperpolarized ^{129}Xe, particularly in regions where the magnetic field approaches zero. The results were validated using experimental longitudinal relaxation measurements of two different permanent magnet designs, generating significantly different magnetic field distrubutions. The work suggests that careful design of the magnets required for continuous-flow SEOP can minimize the effects of magnetic field gradients on longitudinal relaxation, leaving wall collisions as the largest remaining source of gas phase spin relaxation during SEOP of xenon.

In chapter 4, relaxation of xenon diffusing in magnetic field gradients generated by

SPIONs is analyzed and used as a new source of contrast in magnetic resonance imaging. Specifically, the effects of longitudinal and transverse spin relaxation are separated and characterized for hyperpolarized ^{129}Xe undergoing restricted diffusion near SPIONs using finite element analysis and Monte Carlo simulations. Simulations showed that signal loss near the SPIONs is almost entirely caused by transverse relaxation with only a small contribution from longitudinal relaxation. Simulated image contrast and experimental images revealed that xenon diffusion provides no noticeable increase in sensitivity to SPIONs at the length scales typically probed by MRI. This indicates that to increase image contrast near iron oxide nuclei with larger gyromagnetic ratios and/or diffusion coefficients, such as ^{3}He or fluorinated gases, should be used.

Finally, in chapter 5, this work is put into context within the field. Guidelines for the design and orientation of magnets and optical cells used for continuous-flow SEOP are provided. In addition, suggestions for extending current work and possibilities for new research opened by the work in this dissertation are presented.

CHAPTER 2: CHARACTERIZATION OF FLUID FLOW IN CONTINUOUS-FLOW SPIN EXCHANGE OPTICAL PUMPING CELLS

In this chapter, results from an investigation into the fluid flow within optical cells used for continuous-flow spin exchange optical pumping of ^{129}Xe gas are presented. Wall collisions are known to be a significant source of relaxation for hyperpolarized xenon gas. Designing cells that generate laminar flow and minimize contact with the cell walls are necessary to achieve maximum polarization. Computational fluid dynamics and heat transfer simulations are performed on two different optical cells designed for use in a commercial hyperpolarizer to determine the flow regime inside the cells. These simulations reveal turbulence in both designs at flow rates typically used to generate clinical volumes ($\sim$1 liter) of hyperpolarized ^{129}Xe. This turbulence leads to a wide distribution of residency times for xenon in the optical cell which could contribute partially to the discrepancy between the predicted and experimental polarization levels currently achieved.

2.1 The Discrepancy between Theoretical and Experimental Nuclear Spin Polarization of ^{129}Xe

Continuous-flow xenon polarizers have historically produced polarization levels well below the theoretical maximum and a significant effort has been put forth to characterize continuous-flow SEOP experimentally to determine the sources of inefficiency. Norquay et al. (2013) analyzed relaxation of xenon in the solid state during continuous-flow freeze-out to measure the effect of solid state relaxation. They determined that, for a standard collection time of 40 minutes, the percentage loss of polarization due to solid state relaxation would only be about 10%. Schrank et al. (2009) performed *in situ* electron paramagnetic

resonance experiments to measure the rubidium polarization profile during continuous-flow SEOP. They concluded that, at least for their system based on the polarizer design from Ruset et al. (2006), the rubidium polarization was between 85% and 95%. As the rubidium polarization directly affects the xenon polarization, another mechanism must be causing the discrepancy. Antonacci et al. (2017) used atomic absorption spectroscopy to measure polarization losses due to dark rubidium vapor in the outlet of the optical cell. They found that dark rubidium also has a negligible impact on the final xenon polarization under typical experimental conditions. Even correcting the theoretical model to incorporate the combination of all of these effects cannot account for the nearly factor of two difference often observed between theoretical and experimental xenon polarizations.

This has led to the hypothesis that perhaps there are factors missing from the theoretical model of xenon polarization. Freeman et al. (2014) have proposed the presence of paramagnetic rubidium nanoclusters in the cell during SEOP. The presence of rubidium nanoclusters would fundamentally change the theoretical framework of xenon polarization. By including the production of these particles and the depolarizing effects they have into the standard theoretical model of spin exchange optical pumping, they were able to show consistency between the predicted and observed xenon polarization levels. However, while Flower et al. (2017) used electron microscopy to observe rubidium particles in certain locations of some optical pumping cells, these experiments were not performed during SEOP and no experimental evidence has yet shown the presence of rubidium clusters during continuous-flow SEOP. Until such time as these clusters are shown to be present during SEOP, the culprit behind SEOP inefficiency is still unknown.

One factor which is often neglected during the modeling of continuous-flow SEOP is the fluid flow within the optical cell. To our knowledge, Fink et al. (2005); Fink & Brunner (2007) are the only group to perform computational fluid dynamics simulations of flow within the optical cell during xenon hyperpolarization for both batch-mode and continuous-flow SEOP. Their work on continuous-flow pump cells provided helpful recommendations for optimizing

spin exchange that are still used today, including the need to presaturate the gas mixture with rubidium vapor prior to entering the optical cell and to preheat the gas to the oven temperature to avoid temperature gradients leading to turbulent flow. Unfortunately, the simulations performed by Fink & Brunner (2007) used simplified optical cell geometries that neglect the complex flow that develops before the gas enters the main body of the cell. In addition, assumptions about the rubidium density distribution within the optical cell are made which are possibly incorrect for many polarizers.

In the work presented here, a systematic approach is taken to determine the factors that most affect fluid flow within the optical cell during continuous-flow SEOP. This is accomplished by performing computational fluid dynamics simulations on two, complete, full-scale optical cell designs for the only available commercial hyperpolarizer. The effect of using a plug flow versus a fully-developed flow is simulated along with the effect of a density-dependent gravitational force on the gas. The fluid dynamics equations are then coupled with the heat equation to understand the effect of convection on the fluid flow within the two optical cell designs. Finally, a model of rubidium evaporation is included to determine the effect of heat absorption caused by the latent heat of vaporization. Comparisons to previous experimental work are used to test the accuracy of these simulations.

2.2 Optical Cell Designs

The work presented here utilizes two optical cell designs developed for use on the Polarean 9800 ^{129}Xe Hyperpolarizer system. Because of the size of the oven on the polarizer, constraints are placed on the possible geometries and sizes of the optical cell designs. Both optical cell designs have a radius of 2.4 cm and length of 15 cm leading to a volume of approximately 0.27 L. Each cell contains a region for presaturation of the gas mixture with rubidium vapor right before the cell inlet. As shown in Figure 2.1, the major difference between the two cell designs is the location of the inlet. While one cell has an inlet at the rear of the optical cell, the other has an inlet at the bottom of the cell. The gas mixture

used in our system is composed of 1% xenon, 10% nitrogen, and 89% helium by volume. During operation, the gas is typically flowed at a volume rate between 0.1-1.5 SLM and a total pressure of 2 atm. The optical cell, housed within the temperature-controlled oven, is maintained at a temperature of 408 K while the temperature of the presaturation region is controlled via wraparound heating cord to 458 K.

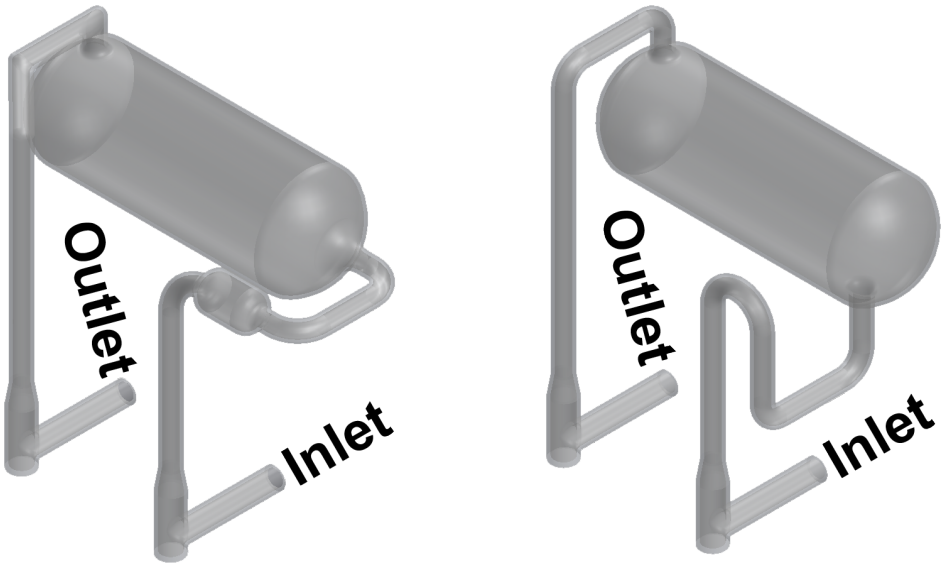

Figure 2.1: SolidWorks models of both cell designs simulated in this investigation. Left: Older cell design with a presaturation "bulb" before the inlet, which is at the rear of the optical cell. Right: Newer cell design with inlet at the bottom of the cell. The presaturation region is still present but is no longer a bulb.

2.3 Computational Fluid Dynamics Simulations of Flow within the Optical Cell

In this section, the simulations used to evaluate the factors that affect fluid flow inside the optical cell during spin exchange optical pumping are presented. The simulations start by just solving for the flow field while ignoring heat transfer and convection. Then the effects of convection on the flow are tested. Finally, a model for heat transfer due to rubidium vaporization is added to determine if any changes occur within the flow field. Particle tracing simulations are used to calculate the residency time of xenon in the optical cell.

2.3.1 Plug Flow and Fully Developed Flow at the Cell Inlet

According to the theoretical model of xenon polarization, the polarization level is dependent on the residency time of xenon within the optical cell. The longer the spins spend within the optical cell, the greater the final polarization that is achieved. Therefore, the average residency time can help to estimate the maximum achievable xenon polarization. Typically, to calculate the residency time within the cell, τ_{res}, the volume flow rate is used in the following manner:

$$\tau_{res} = \frac{V}{Q}, \tag{2.3.1}$$

where V is the volume of the optical cell and Q is the volumetric flow rate. Underlying this method of calculating the residency time are a number of assumptions. The flow profile in the cell is assumed to be radially uniform meaning all atoms have the same speed. This is a poor assumption in the case of continuous-flow SEOP as there is a great deal of piping before the optical cell which will lead to a fully developed flow profile entering the cell. Additionally, using the average residency time based on the flow rate assumes that there is no turbulence present in the optical cell. Turbulence could lead to a wide range of xenon residency times vastly changing the final xenon polarization. Computational fluid dynamics simulations by Fink & Brunner (2007) have already revealed turbulence in a simplified model of continuous-flow optical cells indicating that assuming laminar flow within complex optical cell designs is likely incorrect.

Therefore, the first test was to compare flow field results from a simulation using a plug flow inlet condition against results from a simulation which contained a fully developed flow at the inlet. A plug flow describes a flow profile with a uniform velocity. This is physically unrealistic because of the no-slip condition of the boundary. When a fluid enters a circular pipe at a uniform velocity, the particles near the surface come to a complete stop. This causes nearby particles in the boundary layer to gradually slow down as well. To make up for the velocity reduction near the boundary, the velocity of the fluid at the center of the pipe

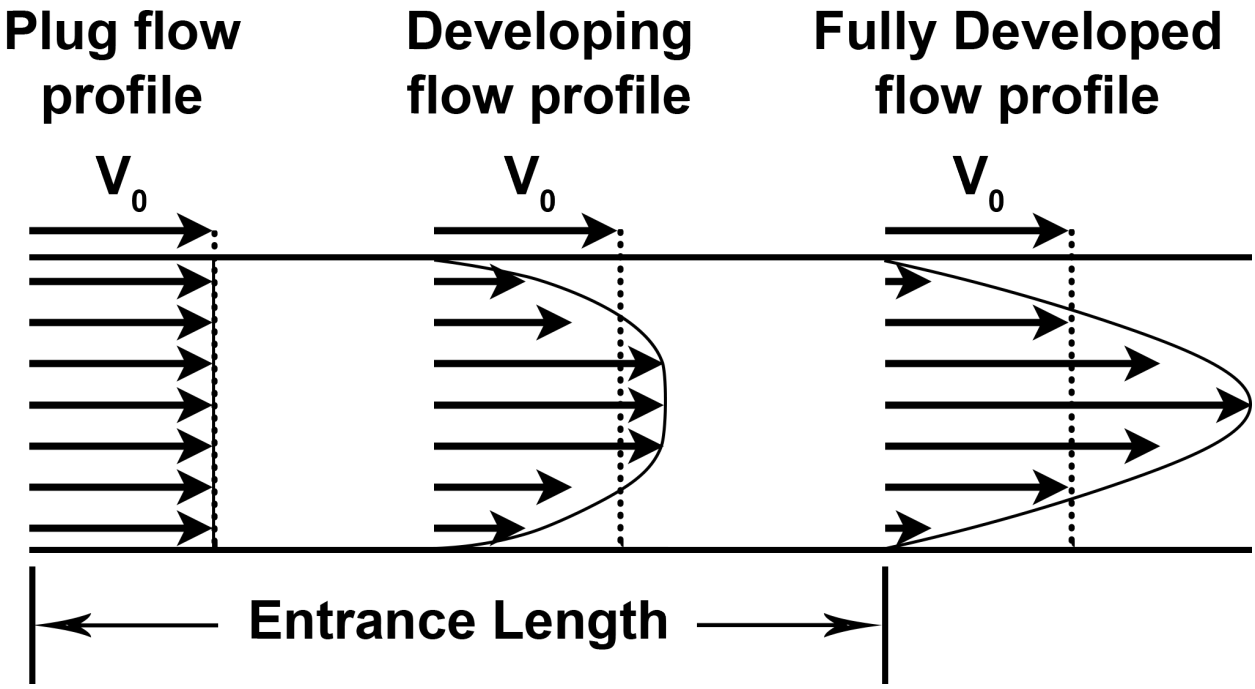

Figure 2.2: The development of the velocity profile in a pipe. The flow enters the pipe as a plug flow then after the necessary entrance length becomes fully developed. The fully developed velocity profile has a parabolic shape.

increases to maintain the mass flow rate through the pipe. Therefore, a velocity gradient develops along the pipe. A certain entrance length is required for the flow to develop this velocity gradient. After the entrance length, the flow is said to be fully developed. Figure 2.2 shows a developing flow within a pipe. As can be seen, magnitude of the velocity at the boundary is zero, while the speed at the center is twice the velocity at the inlet.

To simulate both plug flow and fully developed flow, full-scale models of both optical cell designs were developed using the CAD software SolidWorks for use in finite element analysis simulations. To compute the velocity field within the optical cell, COMSOL Multiphysics was utilized. Material properties were computed using data from the Material Properties Database Software (JAHM Software, Inc., North Reading, MA, U.S.A.). The gas mixture simulated was 1% Xe, 10% N_2, and 89% He by volume, equivalent to what is typically used, and material properties were computed using a volume-averaged value from data for the constituent gases.

For all simulations, a k-ω turbulence model was employed in solving the Reynolds-averaged Navier-Stokes equations in three dimensions using a stationary solver (Bassi et al., 2005). The k-ω turbulence model was chosen because of the low Reynolds number of the conditions simulated. Modified versions of both cells were designed without the inlet portion to simulate the plug flow at the inlet of the of the main body of the optical cell and are shown in Figure 2.3. In order to simulate a fully developed flow at the inlet of the optical cell, inlet conditions were obtained from a separate simulation to generate a fully developed flow profile. Owing to the symmetry of the pipe flow, a 2D axisymmetric simulation was used. The pipe had a diameter of 7.84 mm to match the inlet diameter of the optical cell and was taken to be 200 diameters long to ensure the flow was truly fully developed at the outlet. The inlet conditions were taken to be plug flow profiles with velocities of 0.1296 m/s, 0.2592 m/s, 0.3888 m/s, and 0.5184 m/s corresponding to volume flow rates of 0.375 SLM, 0.75 SLM, 1.125 SLM, and 1.5 SLM, respectively. These flow rates were chosen as they are values typically used to generate pre-clinical and clinical volumes of HP ^{129}Xe using continuous-flow SEOP. An example of the velocity profile at the inlet for plug flow and fully developed flow is shown in Figure 2.4

After performing the 2D axisymmetric simulations, the outlet results for the velocity, turbulent kinetic energy (k), and specific dissipation rate (ω) were mapped onto the inlet boundary condition for the 3D simulations. A normal inflow boundary condition was used at the inlet when simulating a plug flow for the four different flow rates simulated here. The temperature of the gas was kept constant at a typical oven temperature of 408 K for all simulations. A force was included on the fluid volume to determine the effect of gravity on the flow. This was accomplished through the use of a force in the negative z-direction as indicated in Figure 2.5 based on the local gas density and a parameterized gravitational constant that was taken to be zero or 9.81 m/s^2 to turn gravity off or on.

Figure 2.5 shows results from both plug flow and fully developed flow simulations for the new cell design with the inlet at the bottom of the cell. Turbulence in the cell is observed in

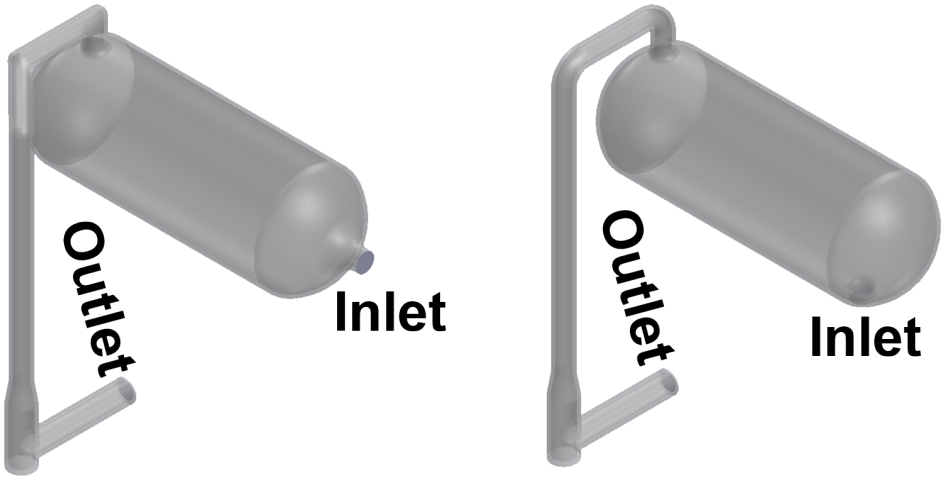

Figure 2.3: SolidWorks models of both cell designs used to simulate plug flow at the inlet of the main cell body. Left: Older cell design with inlet leg removed where the boundary condition at the rear of the cell was taken to be an inlet with a normal inflow velocity whose magnitude was the average velocity for a given flow rate. Right: Newer cell design with inlet leg removed. Boundary condition was again taken to be an inlet with a normal inflow velocity.

both cases, but the flow rate at which turbulence is introduced is not the same. For the fully developed flow simulations, turbulence is introduced as early as 0.75 SLM while turbulence begins around 1.125 SLM in the case of a plug flow. The figure also shows that the flow field in the case of the plug flow looks quite similar to the fully developed flow at a lower flow rate. For example, the flow field for a plug flow at 1.125 SLM looks much like the flow field for the fully developed flow at 0.75 SLM. This indicates that when assuming a plug flow during modeling of xenon polarization, the residency time may be estimated incorrectly because of turbulence increasing the residency time for some atoms while decreasing the residency times for others.

The older optical cell design with the inlet at the rear of the optical cell exhibited much more laminar flow in the case of plug flow and fully developed flow for all flow rates tested. Some recirculation at the back of the cell occurred for the fully developed flow simulation at 1.5 SLM but to much less of an extent compared to the optical cell with the inlet at the bottom. For both optical cell designs, in both plug flow and fully developed flow simulations, gravity had no effect on changing the flow. This is due to the fact that heat

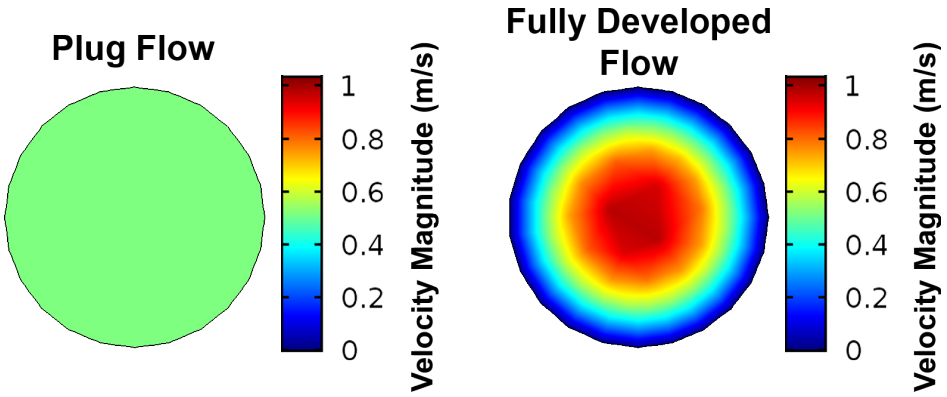

Figure 2.4: Comparison of plug flow velocity profile to fully developed flow velocity profile for flow rate of 1.5 SLM. Left: Plug flow velocity profile showing a uniform velocity of 0.5184 m/s corresponding to the 1.5 SLM flow rate. Right: Fully developed velocity profile exhibiting the expected shape and values. The velocity at the center is twice the velocity at the inlet and the gradient is parabolic with a velocity of zero at the boundary.

transfer was not included in these simulations meaning the temperature throughout the cell was uniform leading to the absence of convection within the cell. While the streamlines are helpful in gaining some knowledge about the flow in the cell they do not provide quantitative information on the time individual particles spend in the optical cell.

Particle tracing simulations were performed in all fully developed flow cases to determine the residency time of xenon in the optical cell. Xenon molecular mass and diameter were specified as particle properties for the particles in the simulation. Temperature, pressure, velocity field, and dynamic viscosity results from the turbulent flow and heat transfer simulations were used to include a drag force on the particles. Particles were released with a density proportional to the velocity magnitude at the inlet. A total of 5000 particles were released at time zero and a time-dependent solver was employed to determine each particle's position and velocity every tenth of a second up to a total time of 60 seconds. The particles underwent an elastic collision if they interacted with the wall except at the outlet. A freeze condition was taken at the outlet boundary in order to allow solution of an auxiliary variable which determined the total residency time of each particle.

Figure 2.6 shows histogram plots of the residency time for both optical cell designs. For the cell design with the inlet at the rear, the smooth nature of the histogram is to be

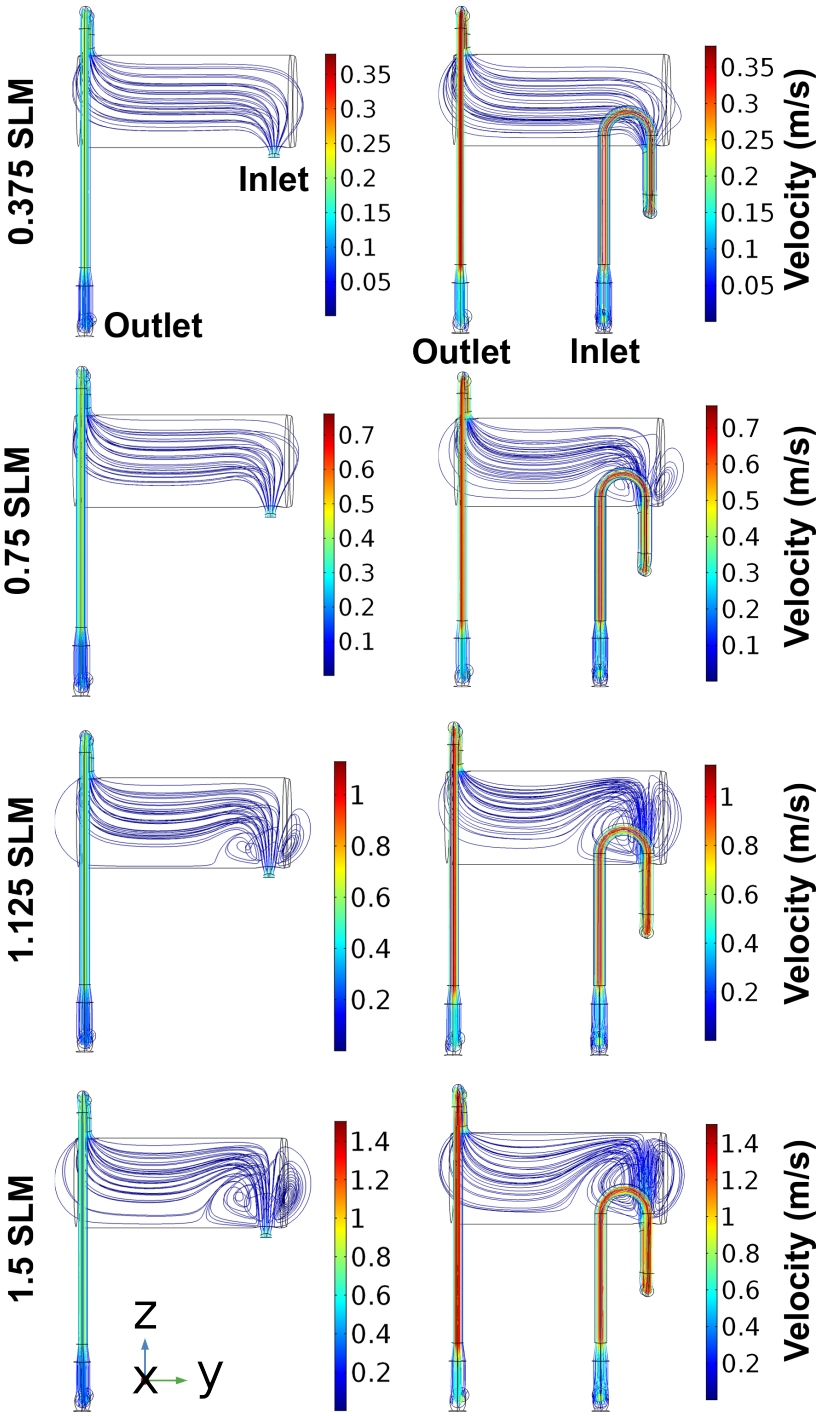

Figure 2.5: Comparison of plug flow results to fully developed flow results at multiple flow rates Left: Plug flow results for increasing flow rate. Turbulence is not introduced until around 1.125 SLM Right: Fully developed flow results for increasing flow rates. It can be seen that turbulence in the fully developed flow simulations is introduced at a lower flow rate compared to the plug flow indicating that assuming a plug flow which creates laminar flow could lead to incorrectly predicted residency times.

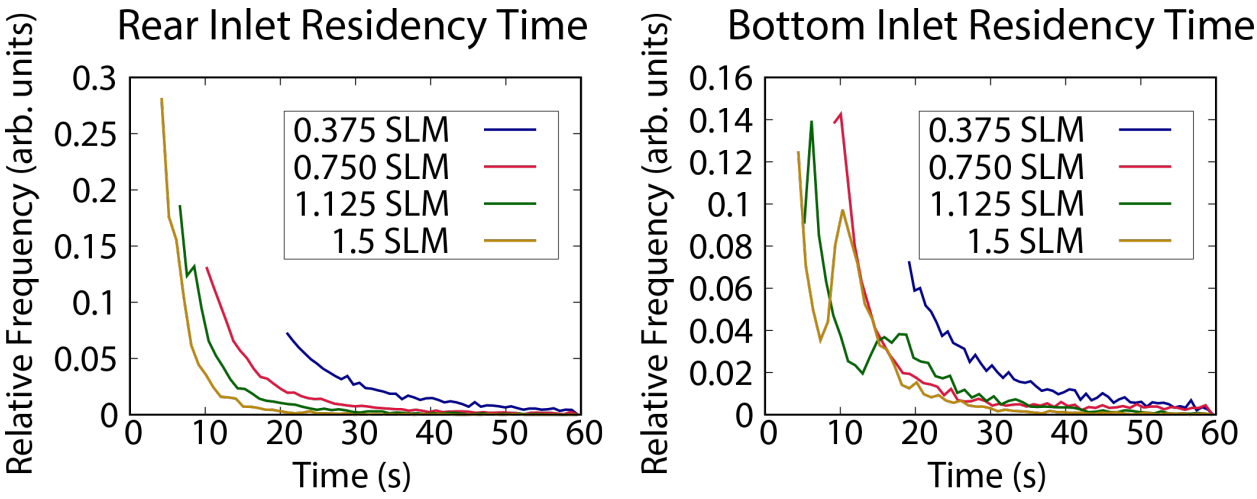

Figure 2.6: Histogram plots showing relative frequency of the residency time for each second in the optical cell for both cell designs at all simulated flow rates. Partitions are connected by lines to more easily show temporal trends. Left: Residency times for the older cell design with the outlet at the rear of the cell. The smooth, exponentially-decreasing shape of the plot shows the lack of turbulence in the cell Right: Residency times for the new cell design with the outlet at bottom of the cell. For the 1.125 SLM and 1.5 SLM plots, the spikes are indicative of significant turbulence affecting the residency times.

expected because of the laminar flow inside the cell. In the case of the cell with the inlet at the bottom, the histograms at the higher flow rates reveal the turbulence that is present in the cell. Both the 1.125 SLM and 1.5 SLM flow rates show a spike in relative frequency after the initial decreases caused by the recirculation of the gas due to turbulence in the cell. The turbulence actually has the effect of increasing the residency time of some particles in the cell as the particles are recirculated. If the effect of wall collisions is not too large on these recirculating atoms, this turbulence could increase the final polarization of xenon by increasing the average residency time. For comparison, the average residency time at 1.5 SLM for the rear inlet cell, with no turbulence, from the simulations is 7.6 s while the average residency time at the same flow rate for the bottom inlet cell, which has turbulence, is 12.1 s. The expected residency time from use of Equation 2.3.1 for the 0.27 L cell at a flow rate of 1.5 SLM is 10.8 s. This shows that in some instances the residency time may be greater than or less than the average predicted by the assumption of a plug flow which will change the predicted final xenon polarization. While these simulations shed light on flow inside the

cell for various geometries, inlet velocity profiles, and flow rates, they are not yet a complete picture of the hydrodynamic and thermodynamic processes occurring during SEOP.

2.3.2 Effects of Convection on the Flow Field within the Optical Cell

The effect of convection on the flow was determined by coupling the heat equation to the Navier-Stokes equations within COMSOL Multiphysics to simulate the heat from the oven and heat from the wraparound heating cord on the presaturation region. The CAD models were modified to include an additional material domain which served as the PYREX (Corning Inc., NY, U.S.A.) portion of the optical cell. For these simulations, all boundary condition from the CFD models remained the same. As the gas was not preheated before entering the cell, the boundary condition at the inlet was taken to be a constant temperature of 293 K to match the ambient temperature in the laboratory. The boundary condition for the presaturation region of each cell was a constant temperature of 458 K to simulate heat transfer from the heating cord, which was temperature controlled via resistance temperature detector on the glass surface, wrapped around the region. All other boundaries were given a heat flux boundary condition at a temperature of 408 K to simulate the convection on the external walls of the optical cell from the oven in which the optical cell was housed.

Figure 2.7 shows results for both optical cell designs at a flow rate of 0.375 SLM. The gravitational force on the volume of the fluid was turned off and on to determine the effect of gravity on the flow field when convection was included in the simulations. As the figure shows for the bottom inlet cell, the inclusion of the gravitational force and convection can lead to turbulence at lower flow rates compared to when convection is not present. This is in part due to the increased velocity of the gas arising from the higher temperature in the presaturation region. For the higher flow rates, where turbulence was already present without coupling heat transfer, the direction of the flow field was changed only slightly but the magnitude of the particle velocities increased similar to the 0.375 flow rate. The gravitational force had minimal effect on the rear inlet cell at all flow rates examined except for increasing the speed

of the flow field. Both gravity and convection did not lead to turbulence in the older cell design even at 1.5 SLM.

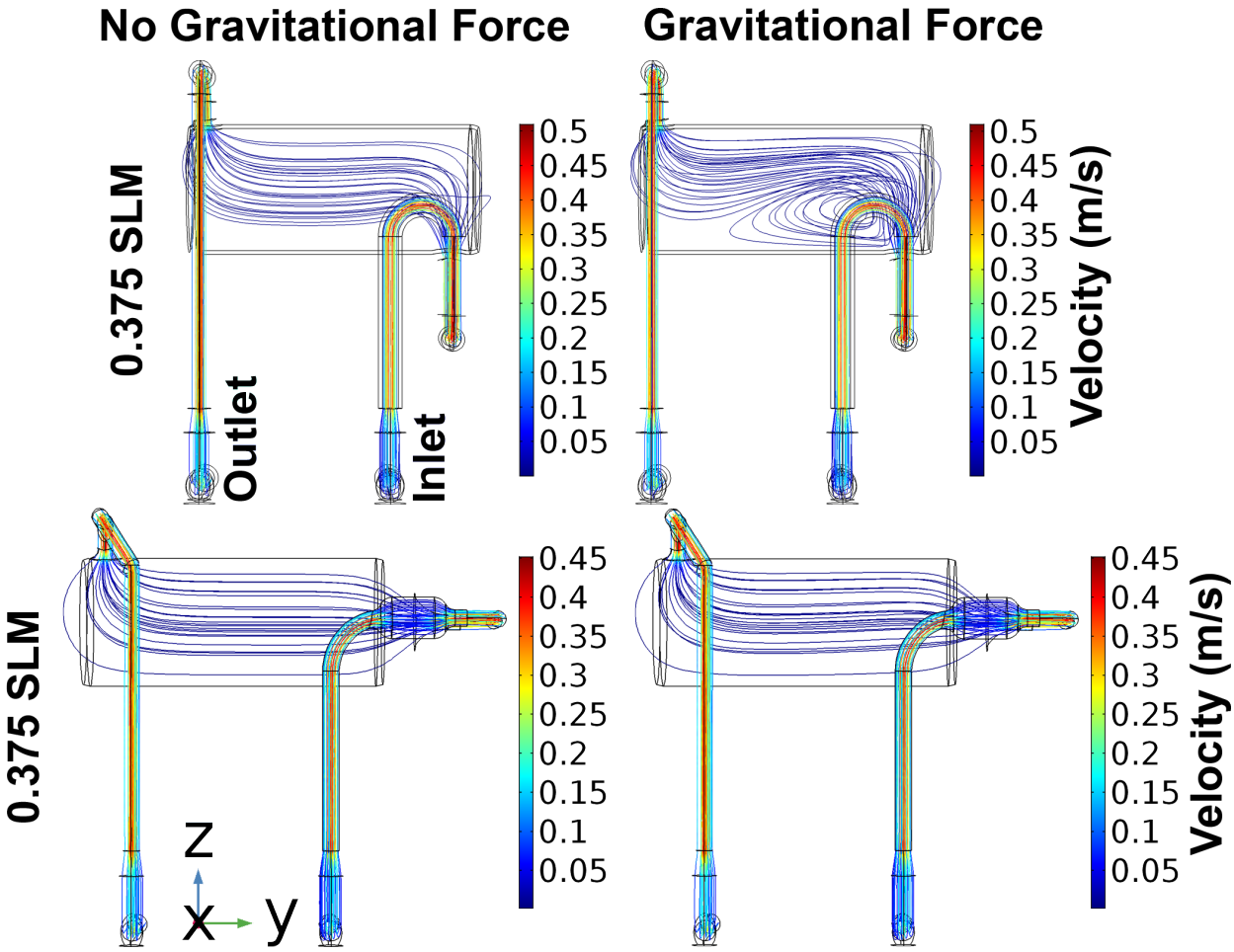

Figure 2.7: Flow field within the optical cell at 0.375 SLM when conduction and convection are included in the simulations. Top: Flow field in the bottom inlet optical cell. The gravitational force creates turbulence when convection is included at the lowest flow rate tested which was not the case in the absence of convection Bottom: Flow field in the rear inlet optical cell. Whether the gravitational force is included or not the flow remains qualitatively the same. This was true for all flow rates tested for this cell design.

These results show that including heat conduction and convection along with the gravitational force are important when determining the flow field for continuous-flow SEOP. While in some cases, these additions may have little effect on the flow in the cell, in others they can lead to significant changes. The addition of heat conduction and convection brings these simulations closer to reality but some key thermodynamic processes must still be included.

2.3.3 Modeling Rubidium Vaporization within the Presaturation Region

To incorporate heat loss from rubidium vaporization, a rubidium evaporation model was included in the simulations. The CAD models were again modified to include a pool of liquid rubidium, colored red in Figure 2.8, at the bottom of the presaturation region for each cell. The rubidium pool was 13.8 mm wide by 15.4 mm long for the optical cell with the inlet at the rear of the cell and 4.3 mm wide by 29.9 mm long for the optical cell with the inlet at the bottom of the cell. A boundary heat source for the latent heat of vaporization was used as the boundary condition for the rubidium/gas mixture boundary. The value of the heat source was calculated using the latent heat of vaporization for rubidium and a modified version of the Hertz-Knudsen equation:

$$\phi_q = \frac{-H_{vap}}{N_A} \frac{\alpha\left(p_{sat}\right)}{\sqrt{2\pi M_{Rb} k_B T}}, \tag{2.3.2}$$

where H_{vap} is the specific heat of vaporization of rubidium (844.95 kJ/kg), N_A is Avogadro's number, α is the sticking coefficient of the rubidium gas, M_{Rb} is the molecular mass of rubidium in kilograms, k_B is the Boltzmann constant, T is the local temperature, and p_{sat} is the saturation pressure of rubidium taken from the vapor pressure curve. The sticking coefficient is taken here to be 1 in order to calculate a best-case scenario rubidium evaporation and because the value is expected to be near unity (Nagayama & Tsuruta, 2003; Tsuruta et al., 1999). The partial pressure of rubidium has been removed from the Hertz-Knudsen equation to simplify computation of a steady state solution. All other boundary conditions for heat transfer were kept the same for these simulations.

The addition of the boundary heat source from rubidium vaporization only had a significant effect on the flow field in some cases. The speed of the fluid was minimally changed for all flow rates by including heat loss on the rubidium surface. However, for the rear inlet optical cell, the rubidium vaporization caused turbulence in the presaturation bulb and optical cell at the higher flow rates. Figure 2.9 shows a top view of the flow field in the

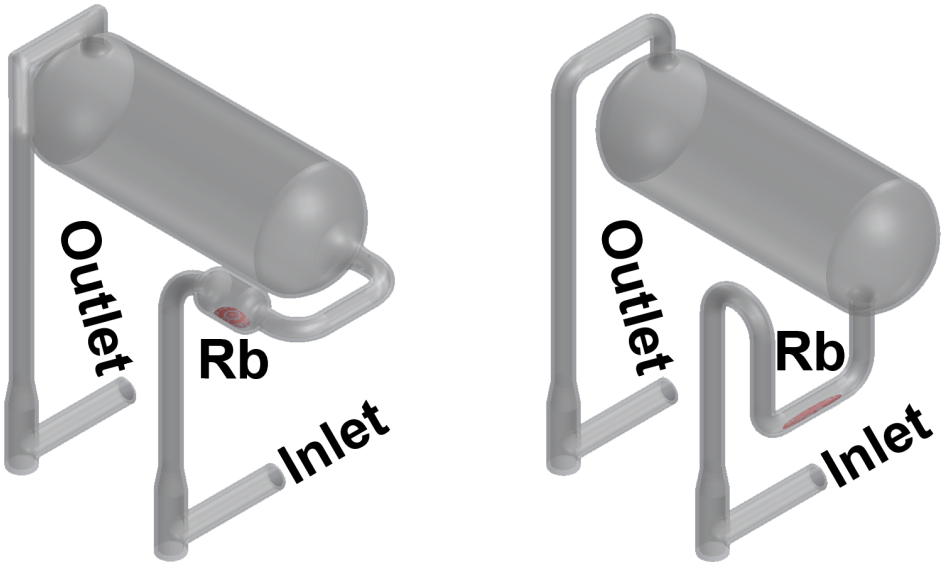

Figure 2.8: Modified SolidWorks models of both cell designs with the addition of rubidium in the presaturation region. Left: Older cell design with rubidium in the presaturation "bulb" before the inlet. Right: Newer cell design with rubidium in the presaturation region below the cell inlet.

rear inlet optical cell for the case when rubidium vaporization is included and when only conduction and convection are included. As the figure shows, in addition to turbulence, the distribution of the streamlines also changes as the gas is forced to the right side of the optical cell. This indicates that what happens to the fluid before it enters the main body of the cell is important in determining the flow field within the cell. These results also indicate the importance of including a model for heat loss at the rubidium surface to determine the flow. While Fink & Brunner (2007) performed simulations to determine the length of tubing required to completely presaturate the gas mixture with rubidium, when they performed later simulations to determine xenon polarization in a continuous-flow SEOP cell, they assumed that the gas mixture was already sufficiently presaturated with rubidium. This assumption may have changed the flow field because of the lack of heat loss from rubidium vaporization.

Particle tracing simulations were again performed to determine the change in residency time caused by the inclusion of heat transfer in the simulations. Figure 2.10 shows the histogram plots for the results of simulations which included heat conduction, convection, and rubidium vaporization. While the streamlines show turbulence within the optical cell

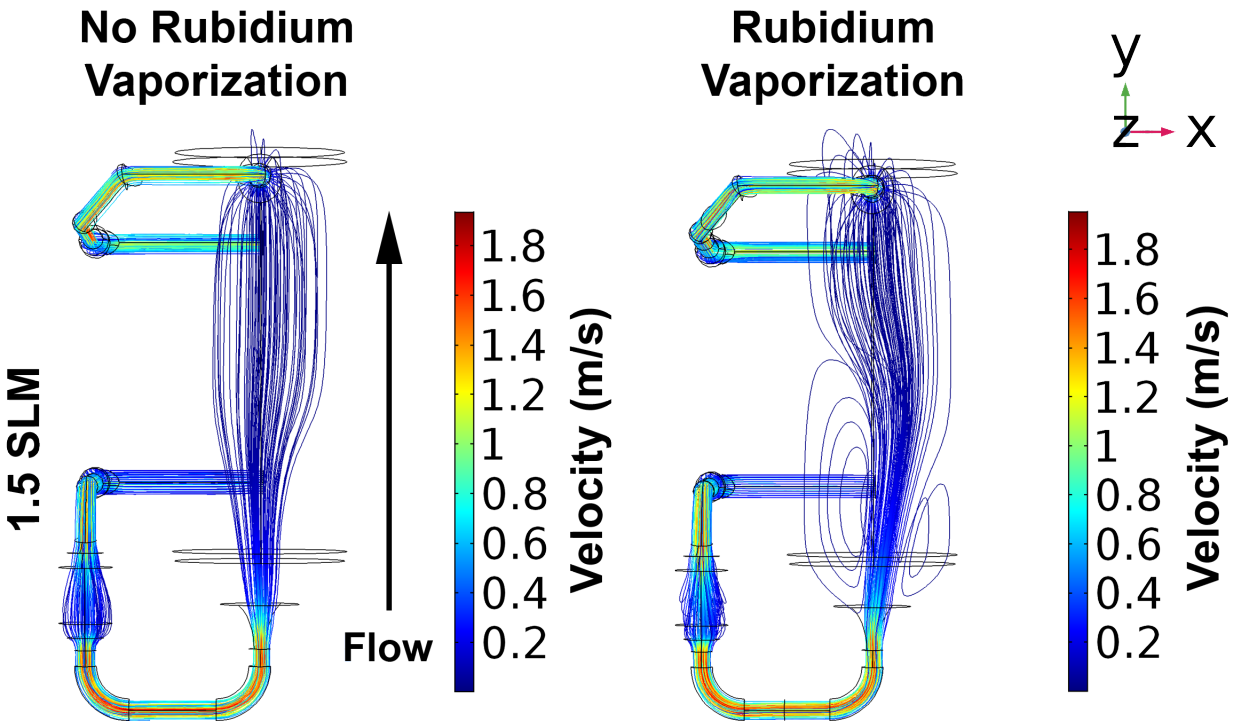

Figure 2.9: Flow field within the optical cell at 1.5 SLM for the optical cell with the inlet at the rear Left: Flow field when heat conduction and convection are included in the simulation but rubidium vaporization is neglected. No turbulence is present in the cell Right: Flow field when heat conduction, convection, and heat loss due to rubidium vaporization are included in the simulation. Notice that turbulence occurs in this case and that the gas preferentially moves to the right side of the cell.

for the rear inlet cell design, this turbulence is not noticeable on the residency time plots as shown by the smooth nature of the curve. In the case of the bottom inlet cell design, the turbulence is now noticeable at a flow rate of 0.75 SLM. The average residency time for all flow rates in both optical cell designs has decreased as compared to Figure 2.6 because of the increase in particle speed. The average residency time at a flow rate of 1.5 SLM is 4.9 s for the rear inlet cell and 8.6 s for the bottom inlet cell, both of which are shorter than the plug flow prediction of 10.8 s.

Not only are the average residency times lower than those expected from a plug flow, they are much lower than the residency time required for spin exchange to occur. Using the theoretical model for the final xenon polarization, a "spin-up" time can be calculated for the conditions in the cell during continuous-flow SEOP. This spin-up time is the time required

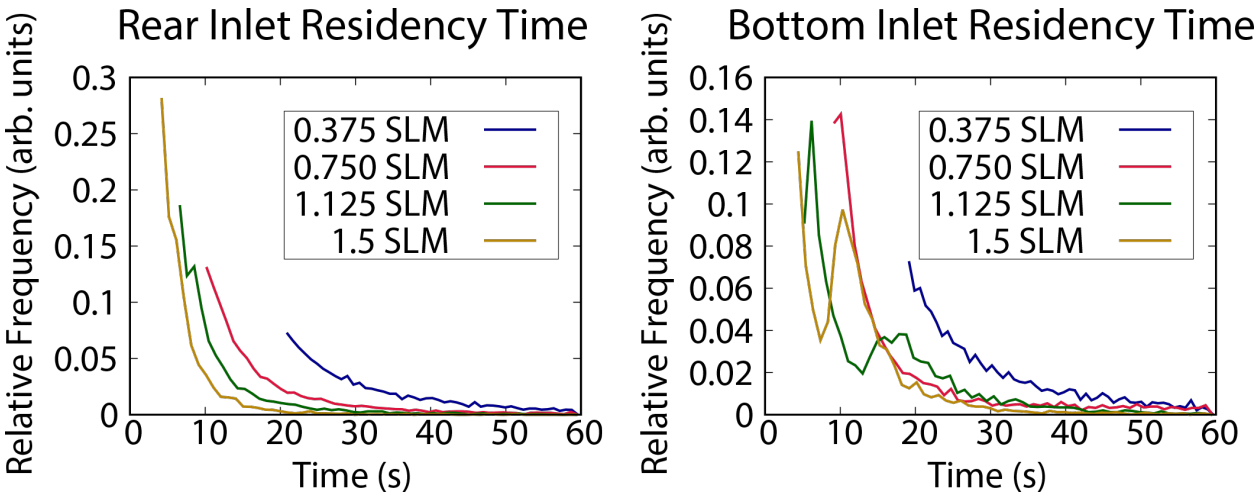

Figure 2.10: Histogram plots showing relative frequency of the residency time for each second in the optical cell for both cell designs at all simulated flow rates with heat conduction, convection, and rubidium vaporization included. Partitions are connected by lines to more easily show temporal trends. Left: Residency times for the rear inlet cell design. While streamlines show turbulence in the cell at the higher flow rates, the histogram does not reveal this turbulence. It is important to note that at 1.5 SLM nearly 100% of the particles have already left the cell in under 10 s. Much shorter than the time required for spin exchange to occur. Right: Residency times for the bottom inlet cell design. Turbulence in the cell can be seen at flow rates of 0.75 SLM, 1.125 SLM, and 1.5 SLM as indicated by the bimodal shape of the histogram.

for the expected xenon polarization to reach 63% of its maximum possible value. It can be defined using the xenon spin exchange rate, γ_{SE}, and the xenon spin destruction rate, Γ, in the following manner (Freeman, 2015):

$$\tau_{SU} = \frac{1}{\gamma_{SE} + \Gamma}. \tag{2.3.3}$$

For the conditions used in these simulations at 1.5 SLM, which were chosen to match the experimental conditions used in our lab to generate clinical volumes of HP ^{129}Xe, the spin-up time was calculated to be 34 s. This shows that even if the conditions in the cell are such that the xenon spin destruction rate is low and xenon spin exchange rate is high, the final polarization of xenon will still be lower than expected because of the short residency time of xenon in the optical cell. This could be an indicator of why polarizers with longer optical cells are able to achieve higher polarizations, simply because the residency time in the cell

increases.

These simulations still do not provide a complete picture of fluid flow during continuous-flow SEOP. Heating from laser radiation incident on the front of the cell has not been added to these simulations. While the addition of laser heating is important to accurately measure the most realistic average residency time based on flow rate, temperature, and cell geometry, the shape of the flow field is not expected to change drastically when laser heating is included. In the work performed by Antonacci et al. (2017), video was taken of the fluid flow inside the cell when the laser was turned on and the flow of the particles matches qualitatively with the results achieved in the work presented here. Of course, this is not definitive proof of the veracity of the simulations, but it does appear to point to the laser heating having less effect on the shape of the flow field and more likely increasing the speed of the particles because of increased temperature.

2.4 Conclusions

Continuous-flow hyperpolarizers often achieve experimental polarizations that are much lower (by up to a factor of two) than the predicted, theoretical polarization. A great deal of work has been done to find the cause of this inefficiency experimentally and has determined many factors that affect the final polarization slightly but has not found the reason for such a large discrepancy. One factor that has been mostly neglected up to this point is the flow inside the optical cell during SEOP. This could be a cause for the large difference between theoretical and experimental polarization as the hydrodynamic and thermodynamic processes inside the optical cell during continuous-flow SEOP are not yet fully understood. Therefore, in this work, a systematic approach is used to determine the factors that most affect the fluid flow within continuous-flow optical cells. This was accomplished using finite element analysis fluid dynamics and heat transfer simulations. The simulations started by only solving the Navier-Stokes equations for fluid flow and were adjusted to include various thermal processes to more closely match experimental parameters.

These simulations revealed that using a plug flow velocity profile at the inlet of the optical cell incorrectly determines the flow field inside the cell for a given flow rate. As such, a fully developed velocity profile must be used at the inlet to accurately determine the velocity field inside the cell. It was also shown that turbulence in the cell could lead to longer average residency times for xenon compared to laminar flow at high flow rates. This means optical cells that exhibit turbulent flow may actually lead to higher xenon polarizations through xenon spins spending a longer amount of time in the region where spin exchange can occur.

When heat transfer was added to the simulations, the results indicated that gravity can create convection rolls that lead to turbulence, even at flow rates that did not show turbulence when the temperature was uniform. Including this effect is therefore necessary to determine an accurate flow field inside the optical cell. Heat loss due to rubidium vaporization played a significant role in the flow for the higher flow rates. The heat loss led to temperature gradients in the presaturation bulb of the cell designed with the inlet at the rear of the cell. This turbulence then propagated to the main body of the cell which did not contain turbulence at any of the flow rates tested when rubidium vaporization was not included.

This work suggests that a possible cause for the discrepancy between theoretical and experimental polarization levels is the low residency time for many atoms in the optical cell. Obviously, one option to increase residency time would be to flow the gas at a lower flow rate. However, this is not possible for most clinical applications which are time-sensitive and require multiple batches of HP ^{129}Xe. Another option would be to design an optical cell with increased turbulence such that recirculation in the cell would lead to larger residency times. This would be problematic as wall collisions with the cell could lead to significant spin destruction in that case. Therefore, it appears that longer optical cells with larger volumes are necessary to increase the residency time of xenon within the main body of the cell to provide sufficient time for spin exchange to occur.

While modeling the flow field within the optical cell is important to more accurately

predict the final xenon polarization, there are many mechanisms which increase the relaxation rate of hyperpolarized xenon. In the next chapter, one of these mechanisms, which is often ignored during continuous-flow SEOP, is investigated to determine its effect on xenon polarization.

CHAPTER 3: HP ^{129}Xe DEPOLARIZATION IN MAGNETIC FIELD GRADIENTS DURING CONTINUOUS-FLOW SEOP [1]

In this chapter, results from an investigation on the effect of diffusion-mediated ^{129}Xe gas depolarization in magnetic field gradients during continuous-flow SEOP is presented. A combination of finite element analysis and Monte Carlo simulations is used to determine the effect of these gradients for the first generation of a commercial, continuous-flow xenon polarizer, while experiments are performed to validate these simulations. The results here show that large gradients in the gas-flow-path can have a significant effect on the longitudinal relaxation of hyperpolarized ^{129}Xe, especially in regions where the magnetic field assumes negligible values. To this end, care should be taken in the design of the permanent magnets required for continuous-flow SEOP. In the absence of such gradients, wall collisions are the major contributing factor to gas-phase spin relaxation of HP ^{129}Xe.

3.1 Effect of Magnetic Field Gradients on ^{129}Xe Depolarization

Early on in the lifetime of two of the most prominent hyperpolarization techniques for noble gases (metastability exchange optical pumping and spin exchange optical pumping), much work was being done to determine the effects of the various longitudinal relaxation mechanisms which depolarize the noble gas. Gamblin & Carver (1965) and Schearer & Walters (1965) were working simultaneously, albeit independently, to characterize the newly identified longitudinal relaxation mechanism of diffusion through magnetic field gradients. In order for the gas to remain polarized while moving in a magnetic field gradient, it is

[1] The work presented in this chapter was originally published in the *Journal of Magnetic Resonance*, see Burant & Branca (2016).

essential that the gas does not violate the adiabatic condition:

$$\left(\frac{1}{B_0}\right)\left(\frac{\mathrm{d}B_T}{\mathrm{d}t}\right) \ll \gamma B_0, \tag{3.1.1}$$

with γ being the gyromagnetic ratio of the diffusing spin and B_T being the transverse component of the of the local magnetic field B_0. If this condition is violated the nuclear spins will be unable to "follow" the field, resulting in their depolarization. Cates et al. (1988) extended the work done by Gamblin & Carver (1965) and Schearer & Walters (1965) by characterizing the effect of magnetic field gradients on the longitudinal relaxation of noble gases at low pressure.

Gradient-induced spin relaxation has also been studied for hyperpolarized ^{129}Xe gas near the fringe field of superconducting magnets but is often ignored during continuous-flow SEOP (Zheng et al., 2011). While most batch-mode polarization systems contain one or more sets of Helmholtz coils to generate a low (tens of gauss), uniform magnetic field necessary for SEOP, continuous-flow polarization systems contain an additional magnet used to generate a much higher magnetic field (kilogauss) in which the frozen gas is stored during the collection process. Depending on the relative configuration of these two magnets, the probability that the polarized gas, while traveling from the optical cell contained within the low field to the cold trap contained within the high field, flows through a region where the magnetic field rapidly changes direction and violates the adiabatic condition is particularly high.

Therefore, in this work, by using computer simulations and experimental measurements of longitudinal relaxation times, the effect of ^{129}Xe diffusion through the magnetic field gradients that are present in the first generation of a commercial, continuous-flow polarizer equipped with a single pair of Helmholtz coils and two different, interchangeable permanent magnets is characterized.

3.2 Theoretical Background

The contribution of magnetic field inhomogeneities to the longitudinal relaxation of hyperpolarized gases is well described by the following relation (Gamblin & Carver, 1965; Schearer & Walters, 1965):

$$\frac{1}{T_1} = D\frac{|\nabla B_x|^2 + |\nabla B_y|^2}{B_0^2}\left(1 + \Omega_0^2\tau_c^2\right)^{-1}. \tag{3.2.1}$$

In this equation, D represents the diffusion coefficient of the hyperpolarized gas and the mean magnetic field, B_0, is assumed to lie along a well-defined quantization axis (taken here to be the z-axis). B_x and B_y represent the transverse components of the magnetic field while $|\nabla B_x|$ and $|\nabla B_y|$ are their spatial gradients. In this case, the spatial gradients are assumed to be independent of position (Cates et al., 1988). The extra factor, $(1 + \Omega_0^2\tau_c^2)^{-1}$, known as the magnetic-decoupling factor, accounts for rotation of spins between kinetic collisions, where Ω_0 is the Larmor frequency and τ_c, the diffusion correlation time, is the time between collisions. As can be seen in Figure 3.1, this factor for ^{129}Xe is nearly unity for a mean magnetic field below $20T$, much higher than the magnetic fields used in this work, and will be omitted.

The assumptions in Equation 3.2.1 may be valid within the optical pumping cell, which is contained within the polarizing field generated by a Helmholtz coil, but they are not valid when the gas flows out of this region, where the magnetic field is on the order of a few tens of gauss, to the liquid nitrogen cold trap, where the magnetic field is on the order of thousands of gauss. Therefore, a modified version of Equation 3.2.1 which removes these assumptions is necessary:

$$\frac{1}{T_1} = D\frac{|\nabla B_T|^2}{B_0^2}. \tag{3.2.2}$$

While Equation 3.2.2 may not appear much different from Equation 3.2.1, B_0 now represents the local magnetic field and ∇B_T is the transverse component of the spatially-dependent gradient of B_0. In using the local magnetic field strength rather than the mean magnetic

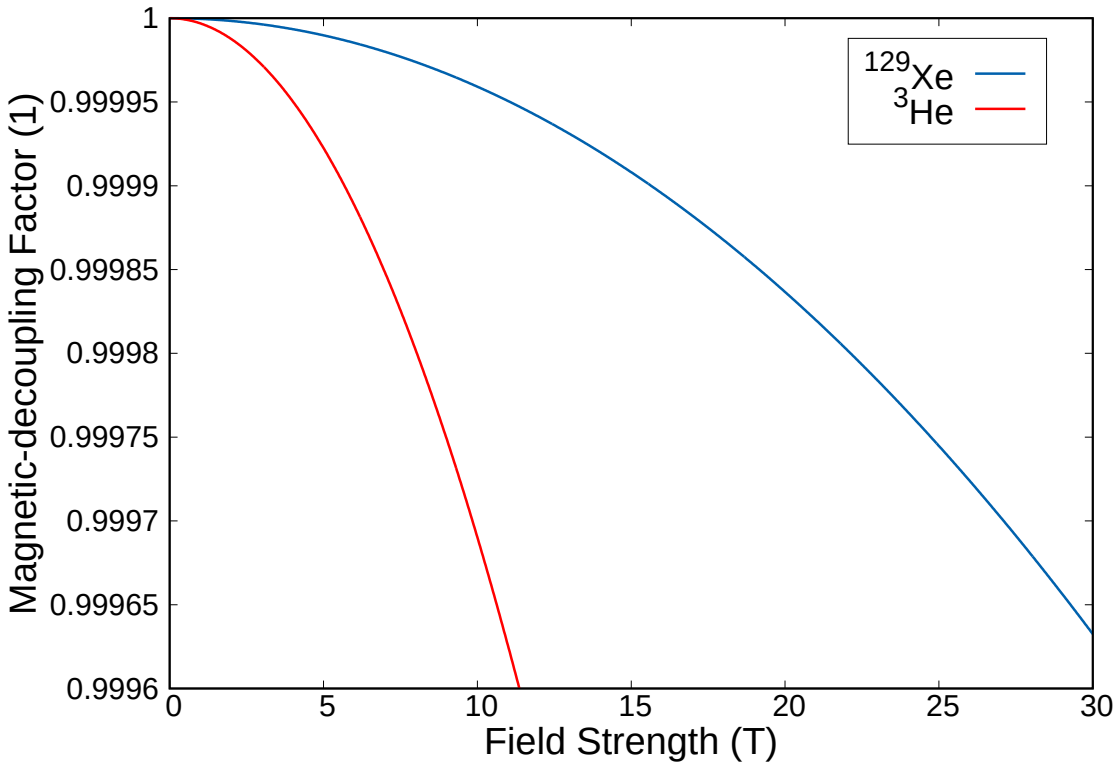

Figure 3.1: Plot of the magnetic-decoupling factor as a function of magnetic field strength for ^{129}Xe and ^{3}He. The value for ^{129}Xe is very nearly 1 for the magnetic field strengths presented in this work.

field along a well-defined quantization axis, it is important to note that a large relaxation rate in Equation 3.2.2 can be obtained whenever the magnetic field rapidly changes direction and assumes very low values, like in the case of a zero-field crossing. All results presented here will utilize Equation 3.2.2.

3.3 Simulating Depolarization of ^{129}Xe Gas in Magnetic Field Gradients

In this section, the methods used to simulate xenon diffusion and depolarization in the magnetic fields generated by a commercial, continuous-flow hyperpolarizer are discussed. First, the various magnet designs which were modeled and tested are presented. Then an overview of the finite element analysis simulations used to generate the magnetic field distribution is provided. Lastly, the Monte Carlo simulations used to simulate gas diffusion and determine the longitudinal relaxation rate are described.

3.3.1 Magnet Designs and Models

All work presented here was performed on a Polarean 9800 ^{129}Xe Hyperpolarizer system (Polarean Inc., Durham, NC, U.S.A.), a system currently used by several research groups around the world. In this system, a single pair of Helmholtz coils creates the polarization field, while the holding field is created by an interchangeable permanent magnet composed of steel and rare-earth magnets. A full-scale model of the setup was developed using the computer-aided design (CAD) software SolidWorks (Dassault Systèmes SolidWorks Corp., Vèlizy-Villacoubly, France) as shown in Figure 3.2.

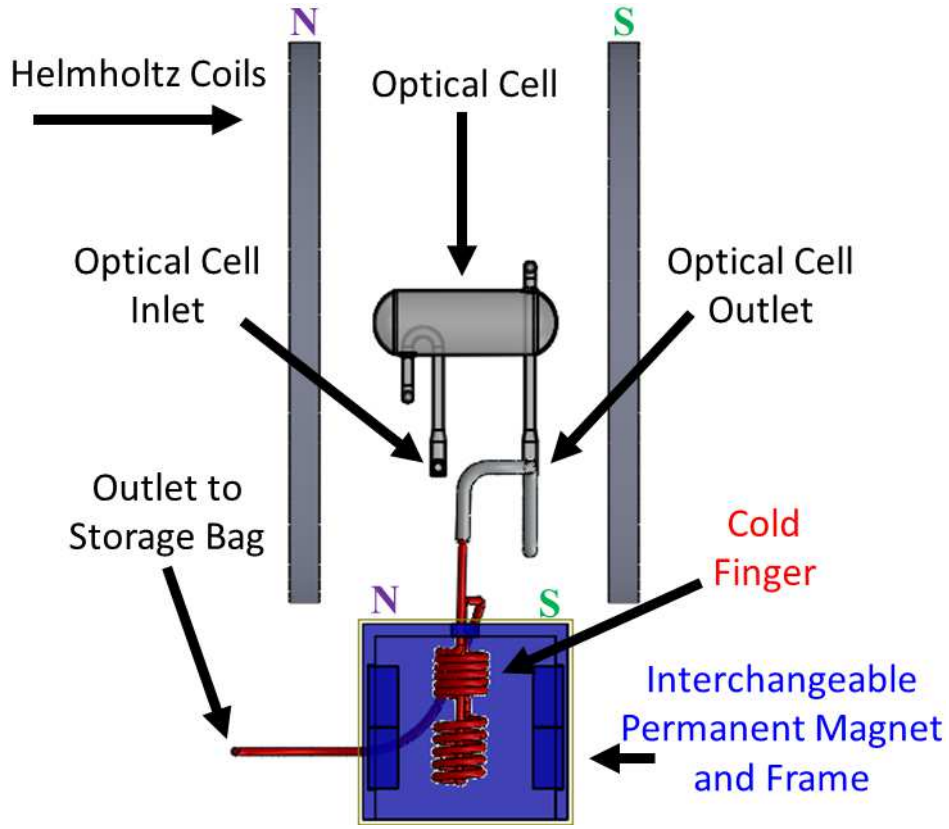

Figure 3.2: 3D model of the continuous-flow SEOP setup used in this work. The model includes the Helmholtz coil, the optical cell, the cold finger, and the interchangeable permanent magnet and frame (highlighted in blue). The interchangeable permanent magnet allowed for an easy change to the distribution of the magnetic field in the region in which the gas diffuses after thawing (colored in red). North (N) and South (S) magnetic poles have been labeled to show the direction of the magnetic field.

To test the effect of various magnetic field distributions of the longitudinal relaxation of

HP xenon gas, the interchangeable permanent magnet could be varied. Our lab currently has two different permanent magnet designs available, the original magnet design provided with the Polarean 9800 ^{129}Xe Hyperpolarizer system and one currently available with the Polarean 3777 upgrade module. The simulated longitudinal relaxation from diffusion in the magnetic fields created by both magnet designs was calculated by keeping the full-scale models identical, except for the design of the permanent magnet. Figure 3.3 shows a three-dimensional view of both permanent magnet designs. Of note for the original magnet design are the steel top containing two holes and an open front, while the new magnet design has the steel top removed and a closed, steel front.

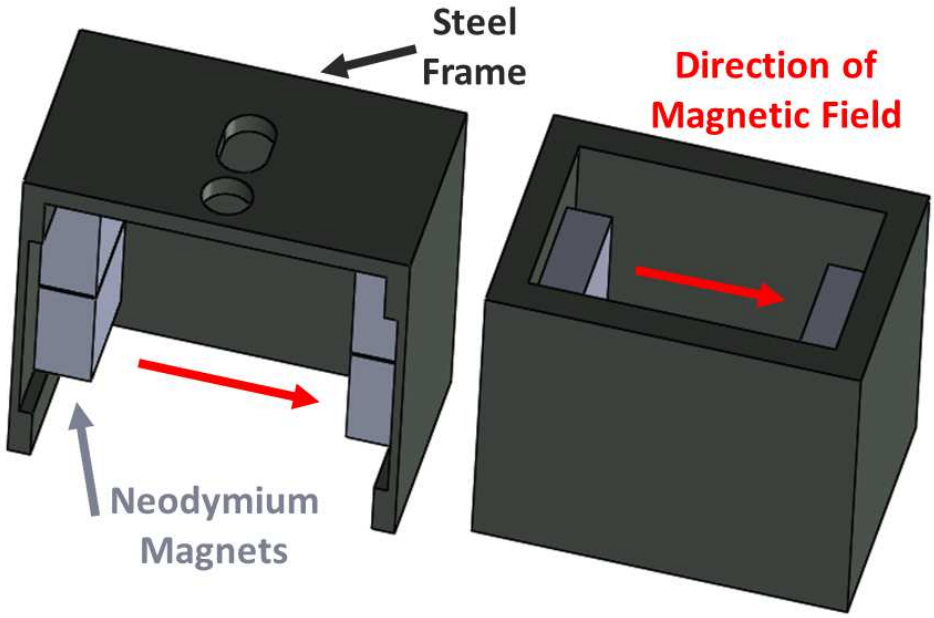

Figure 3.3: Three-dimensional view of the two different permanent magnets that were tested via simulation and experimentally. Left: Original magnet design with a closed, steel top and open front showing the 4 rare-earth magnets (2 on each side). Right: New magnet with open top and closed, steel front. For the new magnet, the magnetic field is created by 2 rare-earth magnets (1 on each side). The direction of the magnetic field is shown for both magnet designs.

3.3.2 Determination of the Magnetic Field Distribution

Simulations were first performed to determine the distribution of the magnetic field throughout the region in which xenon freely diffuses during the polarization process. The

CAD models for each permanent magnet design were imported into the finite element analysis software COMSOL Multiphysics (COMSOL, Stockholm, Sweden) where finite element analysis was used to calculate the distribution of the magnetic flux density along the gas-flow-path by solving Maxwell's equations. The parameters in the simulation were taken to match exactly the experimental setup of the Polarean 9800 ^{129}Xe Hyperpolarizer.

The Helmholtz coil consisted of two 40.3 cm ID coils spaced 23.98 cm apart that were made of 200 turns of 14 AWG copper wire. A current of 2.99 A was used in each coil to create a field within the homogeneous region of approximately 20 G. The remnant flux density for each permanent magnet was adjusted within the simulation until a center point magnetic field of 2000 G was achieved. These field strengths were chosen to match, within 5%, the field distribution experimentally measured on the polarizer system using a gauss meter.

Figure 3.4 shows the field maps for both permanent magnet designs along with magnetic field lines along the inlet of the cold finger. As can be seen from the figure, the simulations revealed significantly different field strengths and distributions for each permanent magnet design. These simulations show that the new magnet, with an enclosed, steel front face, has a much more symmetric and stronger field as compared to the original magnet design. The field lines for the original magnet design indicate a dramatic change in field direction near the top of the magnet. This change occurs when moving through the hole present in the steel plate enclosing the top of the magnet.

Upon further inspection, the COMSOL simulations showed that the original permanent magnet generates an arc-shaped region in which the magnetic field rapidly changes direction and assumes values as low as 0.0138 G. This region is shown in Figure 3.5. According to Equation 3.2.2, the rapidly changing direction and very low value of the magnetic field in this region is likely to cause a large relaxation rate for hyperpolarized xenon. This is problematic as the region is present in one of the top holes through which the gas enters and exits the cold finger. Therefore, it is possible that this region is affecting xenon polarization both as the gas enters the cold finger and is frozen and as the gas exits after thawing to be collected

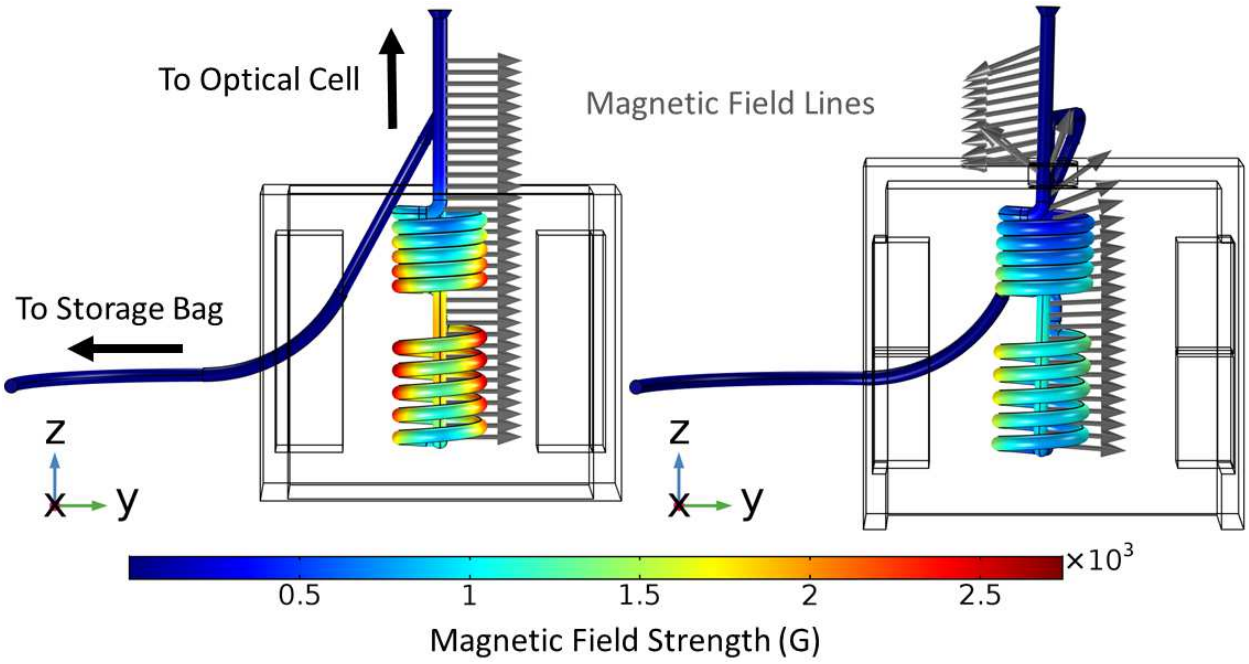

Figure 3.4: Strength of the magnetic field within the volume accessible, after thawing, to the polarized gas, before it is dispensed in a plastic bag. Left: Magnetic field strength and direction as generated by the new magnet design. Right: Magnetic field strength and direction as generated by the original magnet design. Note the drastic change in the magnetic field orientation present at the top of the original magnet design near the cold finger (spiral vessel) outlet, which is a region in which the gas is allowed to diffuse after thawing.

for use.

Figure 3.6 shows the magnetic field strength in the cold finger within the hole at the top of the original magnet. Somewhat fortunately, because of a slight twist and angle of the cold finger as positioned in the permanent magnet, the gas flowing into the cold finger during collection is minimally affected by the arc-shaped region of low magnetic field strength. However, it can be seen that the outlet of the cold finger does have a portion which sits within this arc-shaped region. This indicates that as gas is thawed and transferred to the collection bag, it must pass through the region and may potentially be depolarized.

The COMSOL simulations of the magnetic field distribution for each magnet were essential for identifying locations of potentially large longitudinal relaxation rates along the gas-flow-path during continuous-flow SEOP. They cannot however attach a numerical value to T_1 for xenon spins diffusing within the cold finger. Therefore, other means to determine

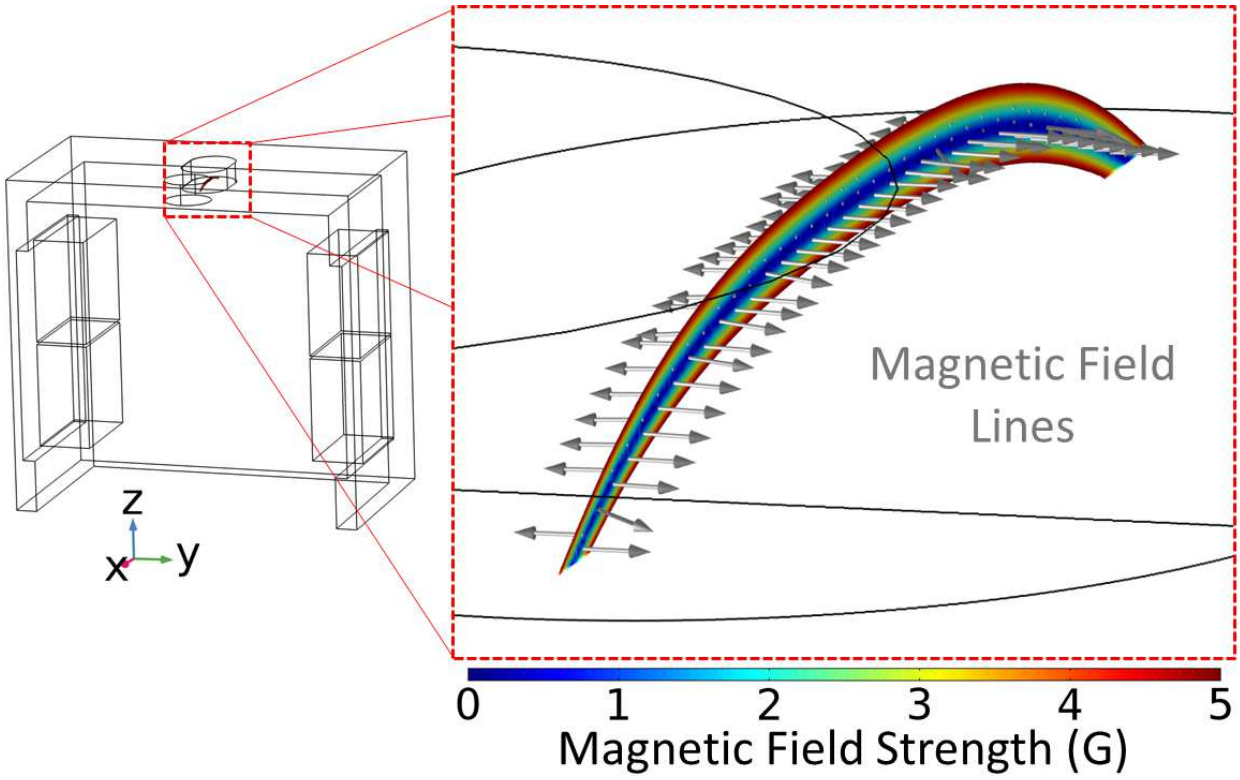

Figure 3.5: Surface plot showing the region, located within the hole at the top of the original permanent magnet, in which the magnetic field rapidly changes direction and, in some places, assumes a zero value. Left: Full view of the original magnet design with the location in which the magnetic field rapidly changes direction and assumes negligible values highlighted. Right: Close up view of the same region. The color scale represents the magnetic field strength in gauss. Arrows represent the magnetic field lines.

a theoretical T_1 value for the xenon gas must be used.

3.3.3 Theoretical T_1 of HP ^{129}Xe Gas in the Cold Finger After Thawing

The magnetic flux density components for each mesh point in the COMSOL simulations were used to calculate a theoretical T_1 value using a custom MATLAB (MathWorks, Natick, MA, U.S.A.) script. The script performed Monte Carlo simulations of gas diffusion through the computed magnetic field gradient to determine the depolarization of xenon nuclear spins as the atom freely diffused throughout the region highlighted in red in Figure 3.2 after xenon had been thawed. Within the script, the spatial components of the mesh created for the COMSOL magnetic field simulations were used as the geometry for the Monte Carlo

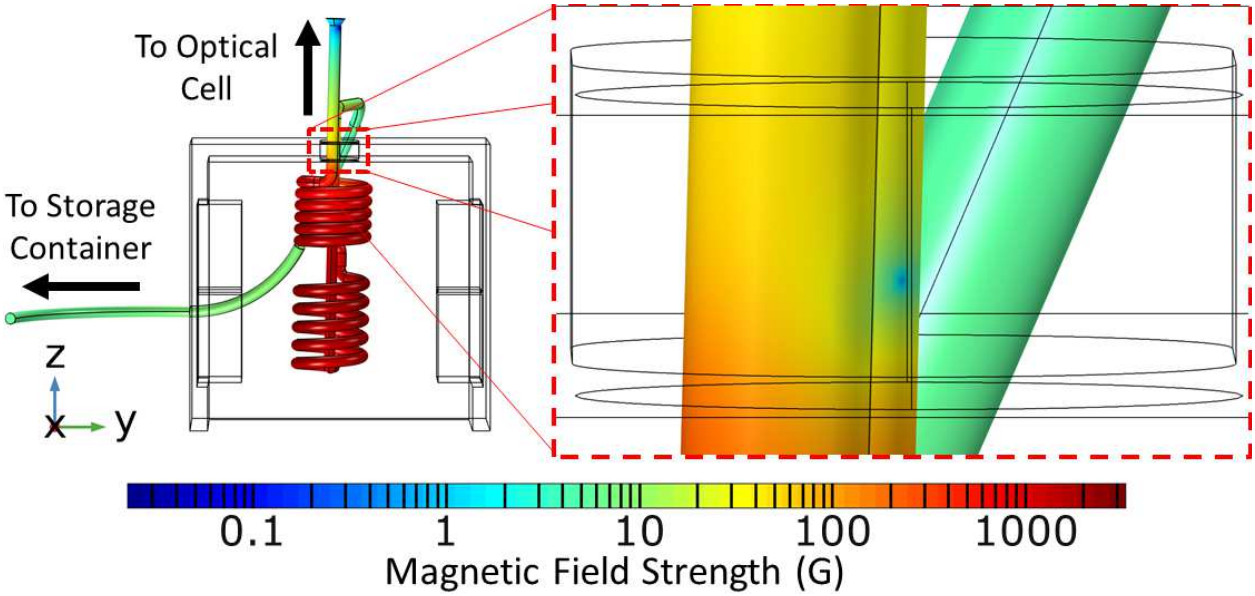

Figure 3.6: View of the magnetic field strength for the magnet design originally shipped with the polarizer. The close up view shows the area of the cold finger outlet affected by the region in which the field rapidly changes direction. A logarithmic color scale is used to highlight the areas in which the field assumes negligible values.

simulations of gas diffusion. The four nearest neighbors for each point in the geometry were used as possible locations for the spin's next step as the mesh used in the COMSOL simulations was tetrahedral. The time, t, of each diffusion step was calculated using the mean-squared displacement in dimensions as follow:

$$t = \frac{d^2}{6 \cdot D} \tag{3.3.1}$$

where d is the distance the particle traveled in moving to the nearest neighbor location and D is the diffusion coefficient of the gas.

The diffusion coefficient of xenon was calculated using the Fuller-Schettler-Giddings equation (Fuller et al., 1966):

$$D_{AB} = \frac{1.00 \times 10^{-3} T^{1.75} \left(1/M_A + 1/M_B\right)^{1/2}}{p \left[\left(\Sigma_A v_i\right)^{1/2} + \left(\Sigma_A v_i\right)^{1/2}\right]^2} \tag{3.3.2}$$

where M_A and M_B are the molar masses of each molecule, p is the total gas pressure, and

Table 3.1: Atomic Diffusion Volumes

Diffusion Volumes of Simple Molecules	
He	2.88
N_2	17.9
(Xe)[a]	37.9

[a]Parentheses indicate that the value is based on only a few data points.

$\Sigma_A v_i$ and $\Sigma_B v_i$ are the sums of the atomic diffusion volume for each component i of the molecule. The values for the atomic diffusion volumes of various molecules are tabulated in Fuller et al. (1966) and values for the molecules of interest in this paper are included in Table 3.1. A value for the the diffusion coefficient of pure xenon was determined to be 0.0132 cm^2/s for a temperature of 293.15 K and a pressure of 63 psi. For each time step in the simulation, an instantaneous relaxation rate, $\frac{1}{T_1}$, was calculated using Equation 3.2.2 and the magnetization was calculated as:

$$M(t + \Delta t) = M(t) \cdot exp\left(-\frac{\Delta t}{T_1}\right), \tag{3.3.3}$$

where $M(0)$ was taken to be one. A time-averaged T_1 value was calculated for each individual spin and then a final average T_1 value was calculated for an ensemble of 100 spins.

Based on the field distribution simulations, it was anticipated that the original magnet, containing the region of very low magnetic field strength, was going to lead to faster xenon relaxation than the new magnet. The MATLAB simulations supported this prediction. The original magnet design generated a field distribution that relaxed spins with an average T_1 of 591 $\pm$ 70 s while the new permanent magnet design produced a field distribution that relaxed spins with an average T_1 of 1644 $\pm$ 90 s.

3.4 Experimental Determination of T_1 in the Cold Finger

In order to validate the simulations, experiments were performed to measure the T_1 of xenon diffusing within the cold finger after thawing for each permanent magnet design. The

experiments were performed on the Polarean 9800 ^{129}Xe Polarizer system. The schematic of the experimental setup and gas-flow-path within the polarizer system is shown in Figure 3.2. The volume in which the gas freely diffuses after thawing is highlighted in red. The gas used in the experiments consisted of a mixture of 1% xenon at natural abundance (26.4% ^{129}Xe), 10% nitrogen, and 89% helium (Global Specialty Gases, Bethelehem, PA, U.S.A.). In this system, the gas is pre-saturated with rubidium vapor within a pre-saturation column that is maintained at 438 K and located right before the cell inlet (not shown in Figure 3.2). The rubidium-saturated gas is then flowed at a rate of 1.5 SLM and at a total pressure of 60 psi into the optical pumping cell. The optical pumping cell is housed within an oven which is temperature controlled to 358 K and is centered inside the Helmholtz coils previously described in subsection 3.3.2. The optical cell is illuminated by a 60 W diode laser with a center wavelength of 794.6 nm and FWHM of 0.2 nm (Spectra-Physics, Santa Clara, CA, U.S.A.) in order to optically pump the rubidium vapor. An on-board NMR system, located on the surface of the optical pumping cell, is used to monitor the ^{129}Xe gas polarization within the optical pumping cell in real time. From the optical cell, the gas flows to the cold finger, located at the center of the permanent magnet region, where the gas is condensed and stored for a total collection time of eleven minutes, yielding a total xenon gas volume of 165 ml. At the end of the collection time, the gas is immediately thawed and free to diffuse within the region highlighted in red in Figure 3.2.

To measure the relaxation induced by magnetic field gradients generated by the two permanent magnet designs, several batches of hyperpolarized gas were produced as previously described and allowed to diffuse within the region highlighted in red in Figure 3.2 for varying amounts of time after the freeze/thaw cycle. After the desired time of diffusion was reached, the gas was dispensed into a Tedlar bag, which was quickly (1-2 s) placed on a calibrated Polarean 2881 Polarization Measurement Station (Polarean Inc., Durham, NC, U.S.A.), to measure the gas polarization level. Gas polarization level as a function of the free diffusion time was then fit to a mono-exponential decay curve in Mathematica (Wolfram Research

Inc., Champaign, IL, U.S.A.) to derive the mean T_1 relaxation time for both permanent magnet designs.

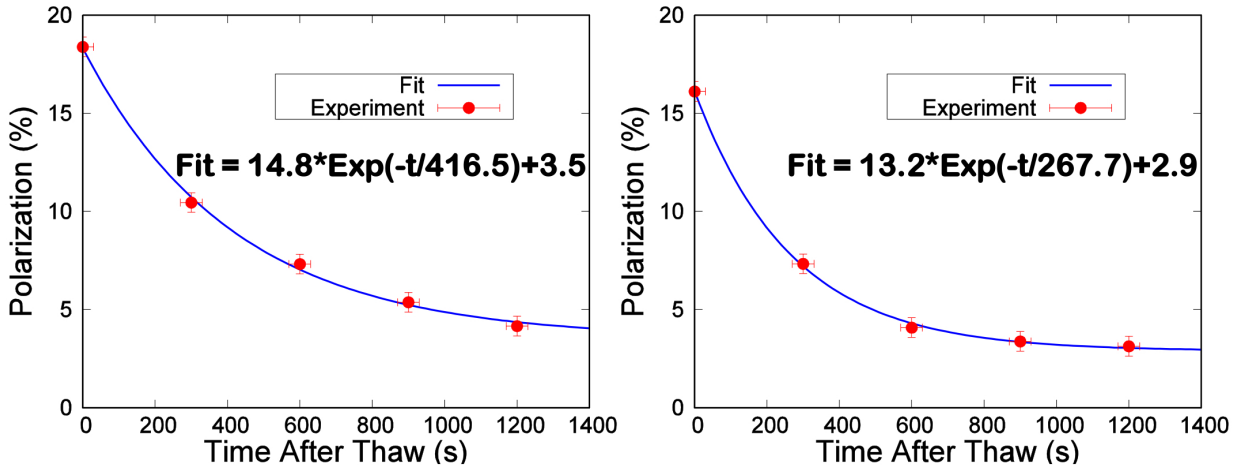

Figure 3.7: T_1 relaxation curves of hyperpolarized xenon gas caused by the magnetic field gradients generated by the two permanent magnets. For each magnet, five different batches of polarized gas were produced. The gas was then allowed to freely diffuse for varying amounts of time in the accessible volume highlighted in red in Figure 3.2. Left: Relaxation curve for the new magnet with maximum polarization of 18.4% and T_1 of 417 s. Right: Relaxation curve for the original magnet with maximum polarization of 16.1% and T_1 of 268 s.

When these T_1 experiments were performed, a T_1 value of 268 $\pm$ 14 s was measured for the original magnet and a T_1 value of 417 $\pm$ 40 s was measured for the new magnet design. The experimental data and fit can be seen in Figure 3.7. The experimental relaxation values are lower than those found using the simulations, which could be cause for concern, but is expected. In the experiments, additional collisional relaxation contributions are present from wall collisions and binary collisions between xenon atoms which will increase the longitudinal relaxation rate and lower the T_1. Both wall relaxation and relaxation due to binary Xe-Xe collisions were ignored in the simulations giving rise to the difference between the experimentally and theoretically determined T_1 values.

As the collisional relaxation is a property of the cold finger, which was never changed during the experiments, the collisional relaxation rates are expected to be the same for the two different magnet designs. Therefore, the values for the collisional relaxation rate can be

estimated by using the experimental relaxation rate and the computed relaxation rate due to magnetic field inhomogeneities in the following fashion:

$$\left(\frac{1}{T_1}\right)_{EXP} = \left(\frac{1}{T_1}\right)_{MFI} + \left(\frac{1}{T_1}\right)_{CR} \tag{3.4.1}$$

where EXP indicates the experimentally determined T_1 value, MFI indicated the relaxation contribution due to magnetic field inhomogeneities, and CR is the collisional relaxation contribution consisting of wall relaxation and transient and persistent xenon dimer.

By using this relation, the estimate for the combined contribution of wall collisions and binary collisions to the longitudinal relaxation time was on the order of 500 s for both magnet designs (488 ± 70 s for the original magnet design and 558 ± 70 s for the new magnet design). In pure xenon, Xe-Xe molecular relaxation is known to be the dominant fundamental relaxation mechanism below 14 amagat, giving a relaxation time on the order of hours (Chann et al., 2002). The experiments performed in this work were within this regime at a calculated xenon density of 4 amagat. As such, it is reasonable to assume that the major contribution to gas-phase relaxation, at least in this system, is likely to be wall collisions with perfluoroalkoxy (PFA), which makes up most of the tubing that connects the cold finger to the gas outlet, and uncoated Pyrex, which makes up the cold finger. Wall relaxation times for uncoated Pyrex have been measured at temperatures of ∼80 °C to range from 200 s to as high as 1300 s in exceptional cases (Zeng et al., 1983). Therefore, the number obtained here for the T_1 through wall relaxation is not in disagreement with the range of values previously measured.

3.5 Conclusions

The experimental and simulation results shown here indicate that the crossing of regions in which the magnetic field rapidly changes direction and assumes negligible values, such as the arc-shaped region in Figure 3.5, can be a major relaxation mechanism and care should be

taken to avoid creating such gradients within the hyperpolarized gas-flow-path. To this end, the flux return on the new magnet design included in the Polarean 3777 upgrade module represents a significant improvement over the previous design, eliminating such gradients and thus better preserving the nuclear spin polarization.

In this chapter, the influence of strong magnetic field gradients on the relaxation of hyperpolarized xenon during continuous-flow SEOP was studied using a combination of finite element analysis and Monte Carlo simulations. Simulation results were then compared to experimental T_1 values obtained from a commercially available polarizer system using two different permanent magnet designs, which were able to generate significantly different magnetic field distributions within the gas-flow-path. Specifically, one of the magnets produced a region in which the magnetic field rapidly changed direction, causing a faster relaxation of xenon atoms diffusing from the cold finger to the collection bag.

The relative configuration and the geometry of the magnets used for continuous-flow SEOP requires careful design in order to avoid the generation of regions in which the magnetic field rapidly changes direction where the gas is able to diffuse and relax. While magnetic field gradients should not be ignored during continuous-flow SEOP, this work suggests that, in the absence of such strong gradients, wall collisions are the major contributing factor to gas-phase spin relaxation.

In the context of noble gas hyperpolarization, mechanisms which cause increased relaxation are often avoided . However, when trying to generate image contrast in gradient-recalled echo magnetic resonance imaging sequences, increased relaxation leads to increased contrast. In the next chapter, results from an attempt to use the depolarization of xenon gas in magnetic field inhomogeneities to increase the image contrast of xenon near superparamagnetic iron oxide particles are presented.

CHAPTER 4: HP ^{129}Xe RELAXATION IN MAGNETIC FIELD GRADIENTS GENERATED BY SUPERPARAMAGNETIC IRON OXIDE NANOPARTICLES [1]

In this chapter, results from an investigation to assess the effects of superparamagnetic iron oxide nanoparticles on the longitudinal and transverse relaxation of hyperpolarized xenon gas are presented. The known depolarization effect of xenon gas in magnetic field gradients is leveraged in an attempt to increase MR sensitivity near the strong field gradients generated by SPIONs. To this end, 3D Monte Carlo simulations are used to simulate the signal decay and resulting image contrast of HP ^{129}Xe gas near SPIONs. Simulations reveal that signal loss near SPIONs is dominated by transverse relaxation, with little contribution from longitudinal relaxation, while simulated image contrast and experiments show that diffusion provides no appreciable sensitivity enhancement to SPIONs.

4.1 Introduction

As discussed in chapter 1, hyperpolarized noble gas MRI has been extensively developed as a methodology to image the lung airspaces in place of conventional proton MRI. Proton MRI in the lung, while possible, is difficult for a variety of reasons (Wild et al., 2012). The lung provides intrinsically low MR signal because of the low density of water in the lungs and because susceptibility differences between air and tissue create strong, local magnetic field gradients that cause rapid dephasing of the ^{1}H signal (Theilmann et al., 2009). Fortunately, hyperpolarized noble gases are much less affected by the highly inhomogeneous magnetic environment of the lungs due to their rapid diffusion (Chen et al., 1999).

[1] The work presented in this chapter was originally published in the *Journal of Magnetic Resonance*, see Burant et al. (2018).

Another contrast agent that has been of particular interest for *in vivo* applications is SuperParamagnetic Iron Oxide Nanoparticles (SPIONs). These particles demonstrate high compatibility with biological systems and their properties can be easily manipulated by adjusting their size and their surface coating, or by surface functionalization (Chen et al., 2010, 2011; Shah et al., 2016). Functionalized SPIONs have been used to target cells, like tumor cells, and to enhance the sensitivity of conventional ^{1}H MRI down to the single cell (Smirnov et al., 2008). This sensitivity enhancement is possible thanks to the SPIONs' large magnetic moment, which affects both transverse and longitudinal relaxation time of nearby ^{1}H spins in a manner that is fairly well understood (Shah et al., 2016; Chen et al., 2012).

While superparamagnetic iron oxide particles and hyperpolarized gases have been used independently, for different applications, very few studies have tried to combine them (Vignaud et al., 2005; Branca et al., 2010). Vignaud et al. (2005) used SPIONs in combination with HP ^{3}He to decrease the tissue/air susceptibility mismatch and increase the transverse relaxation time of HP ^{3}He in the lungs. Years ago, our group proposed combining HP ^{3}He with SPIONs to increase sensitivity and specificity of MR to detect cancer cells in the lungs (Branca et al., 2010). However, to our knowledge, no studies have yet been performed to evaluate the effects of iron oxide on HP gases systematically, specifically to separate the effects of SPIONs on the longitudinal and transverse relaxation times of hyperpolarized gas spins as well as their effects on image contrast.

Therefore, the objective of this work is to separate and characterize the effects of SPIONs on the transverse and longitudinal relaxation rates of hyperpolarized xenon under several restricted diffusion regimes and evaluate the effect that SPIONs have on hyperpolarized xenon image contrast in gradient-recalled echo sequences. This is accomplished by first computing the field perturbation generated by various amounts of iron oxide nanoparticles. Three-dimensional random walk simulations of spins diffusing and dephasing within the magnetic field perturbation created by SPIONs are then used to analyze the contribution of SPIONs to the longitudinal and transverse spin relaxation at different length scales while

the magnetization decay within individual voxels is utilized to generate simulated gradient-recalled echo MR images. Comparisons to previous experimental data are made and new experimental work is performed to validate the simulations.

4.2 Transverse and Longitudinal Relaxation in Magnetic Field Gradients

In this section, the theory behind transverse and longitudinal relaxation of nuclear spins in magnetic field gradients is introduced. First, transverse relaxation in uniform magnetic field gradients, including the three main regimes of transverse magnetization decay based on three characteristic length scales is described. Then the most up to date theory on transverse relaxation in non-uniform magnetic field gradients, including various approximation regimes like the static dephasing regime, Gaussian phase approximation, and weak field approximation is introduced. Finally, a refresher on longitudinal relaxation of nuclear spins in magnetic field gradients is provided.

4.2.1 Transverse Magnetization Decay in Uniform Magnetic Field Gradients

The effect of magnetic field gradients on the transverse relaxation time, T_2, of water has been studied for decades. In the 1960's, Robertson (1966) developed an approximation for the spin echo decay of spins diffusing in magnetic field gradients within a region bounded in one spatial dimension. Hazlewood et al. (1974) studied the transverse relaxation times of water protons in the gastrocnemius muscle of rats. They observed that the value of T_2 for cellular water in the muscle was 40-fold shorter than that for pure water and performed experiments to determine the effect from diffusion across local magnetic field gradients. The effect was shown not to account for the difference, but it did reveal that cellular water is affected by the macromolecular interfaces and the susceptibility gradients generated by these interfaces increase relaxation rates. Yablonskiy & Haacke (1994) were the first to develop a theory for signal behavior in non-uniform magnetic field gradients with work done in biological systems with spatially varying magnetic susceptibility. Jensen & Chandra (2000) continued work

in non-uniform gradients to develop a theory in systems of weak magnetic field gradients. Unfortunately, previous work on transverse relaxation in magnetic field gradients was either solved for the overall magnetization in the system or performed for nuclear spins with with very low diffusion coefficients like water.

Magnetic field inhomogeneities are known to produce a spatial variation of the Larmor frequency, causing a loss of phase coherence between the spins and a decrease in signal intensity. In the presence of uniform gradients, the behavior of the magnetization is often described based on the relative size of three characteristic length scales: the diffusion length, the structural length, and the dephasing length. The diffusion length, which is related to the mean-squared displacement, is defined as the distance that a particle can diffuse in a given time, τ:

$$l_D = \sqrt{2 \cdot q \cdot D \cdot \tau}, \tag{4.2.1}$$

where q is either 1, 2, or 3 depending on the dimension of diffusion and D is the diffusion coefficient of the molecule. This length scale depends exclusively on the diffusion coefficient of the molecule under study and on the time between signal excitation and detection, which for a gradient-recalled echo sequence corresponds to the echo time. The structural length is a measure of the dimension of the restriction in which the spin is allowed to diffuse and is defined, in three dimensions, by the volume to surface ratio

$$l_s = \frac{V}{S}. \tag{4.2.2}$$

Finally, the dephasing length is the distance a particle has to diffuse to acquire a total phase shift of 2π. For a linear magnetic field gradient, this distance is defined as (de Swiet & Sen, 1994):

$$l_g = \left(\frac{D}{\gamma g}\right)^{\frac{1}{3}}, \tag{4.2.3}$$

where γ is the gyromagnetic ratio of the nuclear spin, and g is the strength of the linear gradient.

Depending on the relative size of these length scales, three main regimes of transverse magnetization decay have been identified which are the free diffusion regime, the localization regime, and motional narrowing regime. The free diffusion regime occurs when only a small number of molecules are interacting with the walls of the structure and the gradient is sufficiently weak such that the diffusion length is the shortest length scale ($l_D < l_s, l_g$). In this case, the magnetization decay is described by Hurlimann et al. (1995):

$$\frac{M(g,\tau)}{M_0} = exp\left(-\frac{2}{3}\gamma^2 g^2 D\tau^3\right). \tag{4.2.4}$$

The motional narrowing regime is found when the structural length is the shortest characteristic length scale ($l_s < l_D, l_g$). In this regime, the spins appear to experience a mean dephasing. This is caused by the molecules' appearing to be in their mean position at the center of the boundaries causing the molecules to approach an averaged state. It is important to note that this approximation is valid when the structural length is the shortest, it begins to breakdown, because of diffraction-like effects in the attenuation function, when $l_D \sim l_g$ and must be described by a different diffusion regime. However, the dephasing of the magnetization in the motional narrowing regime is described, for restricted diffusion between two planar boundaries, by Robertson (1966):

$$\frac{M(g,\tau)}{M_0} = exp\left(-\frac{1}{120}\frac{\gamma^2 g^2 l_s^4 2\tau}{D}\right). \tag{4.2.5}$$

Other structural geometries will have a similar expression but with different numerical factors in the exponent. The last restricted diffusion regime occurs when the gradient length is shortest ($l_g < l_D, l_s$) and is known as the localization regime. In the localization regime, spins that are far from the walls become completely dephased and no longer contribute to the signal leading to edge-enhancement effects. The enhancement near the edges is caused by a reduction in spin dephasing near the walls caused by the restricted diffusion. The localization regime was studied by de Swiet & Sen (1994) who found at long echo times

between parallel plane boundaries that the magnetization decay is described by:

$$\frac{M\left(g,\tau\right)}{M_0} = c\frac{D^{\frac{1}{3}}}{\gamma^{\frac{1}{3}}g^{\frac{1}{3}}l_s}exp\left(-a_1\gamma^{\frac{2}{3}}g^{\frac{2}{3}}D^{\frac{1}{3}}\tau^3\right), \tag{4.2.6}$$

where $c = 5.8841$ and $a_1 = 1.0188$.

As can be seen from these examples, for relatively simple geometries in the presence of linear gradients, simple analytical expressions of the magnetization decay can be obtained. However, most of the magnetic field gradients in MRI experiments are non-uniform. Examples include the magnetic field gradients present in the lung airspaces or those generated by SPIONs. In this case, the dephasing length will acquire a spatial dependence and must be described by other means than the three presented above.

4.2.2 The In-between case of the Linear Gradient Approximation

When the dephasing length becomes spatially dependent, a fourth characteristic length scale, as previously described by Valckenborg et al. (2003), can be introduced which is known as the magnetic-field curvature length. The magnetic field curvature length, l_B, is a measure of the non-linearity of the magnetic field gradient and is defined as (Valckenborg et al., 2003):

$$l_B(x) = \left|\frac{g(x)}{C(x)}\right|, \tag{4.2.7}$$

where $g(x)$ is the local gradient, which in one dimension is,

$$g(x) \equiv \left|\frac{\partial B}{\partial x}\right|, \tag{4.2.8}$$

and $C(x)$ is the curvature of the local magnetic field,

$$C(x) \equiv \left|\frac{\partial^2 B}{\partial x^2}\right|. \tag{4.2.9}$$

When the magnetic-field curvature length is larger than l_g, the spins do not experience

the non-linearity of the magnetic field gradient and the description of the magnetization decay in uniform gradients still holds. However, when l_B is comparable to the local l_g, the description of the magnetization decay becomes much more complicated Valckenborg et al. (2003).

4.2.3 Approximation Regimes for Transverse Relaxation in Non-uniform Magnetic Field Gradients

In the presence of non-uniform magnetic field gradients, the magnetization decay can no longer be easily described by simple, analytical expressions. To predict magnetization decay in non-uniform gradients, multiple numerical models have been developed including the static dephasing regime, the Gaussian phase approximation, and the weak field approximation. It has been shown that these approximation regimes accurately predict the behavior of the magnetization when specific criteria are satisfied. These regimes and the criteria under which they hold will be discussed in the section.

Yablonskiy & Haacke (1994) studied signal behavior in biological tissues and near a ferrite contrast agent in the presence of static magnetic field gradients. They developed a method to model the magnetization decay in what is known as the static dephasing regime where diffusion phenomena may be ignored. In this regime, diffusion is unable to average out the phases of different nuclei faster than the time needed for their dephasing. The static dephasing regime for gradients produced by spherical SPIONs has been shown to hold true if:

$$\delta\omega \cdot \frac{\xi^{\frac{1}{3}} R_0^2}{6 \cdot D} \gg 1, \tag{4.2.10}$$

where R_0 is the average radius of the iron oxide particles, ξ is the volume fraction of iron oxide, and $\delta\omega$ is the characteristic frequency shift. For spheres, the characteristic frequency shift is defined as:

$$\delta\omega = \frac{\gamma(m_0 - m)}{3}, \tag{4.2.11}$$

where m_0 and m are the magnetization densities of the iron oxide and medium, respectively.

Sukstanskii & Yablonskiy (2004) studied signal formation in the presence of structure-specific magnetic field inhomogeneities of mesoscopic scale resulting from differences in magnetic susceptibility in biological systems. The mesoscopic scale refers, in MRI, to the scale which is smaller than the voxel size but greater than the atomic scale. The geometries studied included distributions of impermeable spheres and infinitely long cylinders. The work provided a description for the magnetization decay in the Gaussian phase approximation regime. The criterion for validity in this regime is:

$$\frac{\xi D d}{\gamma \Delta\chi B_0 R_0^2} > 1, \tag{4.2.12}$$

where d is a geometrical factor equal to three for spheres. $\Delta\chi$ is the magnetic susceptibility difference between iron oxide and the medium in which the spins are diffusing and B_0 is the external magnetic field strength.

The last approximation regime, aptly named the weak field approximation, is applicable when the magnetic field inhomogeneities are weak in magnitude and the diffusion length is large in comparison to the gradient length. This regime was originally studied by Jensen & Chandra (2000) for a model of randomly distributed magnetized spheres and then used to fit experimental data from biological systems including red blood cell suspensions and samples of human gray matter and rat liver. The weak field approximation is valid for spherical iron oxide particles when:

$$\frac{\gamma \Delta\chi B_0 R_0^2}{3D} \ll 1. \tag{4.2.13}$$

These approximation regimes for magnetization decay in non-uniform magnetic field gradients along with the description of magnetization decay in uniform gradients all describe the signal loss caused by transverse relaxation, but the nuclear spins will also undergo

longitudinal relaxation at the same time.

4.2.4 Longitudinal Relaxation in Magnetic Field Inhomogeneities

As previously discussed in chapter 3, magnetic field inhomogeneities are known to cause increased longitudinal relaxation rates. For water molecules, this effect is typically small and confined to the water molecules that are able to diffuse around the iron oxide nanoparticles and experience a fluctuation of the transverse component of the magnetic field a the Larmor frequency. However, for rapidly diffusing spins such as hyperpolarized noble gases, whose diffusion coefficient is three orders of magnitude higher than water, the effect can be significant, as shown in section 3.4. In addition, while water spins typically experience signal enhancement from field inhomogeneities in T_1-weighted sequences, diffusion in magnetic field inhomogeneities causes permanent loss of signal in hyperpolarized noble gas spins because of the non-renewable nature of the nuclear spin polarization. As a reminder, the effect of magnetic field gradients on the longitudinal relaxation rate can be described by the following relation:

$$\frac{1}{T_1} = D\frac{\left|\nabla B_T\right|^2}{B_0^2}, \tag{4.2.14}$$

where ∇B_T is the transverse component of the spatially-dependent gradient of the mean magnetic field, B_0.

The effect of magnetic field inhomogeneities on the longitudinal relaxation is important in this work as one of the goals is to analyze the conditions under which SPIONs can give rise to longitudinal relaxation.

4.3 Simulated HP ^{129}Xe Image Contrast

In this section, the methods used to simulate the effects of SPIONs on the longitudinal and transverse relaxation of HP ^{129}Xe gas are discussed. First, finite element analysis simulations to compute the magnetic field distribution around given amounts of SPIONs are presented, including comparisons to distributions with analytic solutions as a test of the

method. Then, Monte Carlo simulations used to simulate the nuclear spins' magnetization decay in the field generated by the SPIONs are described. Finally, these results are used to produce simulated magnetic resonance images to assess potential sensitivity enhancement of xenon near SPIONs and for comparison to experimental magnetic resonance images.

4.3.1 Test of Finite Element Analysis Accuracy for Model Systems

A multitude of numerical methods have been developed to determine the magnetic field inhomogeneity caused by spatial variations of the magnetic susceptibility. Bhagwandien et al. (1994) present a numerical technique based on the finite difference method to calculate the magnetic field distribution in three dimensions around an object magnetized by a strong, homogeneous magnetic field. The method matches nicely with distributions that have analytical solutions and is extended to application for cylinders with varying ratios of length and diameter. Salomir et al. (2003) use a first order perturbation approach to Maxwell's magnetostatic equation, along with Fourier transformation to solve the partial differential equations to obtain the magnetic field perturbations. The method matches data from distributions with analytical solutions to 1% precision as well as experimental data. Marques & Bowtell (2005) extended the work on Fourier-based methods to calculate magnetic field inhomogeneities caused by differences in magnetic susceptibility to calculations in biological systems. They used the method to evaluate the magnetic field inhomogeneity in the human head caused by variations in the magnetic susceptibility with tissue type. While these techniques are sufficient at determinng the magnetic field distibution, they suffer from a limited field of view and become computationally intensive at high spatial resolutions.

Therefore, for the work presented here, finite element analysis using COMSOL Multiphysics software was performed to compute the magnetic field perturbation caused by given amounts of iron oxide nanoparticles. The use of COMSOL to calculate the magnetic field allows for a large field of view to be analyzed without loss in spatial resolution, as the mesh size of the simulations can be easily decreased with minimal increases in computation time.

Table 4.1: Internal and external field changes for simple geometries, including the effect of the sphere of Lorentz

Geometry	Internal Field Change	Internal Field Change for Parameters Used Here (ppm)	External Field Change	External Field Change For Parameters Used Here (ppm)
Sphere	$\chi_e/3$	-0.12	$\chi_e/3$	-0.12
Infinite Cylinder (axis parallel to B_0)	$\chi_i/3$	-0.24	$\chi_e/3$	-0.12
Infinite Cylinder (axis perpendicular to B_0)	$\chi_e/2 - \chi_i/6$	-0.06	$\chi_e/3$	-0.12

To test the accuracy of COMSOL for computing the magnetic field perturbation, the results from the numerical simulations were compared to the analytical results for distributions with known analytical solutions. The two susceptibility distributions that were tested were the case of an infinite cylinder (oriented parallel and perpendicular to the applied magnetic field) at the center of a cubic region and the case of a sphere in an applied magnetic field at the center of a cubic region. In all cases, the radius was taken to be 12 mm, the internal susceptibility, χ_i was taken to be -0.72 ppm, the external susceptibility in the cubic region, χ_e , was taken to be -0.36 ppm, and the applied magnetic field, B_0, was taken to be 1 T. These values were chosen for comparison to the Fourier-based methods used by Marques & Bowtell (2005). Table 4.1 shows the expected values of the field change for these geometries along with the values for the parameters selected. For the external field change, the value which is approached asymptotically is included when applicable.

Figure 4.1 shows the results from both Marques & Bowtell (2005) and our simulations in COMSOL compared to the analytical solution. The results match up very well in both cases showcasing how COMSOL can be used in the same way as the Fourier-based methods to calculate the magnetic field perturbation. In fact, through the ability to increase spatial resolution by decreasing the mesh size within COMSOL, the results from COMSOL more closely match the analytical results near the edges of the sphere. Figure 4.2 shows the results for the infinite cylinder from COMSOL compared to the analytical results. These results indicate that COMSOL can accurately predict the field change in a region with spatial variations of the magnetic susceptibility. Therefore, COMSOL will be sufficient to compute the field distribution caused by various amounts of iron oxide nanoparticles for the different

geometries used in this work.

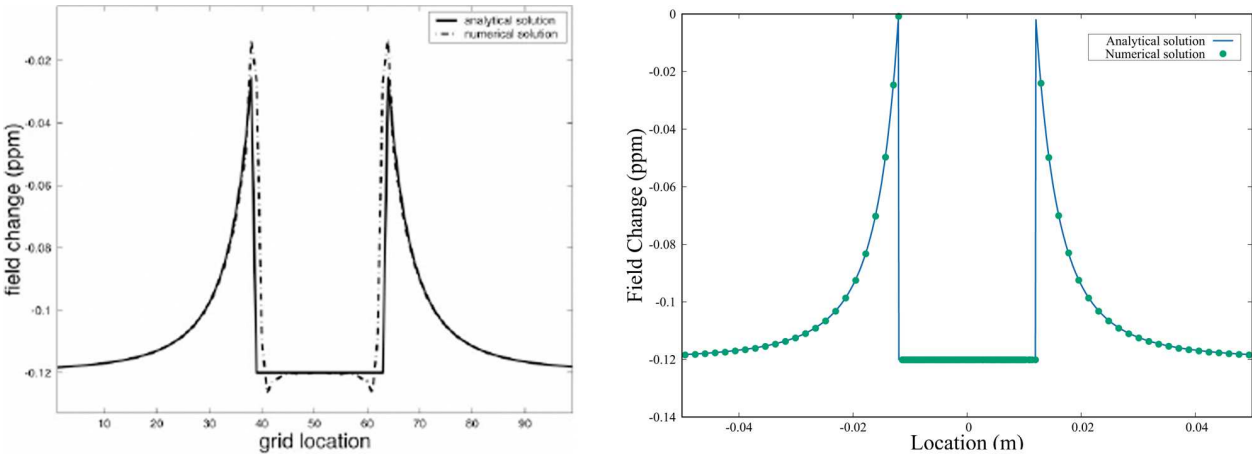

Figure 4.1: Field perturbation in ppm for a sphere of radius 12 mm with an internal magnetic susceptibility of -0.72 ppm placed in a cubic region with an external magnetic susceptibility of -0.36 ppm. The magnetic field was applied in the z-direction and the plot shows the variation of the z-component of the field change along a line through the center of the sphere. Left: Results reproduced from Marques & Bowtell (2005) using a Fourier-based method to calculate the field perturbation. Right: Results from our work using COMSOL Multiphysics to solve for the field perturbation using finite element analysis.

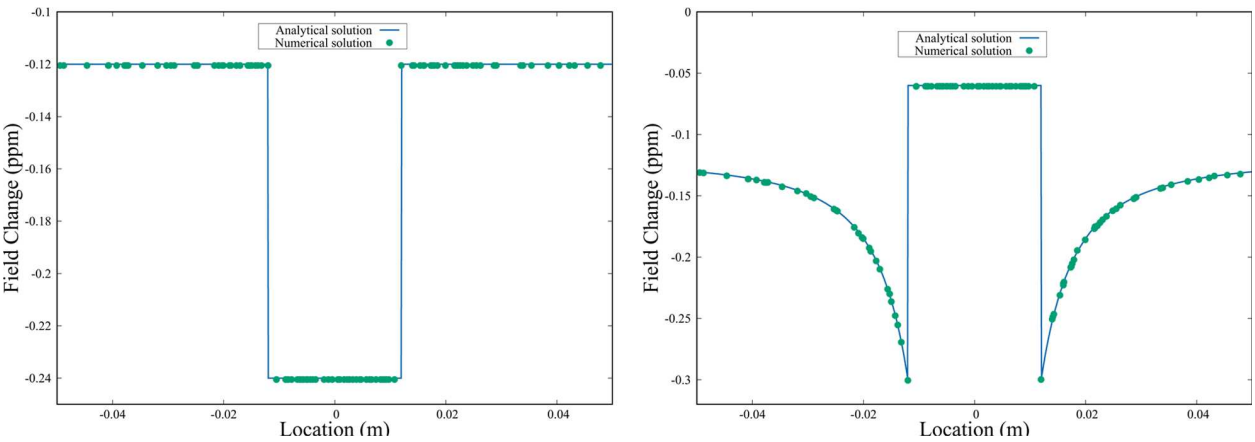

Figure 4.2: Field perturbation in ppm generated by infinite cylinders of radius 12 mm with an internal magnetic susceptibility of -0.72 ppm placed in a cubic region with an external magnetic susceptibility of -0.36 ppm. The magnetic field was applied in the z-direction. Left: Variation of the z-component of the field change with y-position along a line through the center of the cylinder with the axis of the cylinder parallel (along z) to the applied field. Right: Variation of the z-component of the field change with y-position along a line through the center of the cylinder with the axis of the cylinder perpendicular (along x) to the magnetic field.

4.3.2 Longitudinal and Transverse Relaxation During Restricted Diffusion in a Cubic Geometry

Following the simulations to test the accuracy of COMSOL in determining the magnetic field change, simulations were performed to characterize the effects, during restricted diffusion, of structural size and iron oxide concentration on the relaxation rates of hyperpolarized xenon. A simple geometry was used initially involving a cubic structure, shown in Figure 4.3, which represented the region in which the xenon gas was allowed to diffuse, with iron oxide particles placed at its center. A cubic mesh was used to guarantee equal distance between mesh points.

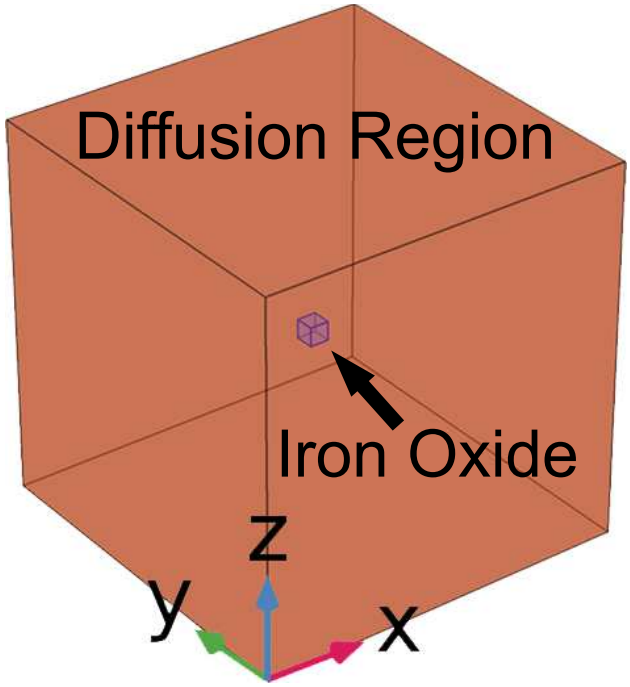

Figure 4.3: Cubic model used for COMSOL simulations. The large volume highlighted in red shows the region in which spins are allowed to freely diffuse. The purple volume at the center represents the impermeable volume occupied by iron oxide nanoparticles. The side lengths of both regions were changed proportionally to keep the volume fraction of iron oxide constant while increasing the structural length of the region of free diffusion

Five different side lengths, 0.02 cm, 0.04 cm, 0.2 cm, 0.4 cm, and 2 cm, were used for the large cube and the side length of the iron oxide was changed proportionally to maintain

a constant volume fraction of iron oxide. The volume fraction, ξ, was defined simply as:

$$\xi = \frac{L_{IO}^3}{L_C^3}, \tag{4.3.1}$$

where L_{IO} is the side length of the iron oxide and L_C is the side length of the cubic, diffusion region. To examine the various diffusion regimes, three different iron oxide volume ratios were tested: 1 ppm, 15.625 ppm, 125 ppm.

The magnetic field perturbation produced by these iron oxide particles was computed assuming a magnetic field strength of 9.4 T oriented along the z-direction as defined in Figure 4.3. The material chosen, in this case for the iron oxide was a non-linear magnetic material with a saturation magnetization of 146,000 A/m, roughly a factor of three less than the saturation magnetization of bare magnetite. The cubic region was taken to be xenon and the volume magnetic susceptibility of the region was chosen to be 0 ppm.

Upon completing the magnetic field simulations, Monte Carlo simulations were performed to determine the depolarization and dephasing of an ensemble of spins within the cubic structure. The MATLAB script from subsection 3.3.3 was modified for use in this context. First, the script was parallelized, which allowed for a much larger ensemble of spins to be used for these simulations. As such, 100,000 spins were simulated diffusing within the cubic structure. For each time step in the simulations, which was calculated using Equation 4.2.1, the instantaneous theoretical T_1 relaxation value for each spin was computed using Equation 4.2.14, in the exact same manner as in subsection 3.3.3. In addition, the spin phase for each time step was determined using the z-component of the magnetic flux density. This allowed us to calculate the transverse magnetization decay in the following manner:

$$M_T(t + \Delta t) = M_T(t) \cdot exp(-i\gamma B_z \Delta t). \tag{4.3.2}$$

In all cases, $M(0)$ was taken to be one.

Temporal resolutions for each side length are listed in Table 4.2. The temporal resolutions

Table 4.2: Calculated temporal resolutions for each structural length of the cubic geometry.

Structural Length (cm)	Temporal Resolution (μs)
0.02	0.0144
0.04	0.0825
0.2	1.44
0.4	8.37
2	135

were determined using the mean-squared displacement in three dimensions along with the average distance to the six nearest neighbors. As previously described, a cubic mesh was used to ensure equal distance between all mesh points, this also ensured that each time step in the simulations would be the same. Equal time steps were required as simulated images were generated, at specified times, by summing the magnetization of spin, with its acquired phase, for each of the 10×10 voxels in which the simulated cubic volume was partitioned.

Simulated water images were produced by assuming a static dephasing regime for the water protons, where diffusion is ignored and only transverse relaxation contributes to signal loss. For the hyperpolarized xenon gas where diffusion could not be neglected, the diffusion coefficient was determined using the Fuller-Schettler-Giddings equation (Equation 3.3.2 for a temperature of 293.15 K and pressure of 100,000 Pa and determined to be 0.117 cm^2/s.

These simulations will provide useful information on the relaxation of hyperpolarized xenon in various restricted diffusion regimes along with a way to separate the effects of SPIONs on the longitudinal and transverse relaxation of xenon, but the geometries cannot be reproduced and tested experimentally for validation. In the next section, simulations of a phantom which can be used to experimentally validate this work are discussed.

4.3.3 Generating Simulated MR Images in a Conical Phantom

Simulations were performed for a 15 ml conical centrifuge tube (Thermo Fisher Scientific, Waltham, MA, U.S.A.) with 1.5 mg of ferric oxide taped to the outside of the tube. First, a full-scale, rectangular model of the tube and iron oxide was created using the CAD software SolidWorks. A rectangular model was used instead of a cylindrical model so that a cubic

mesh could be used to partition the entire volume for the Monte Carlo simulations and generate simulated images. The CAD model was imported into COMSOL Multiphysics which calculated the field perturbation produced by the iron oxide when placed in a 9.4 T uniform magnetic field oriented along the longitudinal axis of the tube. The volume magnetic susceptibility of the ferric oxide was taken to be 5300 ppm, giving a magnetization of 39,500 A/m. This value was used to match the field perturbation produced experimentally at 9.4 T by the iron oxide nanoparticles placed on the surface of the centrifuge tube. The experimental determination of the iron oxide magnetic susceptibility is described in subsection 4.4.2.

The volume magnetic susceptibility of the empty space inside the tube was chosen to be 0 ppm to simulate xenon, while the value of the magnetic susceptibility was taken to be -9.04 ppm to simulate water for comparison (Schenck, 1996). The volume magnetic susceptibility of the 1 mm thick plastic wall of the phantom tube and the volume surrounding the tube and iron oxide was taken to be zero in all cases. Once the field was generated, the same MATLAB script used in subsection 4.3.2 was employed to calculate the longitudinal relaxation rate and magnetization for an ensemble of 100,000 spins with a temporal resolution of 70 μs. Data from MATLAB was used to generate simulated magnetic resonance images with a spatial resolution of 2 mm by 2 mm and a slice thickness of 1.65 cm (the width of the 15 ml phantom model) to match the imaging parameters used experimentally.

These simulations provided a method to validate the simulations experimentally, but they did not provide any information on how the hyperpolarized gas would be affected in a biological system. Therefore, simulations were performed on a biological model for comparison to previously acquired experimental data.

4.3.4 Simulated Magnetic Resonance Images of a Mouse Lung Model

Simulations were performed on a simplified mouse lung model, designed to simulate the alveolar space of mouse lungs, composed of a matrix of 341 empty spheres with a radius of 40 μm and a surface thickness of 4 μm, packed in a face-centered cubic structure. The airspace

of the alveoli were treated as air and had a magnetic susceptibility value of 0 ppm, while the surface was taken to be tissue and given a magnetic susceptibility of -7.79 ppm (Hopkins & Wehrli, 1997). To simulate cancerous tissue targeted by iron oxide nanoparticles, the central alveolus was filled with iron oxide mixed in water at varying concentrations. Simulations were performed for various molarities of iron oxide nanoparticles with a volume magnetic susceptibility of 5300 ppm.

The field distribution was determined in each case with COMSOL using the methods described previously. Monte Carlo simulations for an ensemble of 100,000 spins, randomly distributed among the 42 nearest alveoli surrounding the iron oxide, were performed using the MATLAB script. For these simulations, the temporal resolution was 4 ns. At each time step, the total magnetization from each spin was summed and normalized by the total number of spins to determine the overall magnetization decay within the 42 alveoli.

4.4 Experimental Validation of ^{129}Xe Image Contrast near SPIONs

In this section, the experiments used to generate magnetic resonance images for comparison to the simulated MR images are discussed. First, the hardware used for the experiment is described. Then, the experiments performed to determine the volume magnetic susceptibility of the iron oxide particles used in this work are presented, and the imaging parameters used to generate images from a conical phantom with iron oxide present on the outside of the phantom are provided. Finally, a description of experiments performed *in vivo* on ventilated mice is discussed.

4.4.1 MRI Hardware

The scanner used in this work is located in the Small Animal Imaging suite of the Biomedical Research Imaging Center at the University of North Carolina at Chapel Hill. The scanner is a Bruker Biospec 94/30 USR (Bruker Biospin, Billerica, MA, U.S.A.) with a

magnetic field strength of 9.4T controlled via a console running ParaVision software. Proton and xenon images were obtained using a 35 mm inner diameter dual-tuned $^{1}H/^{129}Xe$ volume coil (m2m Imaging Corp., OH, U.S.A.), resonant at 400 MHz and 110.7 MHz, respectively. For xenon images, phantoms were connected to a custom-built, hyperpolarized gas-compatible ventilator that enabled pumping of hyperpolarized xenon into the centrifuge tube at a constant rate. Hyperpolarized ^{129}Xe gas, with a polarization of 16% and with a 26.4% ^{129}Xe isotopic abundance, was produced using our lab's Polarean 9800 ^{129}Xe Hyperpolarizer system.

4.4.2 Experimental Determination of Iron Oxide Magnetic Susceptibility

In order to ensure that the simulated images could be compared to those images generated experimentally, it was necessary to determine the actual volume magnetic susceptibility of the iron oxide used in the experiments. To this end, experiments were performed to determine the frequency offset generated by the iron oxide that was taped to the outside of the conical phantom filled with water. Initially, the phantom was placed on the cradle so that the iron oxide was directly at the top of the 15 ml centrifuge tube and taped into position. Proton images were acquired using a spin echo sequence in the sagittal slice orientation with a field of view of 6.4 $\times$ 3.2 cm and a matrix size of 64 $\times$ 32. A frequency map was obtained by collecting images using unbalanced spin echo sequences with unbalanced times of 50 μs, 150 μs, 250 μs, 350 μs, and 450 μs.

Once all the images were acquired, the phase of each time point could be used to calculate the frequency offset for each voxel. A custom MATLAB script was developed for this purpose. The script took in the free induction decay information from each acquired image and Fourier transformed the data to find the phase from each voxel at each time point. The phase for each voxel was unwrapped and then plotted as a function of time by using the known time interval between images. The plot can then be fit to a line via linear regression and the slope of this line is the frequency offset from the resonance frequency. This data was used to

make a color map of the frequency difference for comparison to data generated in COMSOL. Figure 4.4 shows the color maps of the frequency offset from the experimental data and the COMSOL simulations. The magnetic susceptibility of the iron oxide in the simulations was varied until it closely matched the experimental data. Using this method, a volume magnetic susceptibility of 5300 ppm was found for the iron oxide used here.

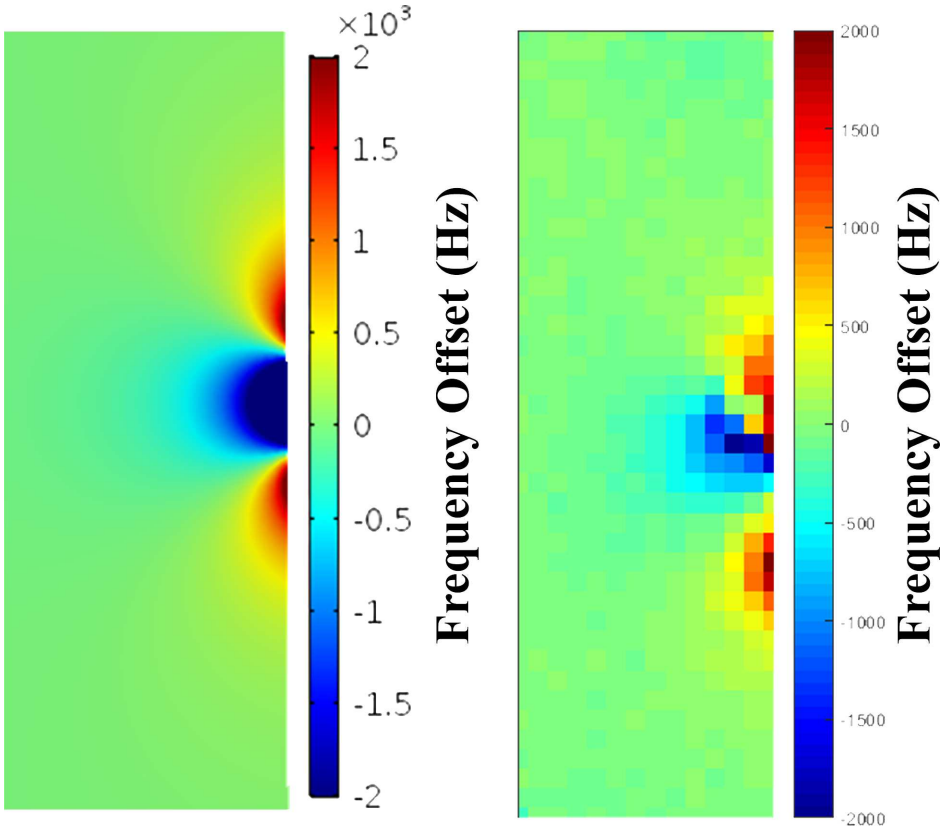

Figure 4.4: Color maps of the frequency offset which were used to estimate the magnetic susceptibility of the iron oxide particles used for the experiments in this work. Left: Color map of data taken from COMSOL for iron oxide with a magnetic susceptibility of 5300 ppm. Right: Color map of experimental data from the conical centrifuge tube with 1.5 mg of iron oxide taped to the side.

4.4.3 Experimental Imaging of Conical Centrifuge Tube

To generate phantom images, phantoms were placed on a cradle so that the iron oxide was directly at the top of the 15 ml centrifuge tube and the taped into position. The cradle was placed such that the iron oxide was at the center of the sensitive region of the volume

coil. For xenon images, the acquisition was triggered 100 ms after fresh, polarized xenon gas was flowed into the centrifuge tube. Proton and xenon images were acquired using a gradient-recalled echo sequence in the sagittal slice orientation with a field of view (FOV) of 6.4 × 3.2 cm, a matrix size of 64 × 32, flip angle (FA) of 30° , and echo times (TE) of 2.7 ms, 5.4 ms, 8.1 ms, 10.8 ms, 13.5 ms, and 16.2 ms.

4.4.4 *In vivo* MRI of Mouse Lungs in the Presence of SPIONs

In vivo animal studies were conducted under an animal protocol approved by the Institutional Animal Care and Use Committee (IACUC) at the University of North Carolina at Chapel Hill. For these experiments, two 10 month old, male C57/B6 mice were used. Prior to imaging, mice were anesthetized with an intraperitoneal injection of 75 mg/kg of pentobarbital (Nembutal, Abbott Laboratories, IL, U.S.A.), intubated and mechanically ventilated at a rate of 60 breaths per minute. The ventilation gas mixture consisted of 75-vol% N_2 and 25-vol% O_2 to generate a total tidal volume of 0.20 ml. During xenon imaging, the 75-vol% N_2 was switched to 75-vol% hyperpolarized xenon. Mice were then placed supine on the cradle and positioned such that the lungs were at the center of the sensitive region of the dual-tuned $^1H/^{129}Xe$ volume coil.

In vivo proton images were acquired using an ultra-short echo time (UTE) sequence with a field of view of 3.5 × 3.5 × 4.5 cm, flip angle of 3.57°, 1 average, repetition time (TR) of 4 ms, and an echo time of 0.012 ms. Xenon images were acquired using a gradient-recalled echo sequence for six slices in the coronal slice orientation with a field of view of 2.5 × 2.5 cm, a matrix size of 32 × 32, flip angle of 90°, slice thickness of 2 mm, 4 averages (NA), and an echo time of 2.7 ms. Xenon signal acquisition was triggered to the 400 ms breath hold. After the initial proton and xenon images were acquired, one mouse received an injection of 75 μl of saline solution with a concentration of 0.1 mg/ml of carboxymethyl-dextran-coated iron oxide nanoparticles into the lungs while the other mouse received an injection of 1 μl of saline solution with a 17 mg/ml concentration of carboxymethyl-dextran-coated iron oxide

Table 4.3: Calculated values for criteria of validity in the static dephasing regime, Gaussian phase approximation, and weak field approximation.

	Volume fraction 125 ppm	Volume fraction 125 ppm	Volume fraction 125 ppm	Volume fraction 15.6 ppm	Volume fraction 15.6 ppm	Volume fraction 15.6 ppm	Volume fraction 1 ppm	Volume fraction 1 ppm	Volume fraction 1 ppm	Centrifuge tube
Structural length (m)	0.0002	0.002	0.02	0.0004	0.004	0.04	0.0004	0.004	0.04	0.025
Static dephasing criterion $\delta\omega \cdot \frac{\xi^{\frac{1}{3}} R_0^2}{6 \cdot D} \gg 1$	2.8E-3	0.285	28.5	1.4E-4	0.142	14.2	9.1E-5	0.00911	0.911	247
Gaussian approximation criterion $\frac{\xi D d}{\gamma \Delta \chi B_0 R_0^2} > 1$	1.5E-4	1.5E-6	1.5E-8	1.9E-5	1.9E-7	1.9E-9	7.7E-6	7.7E-8	7.7E-10	1.8E-8
Weak field criterion $\frac{\gamma \Delta \chi B_0 R_0^2}{3D} \ll 1$	0.424	42.4	4240	0.424	42.4	4240	0.0678	6.78	678	20,600

nanoparticles near the very edge of the lungs. Each mouse was separately repositioned within the magnet and proton and xenon images were acquired using the same parameters as the pre-injection images.

4.5 Results and Discussion

Criteria of validity for the static dephasing regime, Gaussian phase approximation, and the weak field approximation were tested for relevant parameters of all simulated geometries, including those of the 15 ml centrifuge tube. A summary of the calculated values for each approximation regime is show in Table 4.3. From these calculations, it is shown that none of these theories are sufficient to model the overall magnetization decay for any of the cubic geometries simulated. While these results indicate that the static dephasing regime may describe the overall magnetization decay in the centrifuge tube, it cannot be used to describe the decay within individual voxels. More importantly, at large structural lengths, the signal decay of individual voxels, which ultimately determines the image contrast, can vary significantly based on the voxel's proximity to the iron oxide.

The effect of diffusion on transverse relaxation was analyzed using simulations of multiple structural length and iron oxide volume fractions. Simulated ^{129}Xe images for two different structural lengths but the same iron oxide volume fraction are shown in Figure 4.5. As can be seen from the figure, at a structural length of 400 μm, adding a boundary around the iron

oxide prevents the xenon from diffusing near the iron oxide and experiencing the strongest dephasing, considerably reducing the relaxation effects of the iron oxide nanoparticles. We can tell that the relaxation is reduced with the addition of the boundary through the decrease in contrast generated by the hyperpolarized xenon. However, at a length scale of 4000 μm this is no longer true. At this larger scale, the contrast generated by the iron oxide with and without the boundary is nearly identical.

When the relative contribution of T_1 and $T_2^\star$ to the signal decay is analyzed, it is clear that, in both cases, the main contribution to the signal decay is from transverse relaxation as seen in Figure 4.6. For both structural lengths, there is a negligible contribution to the magnetization decay from longitudinal relaxation. While the T_1 effect can be decreased slightly with the addition of a boundary, the overwhelming majority of magnetization loss arises from the dephasing of the spins near the iron oxide, which is only slightly enhanced in the absence of a boundary.

Figure 4.7 shows simulated xenon and proton images for an echo time of 2.7 ms. From this figure, it is clear that structural length plays a major role in the contrast generated by the iron oxide nanoparticles. For the 1 ppm and 125 ppm iron oxide volume fractions, diffusion is only apparent at small length scales (hundredths of centimeters). It is important to note that while the contrast enhancement in both cases is not equivalent, as the color bars vary from image to image, contrast "wash-out" is apparent for both volume fractions. This contrast "wash-out" is the result of spins being in the motional narrowing regime where spins have sufficient time to lose their individuality defined by their initial positions. However, at the largest length scales (centimeters), the effect of diffusion completely disappears. For the intermediate length scale, the effect of spin diffusion is observed only near the edges of the dark spot.

Of course the type of contrast generated depends on the echo time at which the images are acquired. At very short echo times, the diffusion length can be much shorter than the structural and dephasing lengths. In this case, the spins behave as expected in the free

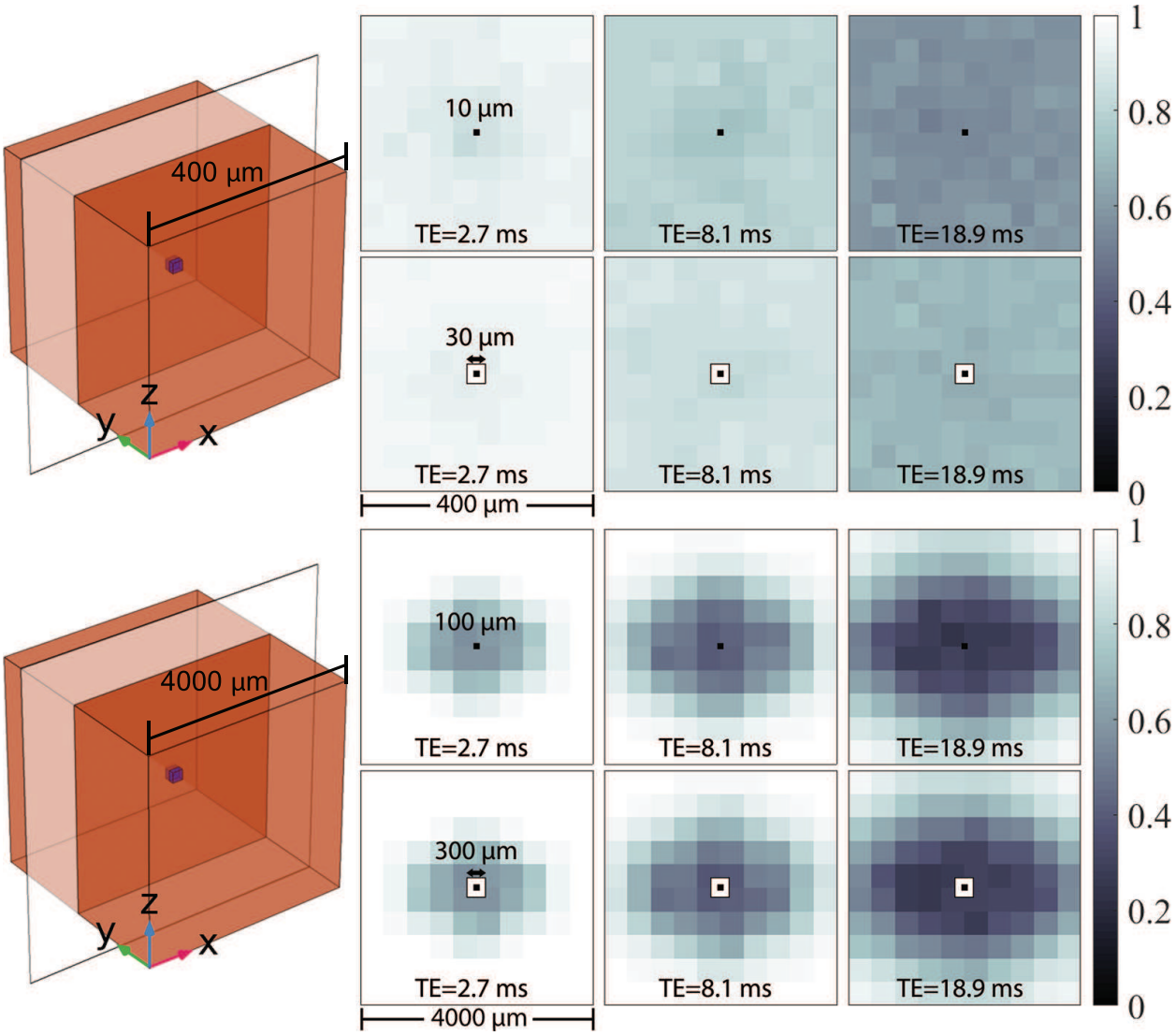

Figure 4.5: Simulated hyperpolarized ^{129}Xe MR images showing a slice in the XZ plane (modeled by translucent slice in cartoon to the left) at different echo times displaying the effect of a boundary around the iron oxide on image contrast. Top: Diffusion region with a side length of 400 μm and iron oxide with a side length of 10 μm. Adding a boundary causes a noticeable difference in contrast enhancement. Bottom: Diffusion region with a side length of 4000 μm and iron oxide with a side length of 100 μm. Adding a boundary causes no noticeable change in contrast enhancement.

diffusion regime. However, at longer echo times, for small structural lengths the spins soon move into the motional narrowing regime as shown in Figure 4.8.

At larger length scales, similar to those probed by current MRI techniques, xenon spins that are far away from the iron oxide nanoparticles appear to be in the free diffusion regime, whereas spins near the iron oxide nanoparticles appear to be in the localization regime. This

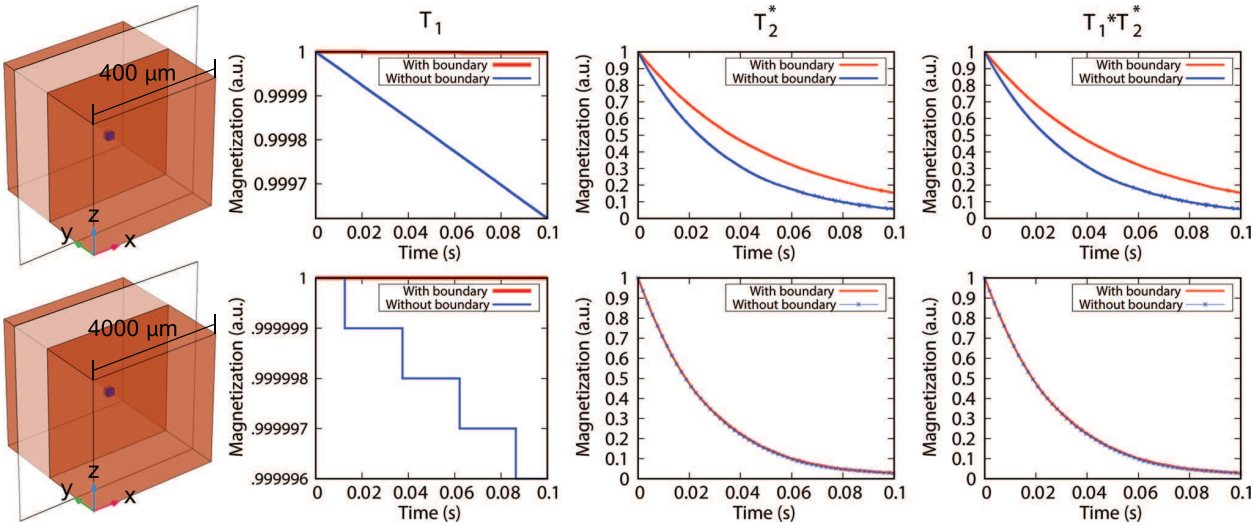

Figure 4.6: Longitudinal and transverse relaxation curves for two different diffusion regions with the same iron oxide volume fraction showing that the overwhelming majority of relaxation arises from transverse spin dephasing. Top: 400 μm side length diffusion region. While only a very small difference is seen in longitudinal relaxation when adding a boundary, a noticeable difference is seen in transverse relaxation. Bottom: 4000 μm side length diffusion region. In this case, the addition of a boundary has a negligible effect on both longitudinal and transverse relaxation.

behavior is confirmed by an analysis of the magnetization decay as shown in Figure 4.9. At short length scales, the magnetization decay, both near and far from the iron oxide, has a linear dependence on time. According to Equation 4.2.5 and Equation 4.2.6, this could mean that the region is within the motional narrowing or localization regimes. Figure 4.7 shows that the regime is most likely motional narrowing because of the reduction in magnetization decay for both volume fractions at the smallest length scale. However, at large length scales, the magnetization decay exhibits vastly different characteristics. Far from the iron oxide, the magnetization decay displays a cubic dependence on time, which according to Equation 4.2.4 is indicative of the free diffusion regime. Near the iron oxide, where the magnetic field gradients are highly non-uniform, and at short time scales, the magnetization decay is linear, indicating that spins have not yet experienced the non-linearity of the gradient and are effectively in the localization regime. At longer echo times, as the spins experience the non-linearity of the gradients, the behavior becomes chaotic and can no longer be defined by any of the restricted diffusion regimes described for uniform or non-uniform magnetic field

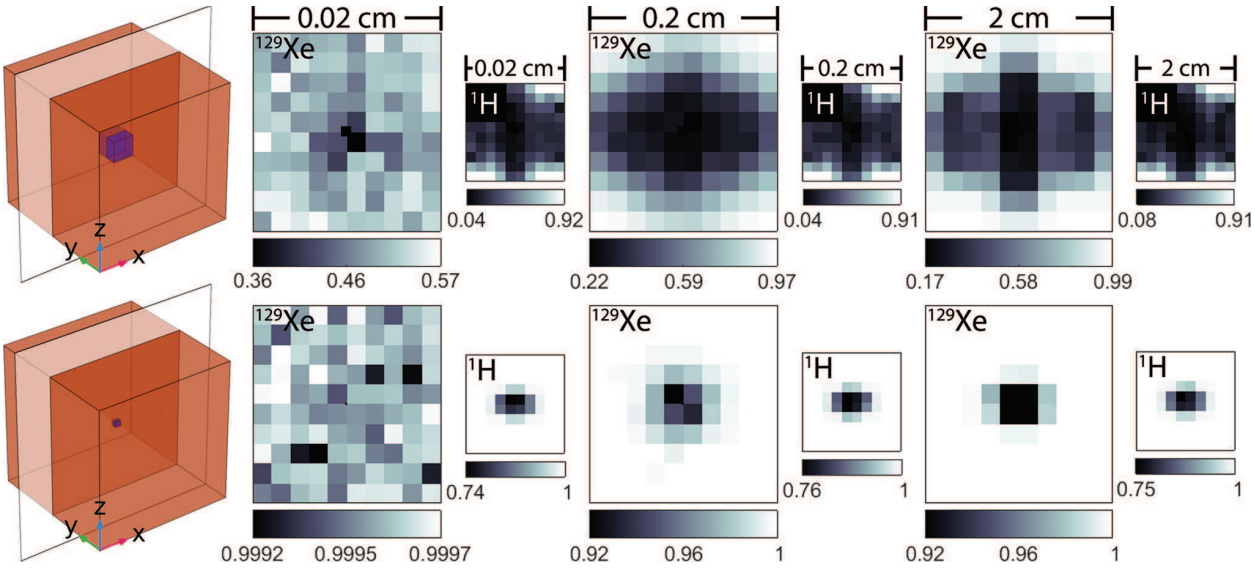

Figure 4.7: Simulated xenon and water MR images at TE=2.7 ms for two different iron oxide volume fractions, at various length scales. Top: Iron oxide volume fraction of 125 ppm. While the effect of diffusion is noticeable at small length scales, at large length scales it becomes undetectable. Bottom: Iron oxide volume fraction of 1 ppm. While the smaller amount of iron oxide used in these simulations produces a significantly smaller signal decay, the same trend holds true; the effect of diffusion is only apparent at very short length scales. Proton images appear the same at all length scales because diffusion at these length scales can be ignored. Cubes to the left are for reference but are not shown to scale.

gradients.

In order to validate the methodology used to compute the effect of iron oxide on hyperpolarized xenon images, simulations and experiments were conducted on a gas phantom in the presence of a given amount of iron oxide. In this case, the value of the saturation magnetization was chosen based on the field perturbation produced and measure experimentally by the iron oxide on the same phantom filled with water, as described in subsection 4.4.2. As can be seen from Figure 4.10, the experimental image contrast nicely matches the simulated image contrast.

These simulations also show that, at the large length scales typically probed by MRI, xenon diffusion provides no sensitivity enhancement to iron oxide. The lack of contrast enhancement arising from diffusion of xenon is evident when xenon images are compared to proton images acquired from the same phantom filled with water. The contrast produced by

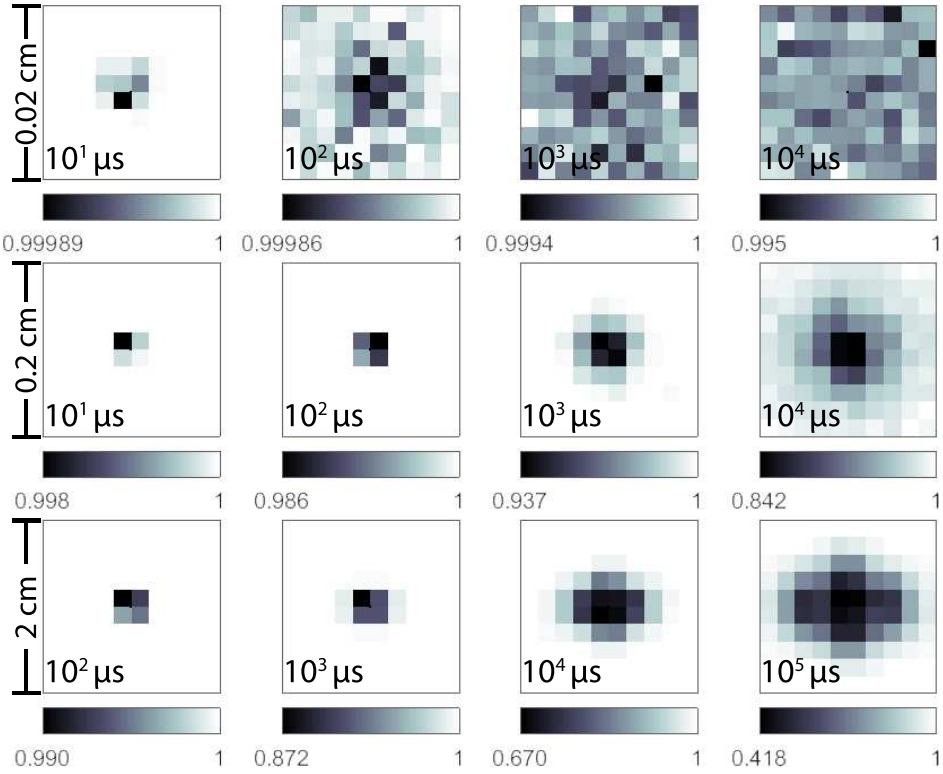

Figure 4.8: Simulated xenon MR images at various length scales for an iron oxide volume fraction of 1 ppm. Top: While at extremely short echo times the spins are in the free diffusion regime, as the echo time increases thet quickly move into the motional narrowing regime. Center: At intermediate length scales, the effect of diffusion becomes apparent at longer echo times (milliseconds). Bottom: At large length scales, the effect of diffusion is undetectable even at longer echo times (tenths of a second).

iron oxide in the proton images looks very similar to the contrast produced by the same iron oxide particles in the xenon images acquired at a fourfold longer echo time, Table 4.4 shows the gyromagnetic ratios for various nuclei used in MRI including many used in hyperpolarized gas MRI. As can be seen from the table, the ratio of gyromagnetic ratios for ^{1}H and ^{129}Xe is $\sim$3.6. This indicates that, in the absence of diffusion-mediated sensitivity enhancement caused by xenon's three orders of magnitude higher diffusion coefficient and knowing that magnetization decay is caused mostly by transverse relaxation, the proton images are expected to appear the same as the xenon images acquired at a fourfold longer echo time.

Figure 4.11 shows that, in the case of this centrifuge tube, while the dephasing length still has a spatial dependence, voxels far from the iron oxide, are still in the free diffusion

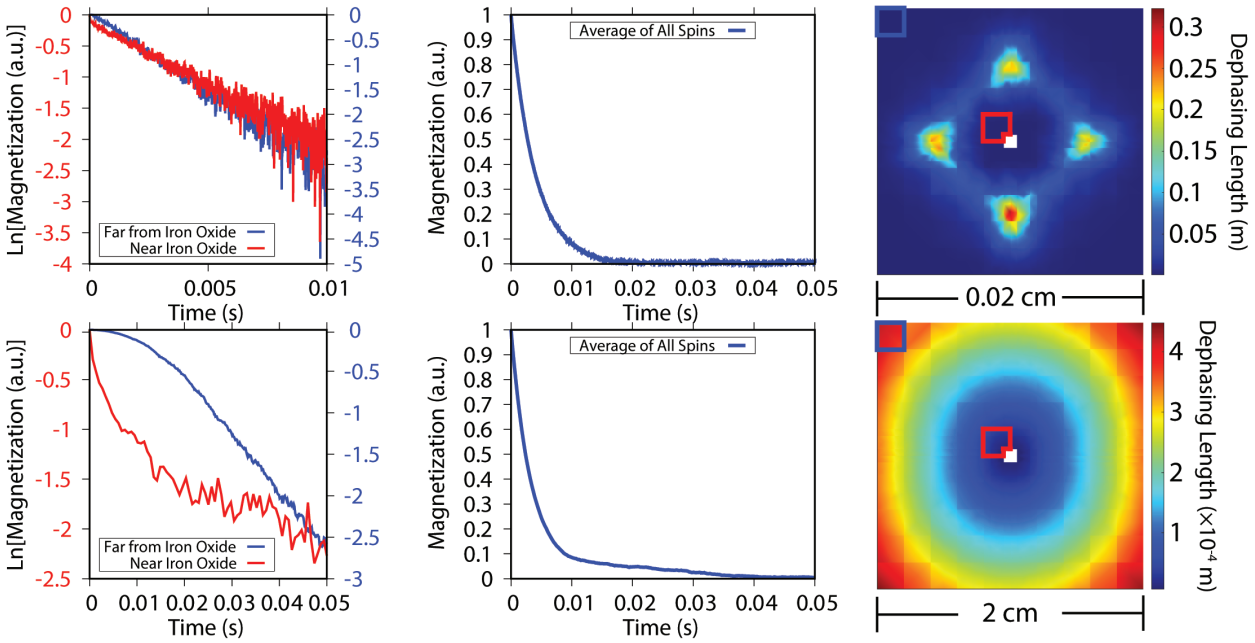

Figure 4.9: Simulated xenon magnetization decay for an iron oxide volume fraction of 125 ppm for small and large length scales. Top: For the smallest diffusion region, the magnetization decay both near and far from the iron oxide exhibits a linear dependence on time, indicating that spins are in the motional narrowing regime and have lost their individuality defined by their initial positions. Bottom: For large diffusion regions, more than one diffusion regime exists. While spins far from the iron oxide are in the free diffusion regime, as indicated by the cubic time dependence on the log of the magnetization, near the iron oxide the log of the magnetization decay is linear for short echo time, indicative of the localization regime. However, as the spins continue to evolve they experience the non-linearity of the dephasing gradients and the magnetization decay becomes chaotic.

regime. However, near the iron oxide, where the magnetic field gradients are highly non-uniform and the magnetic-field curvature length is on the order of the diffusion length, the magnetization decay quickly becomes chaotic and cannot be described analytically by any of the restricted diffusion regimes. In addition, Figure 4.11, shows that, while the overall magnetization decay may have an analytical expression, the magnetization decay can vary significantly from voxel to voxel. Therefore, even though the conical centrifuge tube meets the criterion of validity for the static dephasing regime and the overall decay can be predicted by a simple exponential decay, the static dephasing regime cannot predict the magnetization decay for individual voxels in this geometry and, more importantly, cannot predict the image contrast generated for this setup.

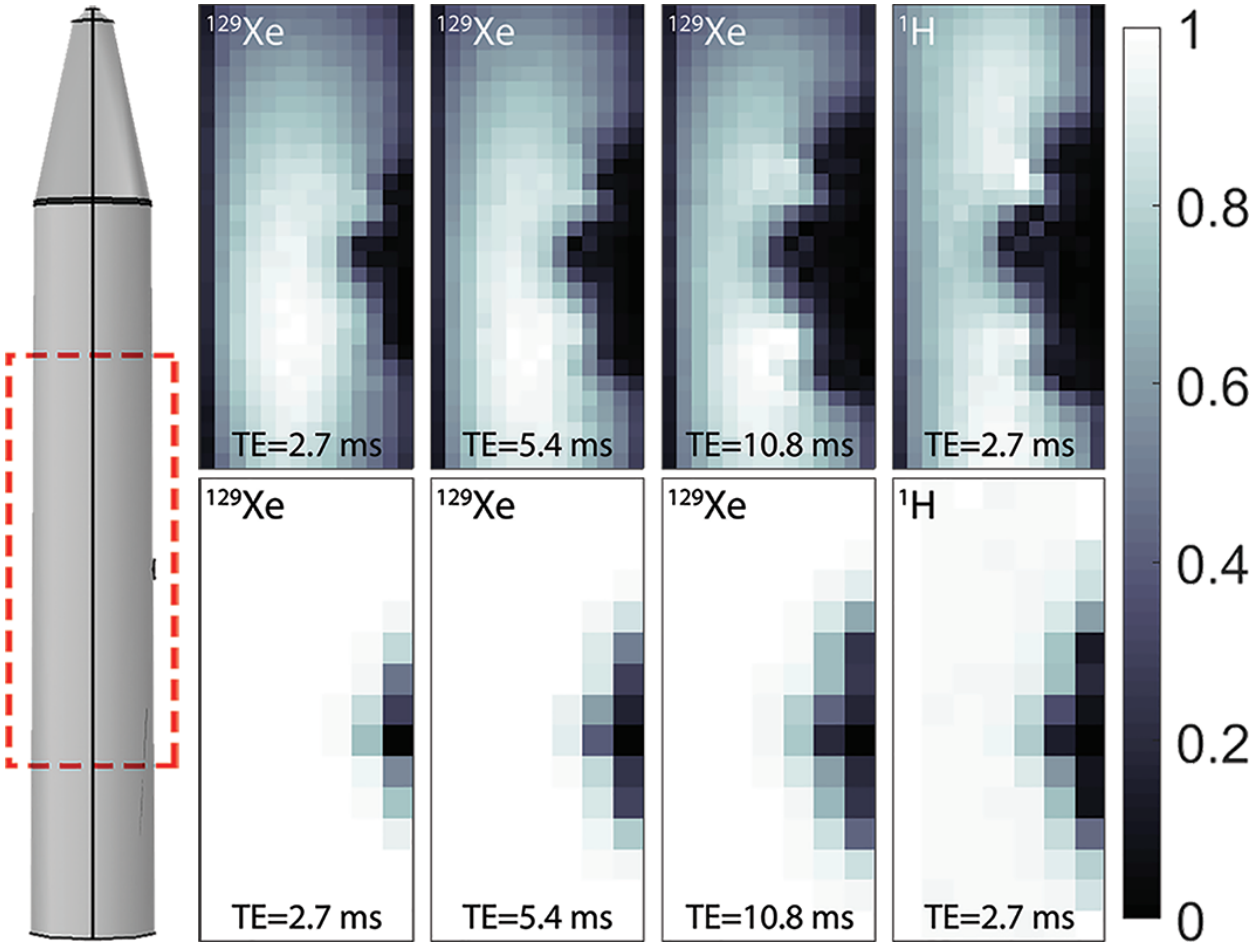

Figure 4.10: Experimental (top) and simulated (bottom) xenon and water MR images of a 15 ml conical centrifuge tube (shown on left with red outline indicating slice size) with 1.5 mg of iron oxide taped on the outer wall (right side of tube). As the echo time increases, the effect of xenon gas diffusion is unnoticeable in both the simulations and experiments. At large length scales, the contrast generated by iron oxide particles in the xenon images is similar to that observed in water images (far right) at a fourfold shorter echo time.

While the experiments performed in phantoms were able to compare the effect of SPIONs on the transverse relaxation of water and xenon, these same comparisons cannot be made in the lungs. The $T_2^\star$ effect of iron oxide on water protons cannot be used because of the significantly lower concentration of water in healthy functioning lungs and the strong magnetic field gradients present in the lungs caused by susceptibility variations. A more appropriate comparison of the effects of iron oxide would be between the $T_2^\star$ effect for xenon in gradient-recalled echo images, which is a halo effect from the dipolar field, to the T_1 enhancement for water protons in ultra-short echo time images, which is a short range effect. Such

Table 4.4: Gyromagnetic ratios of specific nuclei used in MRI

Nucleus	Gyromagnetic Ratio (MHz/T)
^{1}H	42.577
^{3}He	-32.434
^{13}C	10.708
^{19}F	40.052
^{129}Xe	-11.777

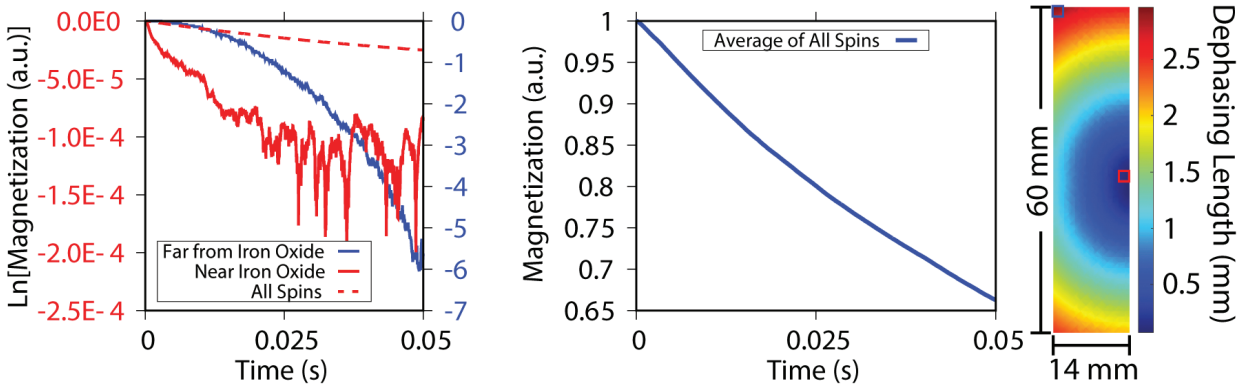

Figure 4.11: Magnetization decay for the 15 ml conical centrifuge tube with 1.5 mg of iron oxide taped on the outer wall. While the overall magnetization decay may be described analytically using a monoexponential function, individual voxels exhibit very different magnetization decay. Similar to the large length scale cubic simulations, spins far away from the iron oxide nanoparticles are found in the free diffusion regime. This shows that, even though iron oxide generates a non-linear magnetic field gradient, if the field is not too strong, such that the dephasing length is the shortest length throughout the volume, the free diffusion regime is still achievable. Near the iron oxide, at very short echo times, the decay is linear. However, at longer echo times, as spins experience the non-linearity of the gradient the decay becomes non-linear.

a comparison was attempted experimentally without much success as, when a given amount of iron oxide in solution was injected into the lungs, the signal defect generated in xenon images by the reduction in $T_2^\star$ could not be differentiated from ventilation defects caused by the obstruction of the airways (Figure 4.12). At the same time, a signal enhancement in the water images caused by the reduction in T_1 could not be differentiated from the injected suspension in the lungs.

As a final method of validation for our simulations, comparison to previously obtained experimental data in biological systems was performed. Hyperpolarized gases combined

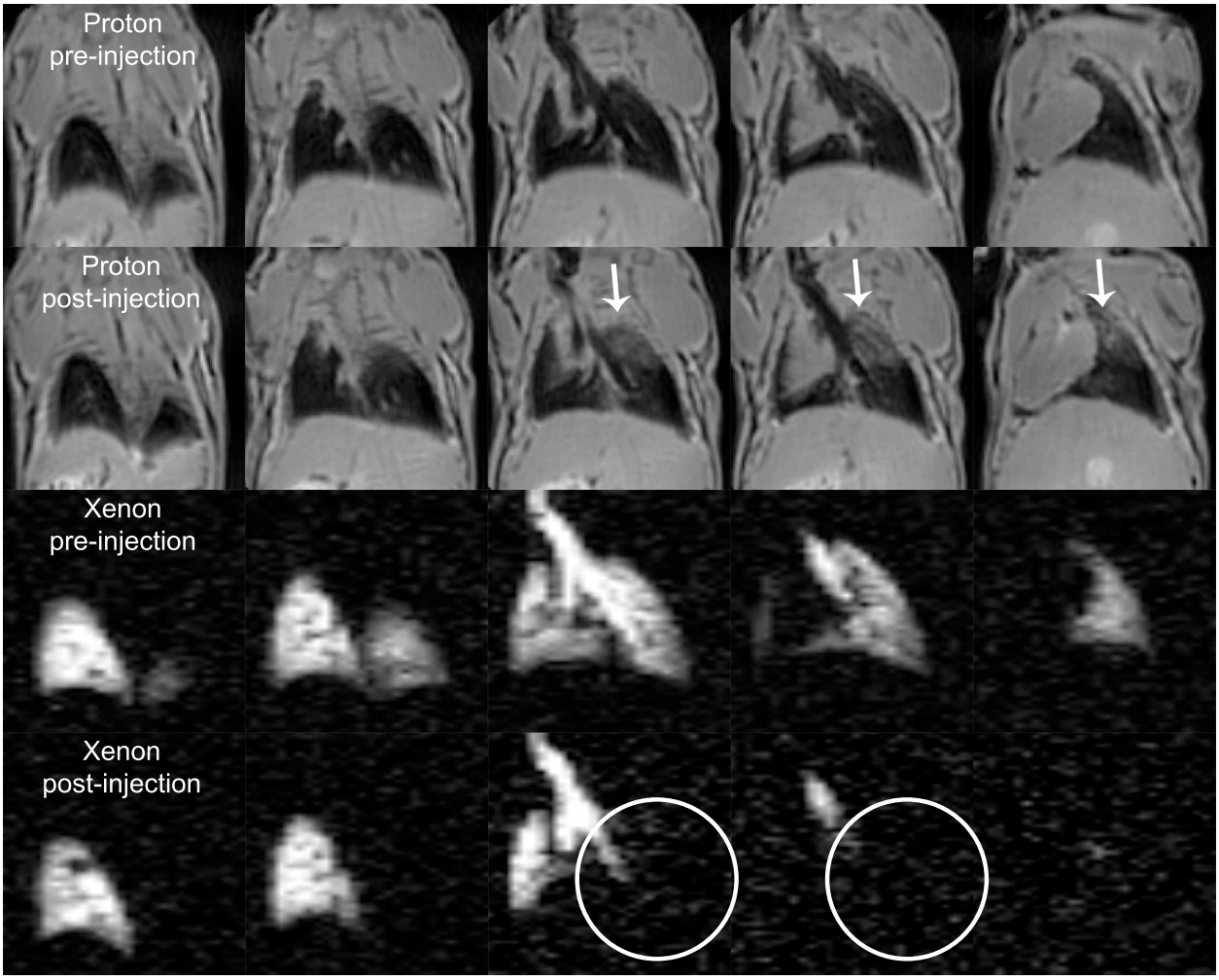

Figure 4.12: Coronal mouse lung images showing the effect of iron oxide when injected into the lungs. Top two rows are ^{1}H ultrashort-echo time (UTE) images acquired prior to (pre) and after (post) injection of iron oxide nanoparticles dissolved in saline at 0.1 mg/ml. The proton images acquired after injection show a localized enhancement close to the apex of the lungs, where the solution was injected. The bottom two rows show the HP ^{129}Xe images acquired on the same mouse before (pre) and after (post) the injection. The post-injection images show a complete occlusion of signal from the left lung indicating a ventilation defect rather than contrast enhancement in this case.

with functionalized SPIONs have been proposed to increase the sensitivity of MRI to cancer nodules in the lungs as computed tomography, the imaging modality used most frequently to provide anatomical information on lesions, is often unable to differentiate benign and malignant cells in the lungs (Branca et al., 2010; Coleman, 1999). The ability of MRI to detect cancer nodules in the lungs depends on the contrast enhancement provided by

SPIONs on the hyperpolarized gas. To test the effects of iron oxide on the longitudinal and transverse relaxation of xenon diffusing in the lung airspace, simulation were performed on a simplified model of the mouse lungs. Figure 4.13 shows the magnetization decay of the alveoli surrounding the alveolus containing iron oxide nanoparticles and water. Interestingly, at low iron oxide concentrations, the relaxation of the magnetization of nearby alveoli is reduced as the susceptibility mismatch between air and tissue is reduced, similar to the results previously obtained experimentally in mouse lungs by Vignaud et al. (2005) using hyperpolarized ^{3}He. By further increasing the iron oxide concentration in the central alveolus, the susceptibility mismatch is recreated, causing a decrease in the transverse relaxation time and an increased signal decay rate. However, the iron oxide concentration necessary to create an appreciable increase in signal decay is 93.6 μmol/L using iron oxide with a saturation magnetization of 39,500 A/m. This corresponds to a concentration of iron oxide in tissue of 15 mg/g, which is approximately fifty times higher than the achievable concentration of 0.3 mg/g (Sadhukha et al., 2013; Leftin et al., 2017). This indicates that in order to create a significant dephasing effect from SPIONs targeting single alveoli filled with cancer cells in xenon lung images, nanoparticle targeting efficiency and saturation magnetization must increase.

4.6 Conclusions

In this chapter, the effect of SPIONs on the longitudinal and transverse relaxation rates of hyperpolarized xenon during restricted diffusion was analyzed using Monte Carlo simulations. These simulations revealed that xenon signal loss near SPIONs is due mainly to transverse spin relaxation with no appreciable effect on longitudinal spin relaxation at any of the length scales analyzed and for reasonable amounts of iron oxide particles, such as those expected in targeted tissues. While the longitudinal relaxation does increase with decreasing structural length, the length scales at which a noticeable effect would occur are in the micrometer range. At larger length scales, near the iron oxide particles, simulations showed that xenon appears to be in a regime which cannot be described by conventional restricted diffusion

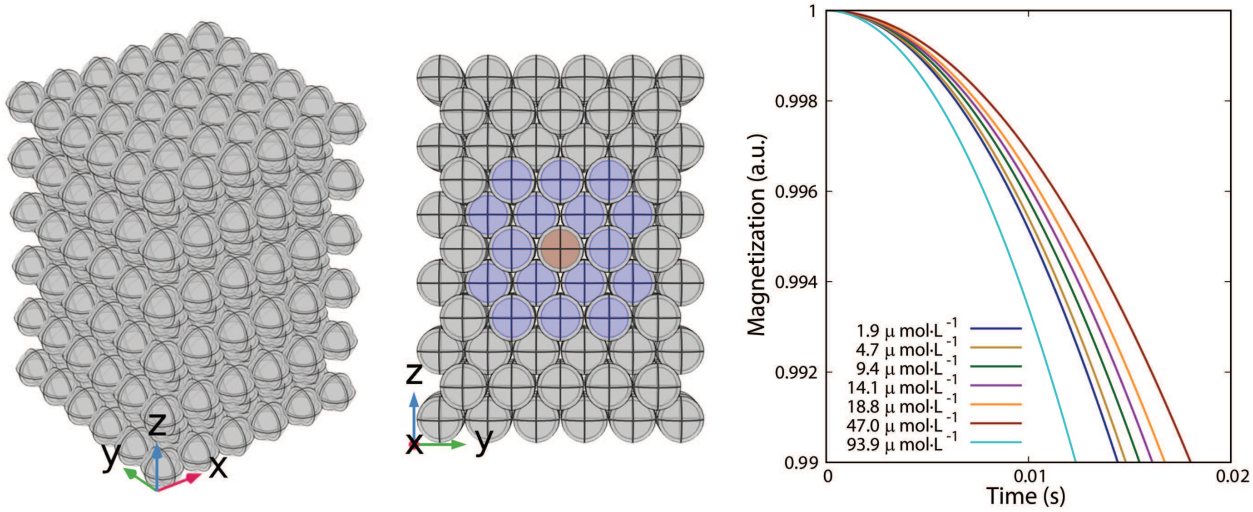

Figure 4.13: Magnetization decay for the 42 alveoli (highlighted in blue) surrounding the central alveolus (highlighted in red) containing a mixture of water and iron oxide at different concentrations. First, the relaxation is relatively small, less than 1% even after 20 ms. Second, the magnetization decay (right) shows a similar trend to the experimental decay observed by Vignaud et al. (2005) for helium gas in the mouse lungs. Initially, at increasing iron oxide concentration, the magnetization decay rate decreases, but for iron oxide concentrations >47 μmol/L, there is an increase in signal decay rate.

regimes, including approximations for non-uniform magnetic field gradients.

Simulations and experiments also revealed that xenon diffusion does not provide a sensitivity enhancement to iron oxide at the length scales achievable by current MRI techniques. Gradient-recalled echo images of water protons for the same iron oxide distribution at an echo time four times shorter than that used to acquire xenon images were virtually identical in simulations and experimentally. Therefore, in order to increase sensitivity to iron oxide, it is necessary to consider using gases with higher gyromagnetic ratios and diffusion coefficients compared to xenon, such as ^{3}He or fluorinated gases.

CHAPTER 5: CONCLUSIONS & OUTLOOK

This dissertation has presented new characterizations of depolarization mechanisms which are often ignored in continuous-flow spin exchange optical pumping and a way to use depolarization in magnetic field gradients as a new source of image contrase. In this final chapter, the contributions to the field are summarized and some guidelines for manufacturing continuous-flow hyperpolarizers, based on the work presented in this dissertation, are offered.

5.1 Fluid Flow in Continuous-flow Optical Cells

In chapter 2, results from fluid dynamics and heat transfer simulations to characterize the fluid flow within continuous-flow spin exchange optical cells were presented. Two different cell designs were tested, exhibiting vastly different flow regimes over a wide range of flow rates. The simulations reveal that many assumptions previously made while modeling the final xenon polarization need to be reevaluated. The results showed that using a plug flow to model the fluid flow leads to incorrect velocities and inaccurate flow fields inside the optical cell. More importantly, the residency times in the optical cell were shown to be much shorter than what is often calculated by using the volumetric flow rate and volume of the optical cell. Specifically, the computed residency times are not long enough to provide sufficient time for spin exchange to occur and xenon to become fully polarized. This could be the major cause for the discrepancy between theoretically predicted xenon polarizations and the values that are currently achieved by continuous-flow SEOP. These results indicate a need to change the way that the theoretical polarization is calculated to account for the distribution of residency times for xenon.

5.2 Depolarization in Magnetic Field Gradients

Work measuring the effect of magnetic field gradients on the depolarization of HP ^{129}Xe gas during continuous-flow SEOP was presented in chapter 3 and results from our attempt to leverage this depolarization effect to increase image contrast in HP ^{129}Xe MRI near superparamagnetic iron oxide nanoparticles was discussed in chapter 4.

Magnetic field gradients have long been known to affect the nuclear spin polarization of hyperpolarized noble gases. Helmholtz coils are used to generate the low, polarizing field necessary for spin exchange optical pumping due to the highly homogeneous field they create. These gradients are carefully avoided in batch method hyperpolarization but are often ignored in continuous-flow hyperpolarizers. However, continuous-flow hyperpolarizers include the Helmholtz coil for spin polarization and a much larger magnet in which the gas is stored in the frozen state during the collection process. Depending on the relative configuration of these two magnetics, it is possible that the gas, traveling from the optical cell to the cold trap, flows through a region where the magnetic field rapidly changes direction.

Therefore, the influence of strong magnetic field gradients on the relaxation of HP ^{129}Xe during continuous-flow SEOP was studied using both finite element analysis and Monte Carlo simulations which were compared to experimentally determined longitudinal relaxation values. The results indicated that the crossing of regions in which the magnetic field rapidly changes direction or assumes values very close to zero can cause significant relaxation. As such, care should be taken to avoid such gradients within the gas flow path. Large field gradients can be avoided through the use of various magnet designs for the polarizing field and the field necessary to prevent solid state relaxation. Coil designs, such as the Lee-Whiting coil can generate much larger homogeneous regions compared to a traditional Helmholtz pair (Lee-Whiting, 1957). Also, the use of a Halbach array magnet could provide better flux return for the permanent magnet and could contain the magnet field above and below the array better than other permanent magnet designs (Bjork et al., 2008). However, in the absence of such large gradients, wall relaxation is the major contributing factor to gas-phase

spin relaxation.

Superparamagnetic iron oxide particles are able to generate powerful magnetic field gradients due to their large magnetic moment. This, along with their high compatibility in biological systems, has made them a particularly interesting contrast agent for *in vivo* MR applications. SPIONs and HP gases have been used independently for different applications, but very few studies have tried to combine them. To our knowledge, before this work, no studies had been performed to systematically evaluate the effects of iron oxide on HP gases and separate the effects of SPIONs on the longitudinal and transverse relaxation times of hyperpolarized gas spins as well as their effects on image contrast.

The effects of SPIONs on the longitudinal and transverse relaxation of hyperpolarized xenon under various restricted diffusion regimes were characterized using simulations and experimental work. This work revealed that xenon signal loss near SPIONs is due mainly to transverse spin relaxation with no appreciable effect of the longitudinal relaxation. It is possible to increase the longitudinal relaxation rate of xenon near SPIONs by decreasing the structural length, but the length scales at which a noticeable effect occurs are in the micrometer range. These are much smaller length scales than can be observed with hyperpolarized gases using current MRI techniques. In addition, xenon diffusion added no sensitivity enhancement near SPIONs, so in order to increase sensitivity near iron oxide, it becomes necessary to use nuclei with higher gyromagnetic ratios, like ^{3}He or fluorinated gases.

5.3 Future Outlook

The work presented in this dissertation provides many opportunities for continued study as well as new avenues of interest. The most obvious continuation from here would be the addition of laser heating to the fluid dynamics models. This would provide a more complete picture of fluid flow in the optical cell and assist in the understanding of continuous-flow SEOP. Along these same lines, mapping the rubidium density distribution throughout the cell

would be very helpful. The xenon polarization is directly related to the rubidium polarization so a non-uniform distribution of rubidium, particularly in the case of rubidium collecting on the side of the optical cell opposite of laser incidence, could significantly affect the overall xenon polarization level. As most people who model the theoretical xenon polarization during continuous-flow assume a uniform rubidium density throughout the entire cell, mapping the rubidium density distribution would determine the accuracy of such an assumption.

Finally, these results would provide an avenue to improve the current model of xenon polarization. First, the rubidium density distribution, in conjunction with temperature and pressure data from the simulation, would provide the means to calculate a real-time, local rubidium spin exchange rate and spin destruction rate. This could be used to more accurately predict the local rubidium polarization in the optical cell from which the final xenon polarization can be estimated, potentially leading to more efficient cell designs.

The work in this dissertation has already provided some guidelines for the design of optical cells used in continuous-flow SEOP. For horizontally-oriented optical cells, the placement of the inlet should be at the bottom of the cell to increase the residency time of xenon in the optical cell through the introduction of recirculation near the inlet. The length of the optical cell should be as long as the homogeneous region of the Helmholtz pair allows. The simulations suggest that doubling the length of the current optical cell (15 cm) should increase the average residency time to over ten seconds, for both cell designs, at a volumetric flow rate of 1.5 SLM. This increase in residency time could lead to a doubling of the final xenon polarization. Additional work on various optical cell designs could provide more precise principles for the design of continuous-flow optical cells.

BIBLIOGRAPHY

Albert, M. S., Cates, G. D., Driehuys, B., et al. 1994, Nature, 370, 199

Alcock, C. B., Itkin, V. P., & Horrigan, M. K. 1984, Canadian Metallurgical Quarterly, 23, 309

Anger, B. C., Schrank, G., Schoeck, A., et al. 2008, Physical Review A, 78, 043406

Anthony, P. L., Arnold, R. G., Band, H. R., et al. 1993, Physical Review Letters, 71, 959

Antonacci, M., Burant, A., Wagner, W., & Branca, R. T. 2017, Journal of Magnetic Resonance, 279, 60

Appelt, S., Ben-Amar Baranga, A., Young, A. R., & Happer, W. 1999a, Physical Review A, 59, 2078

Appelt, S., Ünlü, T., Zilles, K., et al. 1999b, Applied Physics Letters, 75, 427

Barskiy, D. A., Coffey, A. M., Nikolaou, P., et al. 2017, Chemistry - A European Journal, 23, 725

Bassi, F., Crivellini, A., Rebay, S., & Savini, M. 2005, Computers & Fluids, 34, 507

Batz, M., Nacher, P. J., & Tastevin, G. 2011, Journal of Physics: Conference Series, 294, 012002

Becker, J., Heil, W., Krug, B., et al. 1994, Nuclear Instruments and Methods in Physics Research Section A: Accelerators, Spectrometers, Detectors and Associated Equipment, 346, 45

Ben-Amar Baranga, A., Appelt, S., Romalis, M. V., et al. 1998, Physical Review Letters, 80, 2801

Bernardes, N., & Primakoff, H. 1959, The Journal of Chemical Physics, 30, 691

Bhagwandien, R., Moerland, M., Bakker, C., Beersma, R., & Lagendijk, J. 1994, Magnetic Resonance Imaging, 12, 101

Bjork, R., Bahl, C. R. H., Smith, A., & Pryds, N. 2008, Journal of Applied Physics, 104, 013910

Bouchiat, M. A., Carver, T. R., & Varnum, C. M. 1960, Physical Review Letters, 5, 373

Branca, R. T., Cleveland, Z. I., Fubara, B., et al. 2010, Proceedings of the National Academy of Sciences, 107, 3693

Branca, R. T., He, T., Zhang, L., et al. 2014, Proceedings of the National Academy of Sciences, 111, 18001

Burant, A., Antonacci, M., McCallister, D., Zhang, L., & Branca, R. T. 2018, Journal of Magnetic Resonance, 291, 53

Burant, A., & Branca, R. T. 2016, Journal of Magnetic Resonance, 273, 124

Cates, G. D., Fitzgerald, R. J., Barton, A. S., et al. 1992, Physical Review A, 45, 4631

Cates, G. D., Schaefer, S. R., & Happer, W. 1988, Physical Review A, 37, 2877

Chann, B., Nelson, I. A., Anderson, L. W., Driehuys, B., & Walker, T. G. 2002, Physical Review Letters, 88, 113201

Chen, D.-X., Sun, N., Huang, Z.-J., et al. 2010, Journal of Magnetism and Magnetic Materials, 322, 548

Chen, D.-X., Taboada, E., & Roig, A. 2011, Journal of Magnetism and Magnetic Materials, 323, 2487

Chen, D.-X., Xu, F.-J., & Gu, H.-C. 2012, Journal of Magnetism and Magnetic Materials, 324, 2809

Chen, W. C., Gentile, T. R., Walker, T. G., & Babcock, E. 2007, Physical Review A, 75, 013416

Chen, W. C., Gentile, T. R., Ye, Q., Walker, T. G., & Babcock, E. 2014, Journal of Applied Physics, 116, 014903

Chen, X. J., Möller, H. E., Chawla, M. S., et al. 1999, Magnetic resonance in medicine, 42, 729

Cho, A. 2009, Science, 326, 778

Coleman, R. E. 1999, Journal of nuclear medicine : official publication, Society of Nuclear Medicine, 40, 814

Coulter, K., McDonald, A., Happer, W., Chupp, T., & Wagshul, M. 1988, Nuclear Instruments and Methods in Physics Research Section A: Accelerators, Spectrometers, Detectors and Associated Equipment, 270, 90

de Lange, E. E., Altes, T. A., Patrie, J. T., et al. 2006, Chest, 130, 1055

de Swiet, T. M., & Sen, P. N. 1994, The Journal of Chemical Physics, 100, 5597

Driehuys, B., Cates, G. D., Miron, E., et al. 1996, Applied Physics Letters, 69, 1668

Evans, A., McCormack, D., Ouriadov, A., et al. 2007, Journal of Magnetic Resonance Imaging, 26, 1537

Fink, A., Baumer, D., & Brunner, E. 2005, Physical Review A, 72, 053411

Fink, A., & Brunner, E. 2007, Applied Physics B, 89, 65

Flower, C., Freeman, M. S., Plue, M., & Driehuys, B. 2017, Journal of Applied Physics, 122, 024902

Freeman, M. S. 2015, Doctoral dissertation, Duke University

Freeman, M. S., Emami, K., & Driehuys, B. 2014, Physical Review A, 90, 023406

Fuller, E. N., Schettler, P. D., & Giddings, J. C. 1966, Industrial & Engineering Chemistry, 58, 18

Gamblin, R. L., & Carver, T. R. 1965, Physical Review, 138, A946

Grover, B. C. 1978, Physical Review Letters, 40, 391

Happer, W. 1972, Reviews of Modern Physics, 44, 169

Happer, W., & Van Wijngaarden, W. A. 1987, Hyperfine Interactions, 38, 435

Hazlewood, C. F., Chang, D. C., Nichols, B. L., & Woessner, D. E. 1974, Biophysical Journal, 14, 583

Hersman, F. W., Ruset, I. C., Ketel, S., et al. 2008, Academic Radiology, 15, 683

Hopkins, J. A., & Wehrli, F. W. 1997, Magnetic Resonance in Medicine, 37, 494

Hunt, E. R., & Carr, H. Y. 1963, Physical Review, 130, 2302

Hurlimann, M., Helmer, K., Deswiet, T., & Sen, P. 1995, Journal of Magnetic Resonance, Series A, 113, 260

Jameson, C. J., Jameson, A. K., & Hwang, J. K. 1988, The Journal of Chemical Physics, 89, 4074

Jau, Y.-Y., Kuzma, N. N., & Happer, W. 2003, Physical Review A, 67, 022720

Jensen, J., & Chandra, R. 2000, Magnetic Resonance in Medicine, 44, 144

Johnson, J., Thompson, A., Chupp, T., et al. 1995, Nuclear Instruments and Methods in Physics Research Section A: Accelerators, Spectrometers, Detectors and Associated Equipment, 356, 148

Kastler, A. 1967, Science, 158, 214

Killian, T. J. 1926, Physical Review, 27, 578

Lee-Whiting, G. E. 1957, Uniform Magnetic Fields, Tech. rep., Atomic Energy of Canada Ltd. Chalk River Project, Chalk River, Ont

Leftin, A., Ben-Chetrit, N., Klemm, F., Joyce, J. A., & Koutcher, J. A. 2017, PLOS ONE, 12, e0184765

Marques, J., & Bowtell, R. 2005, Concepts in Magnetic Resonance Part B: Magnetic Resonance Engineering, 25B, 65

Möller, H. E., Chen, X. J., Saam, B., et al. 2002, Magnetic Resonance in Medicine, 47, 1029

Mugler, J. P., & Altes, T. A. 2013, Journal of Magnetic Resonance Imaging, 37, 313

Mugler, J. P., Driehuys, B., Brookeman, J. R., et al. 1997, Magnetic Resonance in Medicine, 37, 809

Nagayama, G., & Tsuruta, T. 2003, The Journal of Chemical Physics, 118, 1392

Nesmeyanov, A. N. 1964, Vapor Pressure of the Elements (New York, NY: Academic Press Inc.)

Nikolaou, P., Coffey, A. M., Barlow, M. J., et al. 2014, Analytical Chemistry, 86, 8206

Nikolaou, P., Coffey, A. M., Walkup, L. L., et al. 2013, Proceedings of the National Academy of Sciences, 110, 14150

Norquay, G., Parnell, S. R., Xu, X., Parra-Robles, J., & Wild, J. M. 2013, Journal of Applied Physics, 113, 044908

Rao, M., Stewart, N. J., Norquay, G., Griffiths, P. D., & Wild, J. M. 2016, Magnetic Resonance in Medicine, 75, 2227

Repetto, M., Zimmer, S., Allmendinger, F., et al. 2016, Journal of Magnetic Resonance, 265, 197

Robertson, B. 1966, Physical Review, 151, 273

Romalis, M. V., Miron, E., & Cates, G. D. 1997, Physical Review A, 56, 4569

Ruset, I. C. 2005, Doctoral dissertation, University of New Hampshire, Durham

Ruset, I. C., Ketel, S., & Hersman, F. W. 2006, Physical Review Letters, 96, 053002

Sadhukha, T., Wiedmann, T. S., & Panyam, J. 2013, Biomaterials, 34, 5163

Salomir, R., de Senneville, B. D., & Moonen, C. T. 2003, Concepts in Magnetic Resonance, 19B, 26

Schearer, L. D., & Walters, G. K. 1965, Physical Review, 139, A1398

Schenck, J. F. 1996, Medical Physics, 23, 815

Schrank, G., Ma, Z., Schoeck, A., & Saam, B. 2009, Physical Review A, 80, 063424

Shah, E., Upadhyay, P., Singh, M., et al. 2016, New J. Chem., 40, 9507

Smirnov, P., Poirier-Quinot, M., Wilhelm, C., et al. 2008, Magnetic Resonance in Medicine, 60, 1292

Streever, R. L., & Carr, H. Y. 1961, Physical Review, 121, 20

Sukstanskii, A. L., & Yablonskiy, D. A. 2004, Journal of Magnetic Resonance, 167, 56

Theilmann, R. J., Arai, T. J., Samiee, A., et al. 2009, Journal of Magnetic Resonance Imaging, 30, 527

Tsuruta, T., Tanaka, H., & Masuoka, T. 1999, International Journal of Heat and Mass Transfer, 42, 4107

Valckenborg, R. M. E., Huinink, H. P., & Kopinga, K. 2003, The Journal of Chemical Physics, 118, 3243

Venkatesh, A. K., Hong, K. S., Kubatina, L., et al. 2001, in Proc. Intl. Soc. Mag. Reson. Med., 951

Vignaud, A., Maître, X., Guillot, G., et al. 2005, Magnetic Resonance in Medicine, 54, 28

Wagshul, M. E., & Chupp, T. E. 1994, Physical Review A, 49, 3854

Walker, T. G., & Happer, W. 1997, Reviews of Modern Physics, 69, 629

Wang, Z., Robertson, S. H., Wang, J., et al. 2017, Medical Physics, 44, 2415

Wild, J. M., Marshall, H., Bock, M., et al. 2012, Insights into Imaging, 3, 345

Woodhouse, N., Wild, J. M., van Beek, E. J. R., et al. 2009, Journal of magnetic resonance imaging : JMRI, 30, 981

Yablonskiy, D. A., & Haacke, E. M. 1994, Magnetic Resonance in Medicine, 32, 749

Zeng, X., Miron, E., Van Wijngaarden, W., Schreiber, D., & Happer, W. 1983, Physics Letters A, 96, 191

Zeng, X., Wu, Z., Call, T., et al. 1985, Physical Review A, 31, 260

Zhang, L., Burant, A., McCallister, A., et al. 2017, Magnetic Resonance in Medicine, 78, 1070

Zheng, W., Cleveland, Z. I., Möller, H. E., & Driehuys, B. 2011, Journal of Magnetic Resonance, 208, 284

Zook, A. L., Adhyaru, B. B., & Bowers, C. R. 2002, Journal of Magnetic Resonance, 159, 175